

TURBULENCE MODEL VALIDATION THROUGH JOINT EXPERIMENTAL /  
COMPUTATIONAL STUDIES OF SEPARATED FLOW OVER A  
THREE-DIMENSIONAL TAPERED BUMP

A Final Report

Part I: Experimental Investigation

JULY 2023

Patrick Gray<sup>1</sup>, Thomas Corke<sup>2</sup> and Flint Thomas<sup>3</sup>

*University of Notre Dame*

Igal Gluzman<sup>4</sup>

*Technion–Israel Institute of Technology, Haifa, Israel*

Joseph Straccia, PhD<sup>5</sup>

*The Boeing Company*

---

<sup>1</sup>Graduate Research Assistant, PhD Candidate

<sup>2</sup>Clark Chair Professor

<sup>3</sup>Professor

<sup>4</sup>Assistant Professor, Aerospace Engineering

<sup>5</sup>Aerospace Engineer, Boeing Research & Technology



## CONTENTS

Figures . . . . .	iv
Tables . . . . .	xii
Executive Summary . . . . .	1
Chapter 1: Introduction . . . . .	2
Chapter 2: Experimental Setup: Wind Tunnel and Test Methodology . . . . .	4
2.1 White Field Mach 0.6 Closed Loop Wind Tunnel . . . . .	4
2.2 Bump Model Design and Installation . . . . .	5
2.3 Bump Configurations and Coordinate Systems . . . . .	6
2.4 Flow Diagnostic Techniques . . . . .	9
2.4.1 Surface Flow Visualization . . . . .	9
2.4.2 Pitot-Static Probe Instrumentation . . . . .	10
2.4.3 Hot-wire Anemometry . . . . .	12
2.4.4 Photogrammetric Oil-Film Interferometry . . . . .	16
2.4.5 Particle Image Velocimetry . . . . .	21
2.4.6 Stereoscopic Particle Image Velocimetry . . . . .	26
2.4.6.1 Downstream Cross-planes . . . . .	26
2.4.6.2 Upstream Flow Development . . . . .	30
2.4.7 Instrumented Bump . . . . .	34
2.4.7.1 Surface Static Pressure Taps . . . . .	34
2.4.7.2 Dynamic Pressure Sensor Instrumentation . . . . .	37
Chapter 3: Boundary Conditions and Flow Quality . . . . .	40
3.1 Empty Tunnel Flow Characterization . . . . .	40
3.1.1 Freestream Pitot-Static Rakes . . . . .	40
3.1.2 Freestream X-Wire Rakes . . . . .	43
3.1.3 Total Pressure Probe Boundary Layer Investigation . . . . .	49
3.2 Splitter Plate Only (No Bump) . . . . .	54
3.2.1 Leading Edge and Side Wall Streamlines . . . . .	54
3.2.2 Boundary Layer Development . . . . .	55
3.2.3 Skin Friction Measurements . . . . .	58

Chapter 4: Documentation of Flow Over the Bump . . . . .	63
4.1 Testing Conditions . . . . .	63
4.2 Upstream Flow Development . . . . .	64
4.2.1 Boundary Layer Development . . . . .	64
4.2.2 Upstream SPIV Flow Fields . . . . .	68
4.3 Surface Streamlines . . . . .	74
4.4 Surface Static Pressure . . . . .	75
4.4.1 Time-Averaged Surface Pressure . . . . .	75
4.4.2 Instantaneous Surface Pressure . . . . .	78
4.5 Surface Skin Friction . . . . .	82
4.6 PIV in Separation Region . . . . .	83
4.7 SPIV Cross-Plane Flow Fields in Separation Region . . . . .	87
Chapter 5: Summary and Recommendations . . . . .	94
Appendix A: Splitter Plate and Bump Installation . . . . .	97
Appendix B: OFI Calibration and Procedure . . . . .	101
Appendix C: Static Pressure Tap Locations . . . . .	105
Appendix D: Uncertainty Analysis . . . . .	108
D.1 Freestream Conditions . . . . .	108
D.2 Hot-wire Anemometry . . . . .	111
D.3 Photogrammetric Oil-Film Interferometry . . . . .	115
D.4 Particle Image Velocimetry . . . . .	116
D.5 Static Pressure Coefficient . . . . .	118
D.6 Freestream Uniformity . . . . .	120
D.7 Empty Tunnel Side Wall Boundary Layers . . . . .	123
Publications and Presentations . . . . .	127
Acknowledgements . . . . .	128
Bibliography . . . . .	129

## FIGURES

2.1	Schematic of the University of Notre Dame's White Field Mach 0.6 closed loop wind tunnel facility. . . . .	4
2.2	Cross-sectional views of the bump geometry, Gaussian in the streamwise direction and tapered in the spanwise direction using an error function. . . . .	6
2.3	Schematic of the splitter plate mounted bump model suspended inside the Mach 0.6 closed loop wind tunnel test section. . . . .	7
2.4	Drawing of an empty test section with the global coordinate system. . . . .	8
2.5	Bump configurations A and B with the bump coordinate system (red), and the moving curvilinear coordinate system (blue). . . . .	8
2.6	Photographs of the (a) UV light setup following a run, and (b) the resultant surface flow pattern revealed using the fluorescing oil mixture downstream of the bump apex. . . . .	10
2.7	Sample linear calibration for the Scanivalve PDCR23D differential pressure transducer using the NI USB 6343 DAQ. . . . .	12
2.8	Schematic of the hot-wire traverse system installed in the middle window slot for bump configuration B. . . . .	13
2.9	Photograph of the hot-wire traverse truss support and probe extending arm inside the test section. Flow is from left to right. . . . .	14
2.10	Sample calibration of the hot-wire using the velocity measured by a Pitot probe. A 3rd, 4th, and 5th order polynomial curve fit and the calibration points are shown. . . . .	16
2.11	a) Test model with imaging setup, showing the impact of surface variation on refractive angle. (b) Zoomed in view of small surface area, which highlighted by blue rectangle in panel a, demonstrating the schematic of oil-film interference process. Reproduced from Fig. 1 of Gluzman et al. [1]. . . . .	18
2.12	Top view of the bump model in Configuration A. The enumerated orange rectangle patches indicate the region where oil was applied over mounted Kapton tape surfaces. A fluorescent oil visualization image is superimposed onto the graphic to show the skin friction lines. Reproduced from Fig. 2a of Gluzman et al. [1]. . . . .	19

2.13	Fringe patterns after an experimental run at locations 5-7 in the highlighted blue rectangle region in Figure 2.12 and nearby checkerboard (7.75 mm square size), where we denote its local $x'$ - $z'$ coordinate system. Reproduced from Fig. 4 of Gluzman et al. [1]. . . . .	19
2.14	Diagram of the PIV setup used to obtain $x$ - $y$ flow field planes in the downstream bump region. . . . .	22
2.15	PIV measurement plane locations. . . . .	23
2.16	Top view diagram of SPIV cameras (with Scheimpflug adapters creating an angle $\phi$ between the camera and lens) and laser setup to sample a cross-plane velocity field on configuration A. . . . .	27
2.17	SPIV measurement plane locations. . . . .	28
2.18	Side view of the test section with the calibration plate aligned with the laser light sheet illuminating the $x/L = 0.208$ plane and the resultant calibration images taken by both of the cameras. . . . .	28
2.19	(a) Diagram showing apparent disparity in particle measurements with misalignment between the calibration plane and laser plane and (b) the resultant disparity field for a single particle field which defines the correction to be applied by the planar self-calibration. . . . .	29
2.20	Top view diagram of SPIV cameras (with Scheimpflug adapters creating an angle $\phi$ between the camera and lens) and laser setup to sample an upstream velocity field on bump configuration A. The angle between cameras is denoted by $\theta_c$ . . . . .	31
2.21	Photograph of the side view of the test section in bump configuration A. Both cameras were focused on the LaVision 106 mm two-plane calibration target placed on the flat surface upstream of the bump curvature. . . . .	32
2.22	Top view of bump section with locations of the static pressure ports shown by black dots with flow from left to right. . . . .	35
2.23	Linear calibration fit from Scanivalve differential pressure transducer voltage to Setra absolute pressure transducers, connected to the same pressure lines. . . . .	36
2.24	Kulite sensor locations on the downstream side of the bump section. .	37
2.25	Kulite calibration data referenced to the ambient lab conditions at the time of calibration. The symbols represent the calibration points for each of the sensors, and the solid lines of matching colors denote the linear calibration fits used for converting voltages to pressures. . . . .	39
3.1	Empty tunnel Pitot-static probe freestream uniformity grid locations. .	40
3.2	Labeled photograph of the empty tunnel traversing Pitot-static probe freestream uniformity setup. Flow is from right to left. . . . .	41

3.3	Freestream velocity acquired across the empty test section at a single reference velocity of $U_\infty = 69$ m/s (corresponding to $M = 0.2$ and $Re_L = 4.0 \times 10^6$ ). . . . .	42
3.4	Empty tunnel x-wire probe freestream angularity grid locations. . . . .	43
3.5	(a)Diagram of the x-wire orientations and (b) geometric relationships used to evaluate instantaneous flow angularity and velocity components. . . . .	45
3.6	(a) Setup of the x-wire and straight Pitot probe used to calibrate the x-wire anemometer channels against the velocity obtained by the Pitot probe, and (b) the setup of the x-wire for data acquisition on selected measurement grids. . . . .	45
3.7	Sample 5th order calibration fit of two hot-wire channels used during the x-wire test entry. $U_{norm}$ is the velocity perpendicular to each wire given by Equation 3.9. . . . .	46
3.8	Three-component mean velocity and turbulence RMS measured on a $4 \times 4$ grid by a traversing x-wire at $X = 0.49$ m for a freestream reference velocity of $U_\infty = 69$ m/s, corresponding to freestream Mach and Reynolds numbers based on tunnel width of $M = 0.2$ and $Re_L = 4.0 \times 10^6$ , respectively. . . . .	48
3.9	Three-component mean velocity and turbulence RMS measured on a $4 \times 4$ grid by a traversing x-wire at $X = 1.02$ m for a freestream reference velocity of $U_\infty = 69$ m/s, corresponding to freestream Mach and Reynolds numbers based on tunnel width of $M = 0.2$ and $Re_L = 4.0 \times 10^6$ , respectively. . . . .	49
3.10	Three-component mean velocity and turbulence RMS measured on a $4 \times 4$ grid by a traversing x-wire at $X = 1.37$ m for a freestream reference velocity of $U_\infty = 69$ m/s, corresponding to freestream Mach and Reynolds numbers based on tunnel width of $M = 0.2$ and $Re_L = 4.0 \times 10^6$ , respectively. . . . .	50
3.11	Three-component mean velocity and turbulence RMS measured on a $4 \times 4$ grid by a traversing x-wire at $X = 1.73$ m for a freestream reference velocity of $U_\infty = 69$ m/s, corresponding to freestream Mach and Reynolds numbers based on tunnel width of $M = 0.2$ and $Re_L = 4.0 \times 10^6$ , respectively. . . . .	51
3.12	Three-component mean velocity and turbulence RMS measured on a $4 \times 4$ grid by a traversing x-wire at $X = 1.37$ m (repeat measurement) for a freestream reference velocity of $U_\infty = 69$ m/s, corresponding to freestream Mach and Reynolds numbers based on tunnel width of $M = 0.2$ and $Re_L = 4.0 \times 10^6$ , respectively. . . . .	52

3.13 Three-component mean velocity and turbulence RMS data measured on a $4 \times 4$ grid by a traversing x-wire at $X = 1.37$ m for a freestream reference velocity of $U_\infty = 34$ m/s, corresponding to freestream Mach and Reynolds numbers based on tunnel width of $M = 0.1$ and $Re_L = 2.0 \times 10^6$ , respectively. . . . .	53
3.14 Empty tunnel boundary layer measurement locations and naming convention. . . . .	54
3.15 Photograph of the traversing mechanism used to place a total pressure probe near the empty test section walls for boundary layer measurements. . . . .	55
3.16 Diagram of the total pressure probe in an empty tunnel side wall boundary layer. When the probe was stepped towards the wall, the mean velocity sensed would decrease until a minimum velocity (and minimum $y_w$ ) was reached. When a step down resulted in a velocity increase, the probe had gone too far, and required a single step away from the wall. . . . .	56
3.17 Boundary layer profiles obtained on each of the four empty test section side walls at a reference freestream velocity of $U_\infty = 69$ m/s, corresponding to freestream Mach and Reynolds numbers based on tunnel width of $M = 0.2$ and $Re_L = 4.0 \times 10^6$ , respectively. Uncertainty bars indicate a 95% measurement confidence interval. . . . .	57
3.18 Boundary layer profiles obtained on each of the four empty test section side walls at a reference freestream velocity of $U_\infty = 34$ m/s, corresponding to freestream Mach and Reynolds numbers based on tunnel width of $M = 0.1$ and $Re_L = 2.0 \times 10^6$ , respectively. Uncertainty bars indicate a 95% measurement confidence interval. . . . .	58
3.19 Boundary layer profiles obtained on each of the four empty test section side walls at a reference freestream velocity of $U_\infty = 17$ m/s, corresponding to freestream Mach and Reynolds numbers based on tunnel width of $M = 0.05$ and $Re_L = 1.0 \times 10^6$ , respectively. Uncertainty bars indicate a 95% measurement confidence interval. . . . .	59
3.20 Flow visualization for the (a) leading edge of the flat plate and (b) a corner junction between the flat plate and a side wall near $X = 1.8$ m. . . . .	59
3.21 Flat plate boundary layer measurement locations and naming convention. . . . .	60
3.22 Boundary layer profiles obtained on the flat plate surface and a test section side wall at a reference freestream velocity of $U_\infty = 34$ m/s, corresponding to freestream Mach and Reynolds numbers based on tunnel width of $M = 0.1$ and $Re_L = 2.0 \times 10^6$ , respectively. Uncertainty bars indicate a 95% measurement confidence interval. . . . .	60

- 3.23 Boundary layer profiles obtained on the flat plate surface and test section side walls at a reference freestream velocity of  $U_\infty = 69$  m/s, corresponding to freestream Mach and Reynolds numbers based on tunnel width of  $M = 0.2$  and  $Re_L = 4.0 \times 10^6$ , respectively. Uncertainty bars indicate a 95% measurement confidence interval. . . . . 61
- 3.24 Boundary layer thicknesses for the flat plate configuration at  $U_\infty = 69$  m/s ( $M = 0.2$ ,  $Re_L = 4.0 \times 10^6$ ) averaged over the TBL measurements on the plate surface (blue circle) and the side walls (red square) for each streamwise plane. The average boundary layer thicknesses for the empty tunnel case (yellow diamond) and the empirical growth curve for a turbulent boundary layer on a smooth flat plate (Schlichting [2]). 62
- 3.25 Skin friction coefficient over the centerspan of the flat plate configuration at  $U_\infty = 69$  m/s ( $M = 0.2$ ,  $Re_L = 4.0 \times 10^6$ ) using the photogrammetric OFI method (blue circles, with 2% uncertainty bars) and the indirect Clauser method on the flat plate B profiles (red squares with 4% uncertainty bars). The measurements follow the empirical curve of Oweis et al. [3] for a smooth flat plate TBL at high  $Re$ . Reproduced from Fig. 8a of Gluzman et al. [1]. . . . . 62
- 4.1 Mean streamwise velocity profiles of the incoming TBL measured using the hot-wire anemometry system for bump configurations A (cool colors) and B (warm colors) for  $M_\infty = 0.1$  and  $0.2$ . Vertical distance is referenced from the surface of the bump  $y_b$ . Streamwise velocity is normalized by the local external velocity  $U_e$ . . . . . 67
- 4.2 Boundary layer mean velocity profile obtained using the hot-wire system at  $x/L = -0.822$  in bump configuration B compared to a composite fit [4], and another experimentally acquired ZPG TBL [5] at a similar  $Re_\theta$ , plotting in (a) outer variable scaling and (b) viscous unit scaling. . . . . 70
- 4.3 Streamwise RMS turbulence profiles of the incoming TBL measured using the hot-wire anemometry system for bump configurations A (cool colors) and B (warm colors) for  $M_\infty = 0.1$  and  $0.2$ . Vertical distance is referenced from the surface of the bump  $y_b$ . Turbulence data is normalized by the local external velocity  $U_e$ . . . . . 71
- 4.4 Boundary layer turbulence profile obtained using the hot-wire system at  $x/L = -0.822$  in bump configuration B (red squares) compared to data from another experimentally acquired ZPG TBL [5] at a similar  $Re_\theta$  (black circles), plotting in viscous unit scaling. The profile from the present experiment used a friction velocity of  $u_\tau = 2.49$  m/s; the other used  $u_\tau = 0.73$  m/s. . . . . 72
- 4.5 Total velocity field measured using the SPIV system upstream of the bump apex at three interrogation windows for the B configuration at  $M_\infty = 0.2$ . White streamlines follow the  $[U\ V]$  flow vectors. . . . . 72

4.6 Normalized mean and turbulent stress components measured on the upstream side of the bump in the B configuration using SPIV at $M_\infty = 0.2$ . . . . .	73
4.7 Comparisons of the boundary layer profile measurements between SPIV and hot-wire for the normalized (a) mean streamwise velocity and (b) streamwise turbulence intensity RMS obtained at $x/L = -0.469$ in bump configuration B at $M_\infty = 0.2$ . . . . .	73
4.8 Downstream flow topology for bump configuration A at $M_\infty = 0.2$ using florescent oil flow visualization, flow from top to bottom. Critical features were identified and denoted using notation from [6]. Surface markings were used to estimate the distance between mean separation and reattachment. . . . .	75
4.9 Time-averaged pressure coefficient distribution measured using surface taps along the bump centerline, $z/L = 0$ , for the bump configuration A at various tunnel speeds. Uncertainty bars indicate a 95% measurement confidence interval. The locations of the pressure taps are denoted in red on the bump geometry on the left plot. . . . .	77
4.10 Time-averaged pressure coefficient distribution measured using surface taps on the $z/L = -0.083$ and $-0.167$ planes, for the bump configuration A at various tunnel speeds. Uncertainty bars indicate a 95% measurement confidence interval. The locations of the pressure taps are denoted in red on the bump geometry on the left plot. . . . .	77
4.11 Time-averaged pressure coefficient distribution measured using surface taps on the apex ( $x/L = 0$ ) and at the downstream geometric inflection point ( $x/L = 0.138$ ), for the bump configuration A at various tunnel speeds. Uncertainty bars indicate a 95% measurement confidence interval. The locations of the pressure taps are denoted in red on the bump geometry on the left plot. . . . .	78
4.12 Mean static pressure coefficient measured by pressure taps ( $z/L = 0$ ) and Kulite sensors ( $z/L = 0.028$ ) for configuration A at $M_\infty = 0.2$ . The locations of the pressure taps and Kulites are denoted on the bump geometry on the left plot by blue and red symbols, respectively.	80
4.13 Static pressure fluctuation RMS normalized by the reference dynamic pressure for configuration A at $M_\infty = 0.2$ . . . . .	80
4.14 Premultiplied auto spectra of the pressures measured using the Kulite sensors, showing a peak frequency of $\sim 190$ Hz for configuration A and $\sim 230$ Hz for B. . . . .	81
4.15 Premultiplied auto spectra of the pressures measured using the K4 sensor at each of the reference speeds tested. . . . .	81

4.16 Skin friction coefficient distribution for the $M_\infty = 0.2$ case obtained using OFI for bump configurations A (blue circles) and B (red squares) with 2% uncertainty bands, and using the Clauser method on TBL velocity profiles obtained via hot-wire in configurations A (cyan sideways triangles) and B (yellow hexagrams) with 4% uncertainty bands. . . . .	82
4.17 Skin friction coefficient distribution for the $M_\infty = 0.1$ case obtained using OFI for bump configurations A (blue 'x') and B (red '+') with 2% uncertainty bands, and using the Clauser method on TBL velocity profiles obtained via hot-wire in configurations A (cyan upright triangle) and B (yellow pentagram) with 4% uncertainty bands. . . . .	83
4.18 Skin friction coefficient distribution for the $M_\infty = 0.05$ case obtained using OFI for bump configurations A (blue asterisks) and B (red dots) with 2% uncertainty bands. . . . .	84
4.19 Centerline ( $z/L = 0$ ) Mean velocity and Reynolds stress components obtained using PIV downstream of the bump apex in configuration A at $M_\infty = 0.2$ . The plane cut for which the PIV data is shown is illustrated over the bump surface on the top figure. . . . .	86
4.20 Mean streamwise velocity component obtained using PIV for the $M_\infty = 0.2$ case at the centerline ( $z/L = 0$ ) for bump configuration A. Select vertical profiles are shown. The colormap shows flow moving in the downstream direction as blue, and the backflow region in red, and white indicates $U = 0$ . . . . .	87
4.21 Spanwise distribution of mean velocity (colormap) and in-plane streamlines (white arrows) within the separation region measured with PIV at $M_\infty = 0.2$ in bump configuration A. The plane cuts for which the PIV data are shown are illustrated over the bump surface on the left plot. . . . .	88
4.22 Spanwise distribution of turbulent shear stress within the separation region measured with PIV at $M_\infty = 0.2$ in bump configuration A. The plane cuts for which the PIV data are shown are illustrated over the bump surface on the left plot. . . . .	89
4.23 Mean velocity and Reynolds stress components obtained using SPIV downstream of the bump apex in a cross-plane located at $x/L = 0.250$ at $M_\infty = 0.2$ for bump configuration A. The cross-plane cut for which the SPIV data is shown is illustrated over the bump surface on the top plot. . . . .	91
4.24 Streamwise distribution of the mean velocity (colormap) and the in-plane streamlines (white arrows in direction of [W V]) measured in several SPIV cross-planes at $M_\infty = 0.2$ for bump configuration A. The dotted black line indicates $U = 0$ . The cross-plane cuts for which the SPIV data are shown are illustrated over the bump surface on the left plot. . . . .	92

4.25 Streamwise distribution of the turbulent shear stress, $-\overline{u'v'}$ , measured in several SPIV cross-planes at $M_\infty = 0.2$ for bump configuration A. The cross-plane cuts for which the SPIV data are shown are illustrated over the bump surface on the left plot. . . . .	93
A.1 Top and bottom views of the bump section halves. . . . .	97
A.2 Trailing edge flap assembly. . . . .	98
A.3 Photograph underneath the splitter plate, the connecting fixtures are highlighted. . . . .	99
B.1 Undistorting image process for a checkerboard over a curved surface: a) the camera angle with respect to the deformed checkerboard (red curve) mounted on the curved surface (black curve). b) The process of calibration deforms the image to flatten the checkerboard. c) Extrinsic parameters visualization, where the camera for each image is projected in space relative to the local origin of the calibration board. c) Mean projected error per image. Reproduced from Fig. 6 of Gluzman et al. [1]. . . . .	103
B.2 Undistorted image of OFI application from Kapton strip 6 (see Figure 2.12). The selected rectangle was converted to into HSV space and a threshold function was used to identify the fringe centers for each pixel column (the pink dots represent the fringe centers averaged across the span). Reproduced from Fig. 7a of Gluzman et al. [1]. . . . .	104
C.1 Static pressure port locations on the instrumented bump. . . . .	105

## TABLES

2.1	Calibration uncertainty and conversion factors for each spanwise camera setup of the PIV experiment. . . . .	24
2.2	SPIV cross planar calibration angles between cameras, conversion factors for calibration mapping, and resultant dewarped image size for each cross-planes. . . . .	30
2.3	SPIV measurement locations, calibration angles between cameras, and conversion factors for calibration mapping. . . . .	33
2.4	Sample Kulite sensor pressure sensitivity obtained via calibration. . .	39
4.1	Reference freestream Mach numbers tested and the associated velocity and Reynolds number based on tunnel width. . . . .	64
4.2	Freestream speed tested for each of the flow diagnostic techniques for bump configurations A and B. The $\dagger$ symbol indicates that only a single cross-plane of SPIV was measured at the specified tunnel speed.	65
4.3	Hot-wire boundary layer profile locations and tunnel speeds. . . . .	66
4.4	Incoming boundary layer properties at both bump configurations for the $M_\infty = 0.1$ case. . . . .	68
4.5	Incoming boundary layer properties at both bump configurations for the $M_\infty = 0.2$ case. . . . .	69
4.6	Center locations of the upstream SPIV measurement windows and associated test conditions run for each of the bump configurations. . .	69
4.7	Locations of the streamwise arrays (left) and the spanwise arrays (right) and the number of taps in each, and the tunnel speed run for each of the bump configurations. . . . .	76
4.8	Kulite dynamic pressure sensor locations and tunnel speeds run for each of the bump configurations. . . . .	79
4.9	Locations and tunnel speeds run for both bump configurations using PIV. . . . .	84
4.10	Tunnel speeds and the streamwise locations of cross-planes investigated using SPIV. . . . .	90
A.1	Vertical plate alignment in the test section. . . . .	100

C.1	Locations of static pressure taps along three different streamwise axes ( $z/L = 0, 0.0833, \& 0.1667$ ). . . . .	106
C.2	Locations of static pressure taps along two different spanwise axes ( $x/L = 0 \& 0.1379$ ). . . . .	107
D.1	Confidence intervals for various coverage factor values. . . . .	110

## EXECUTIVE SUMMARY

The results of a three year experimental campaign aimed at comprehensively documenting the separated flow over a three-dimensional bump are presented with the purpose of generating a benchmark experimental database useful in validating computational fluid dynamics (CFD) flow simulations. The bump model geometry was designed to provide well-defined and repeatable smooth-body flow separation conditions that were suitable for both experiments and simulations. The bump had a Gaussian streamwise profile with a constant height equal to 8.5% of its width over the central 60% of the test section width. The remaining 40% were outboard spanwise portions that gradually taper to zero using an error function profile to minimize side-wall boundary layer effects. The model was immersed in a turbulent boundary layer that was developed on a suspended flat plate in the Notre Dame Mach 0.6 Wind Tunnel. In order to document the effect of the incoming boundary layer thickness on the flow separation, the bump model could be located at two streamwise positions. The mean velocity and turbulence intensity of the wind tunnel freestream flow field and approaching turbulent boundary layer were fully documented. The measurements of the flow separation region included surface visualization, wall shear stress using oil-film interferometry, mean and dynamic surface pressure, and planar and stereoscopic particle image velocimetry. The experiments were conducted over a range of Mach numbers from 0.05 to 0.2 corresponding to a range of Reynolds numbers based on the test section spanwise dimension (0.914m) of  $1.0 \times 10^6 \leq Re_L = U_\infty L / \nu \leq 4.0 \times 10^6$ . The bulk of the results are presented for the higher Mach number conditions of 0.1 and 0.2 with  $Re_L = 2.0 \times 10^6$  and  $4.0 \times 10^6$ , respectively. Extensive uncertainty analysis of the data was performed. The data is archived in the [NASA Langley Turbulence Modeling Resource website](#) at [https://turbmodels.larc.nasa.gov/Other\\_exp\\_Data/speedbump\\_sep\\_exp.html](https://turbmodels.larc.nasa.gov/Other_exp_Data/speedbump_sep_exp.html). In addition to the experiments, a computational effort was made in parallel by the CFD group at Boeing Research & Technology highlighting the usefulness of the data set, and is outlined in the accompanying CFD report.

## CHAPTER 1

### INTRODUCTION

It is well known that CFD methods have significant difficulty in accurately predicting turbulent separated flows relevant to off-design aerodynamic conditions. NASA's Vision 2030 study[7] outlined the desired path towards revolutionizing the aerospace communities CFD capabilities. The vision focuses on the improvement of high performance computing (HPC), as well on the understanding of the underlying physics behind challenging aerodynamic flows. Of the many interesting and important fluid flow problems, perhaps the largest gap in CFD capabilities manifests in the ability to predict viscous turbulent flows with ranging degrees of boundary layer separation and subsequent reattachment. For improved model development, there is clearly a need for high-quality, detailed benchmark experimental data sets that may be used for Reynolds-Averaged Navier-Stokes (RANS) model development, correction and validation purposes. This need was the motivation for performing a series of archival benchmark validation wind tunnel experiments on smooth body turbulent boundary layer flows leading to incipient separation, as well as small-scale and large-scale separation cases with subsequent reattachment for the purpose of CFD validation. It builds upon previous archival experiments performed on a two-dimensional separation ramp at the same wind tunnel facility in partnership with the CFD group at NASA Langley Research Center under the Transformative Tools and Technologies Program [8, 9]. These experiments highlighted the highly three-dimensional nature of the separation and recirculation region that was exhibited over a two-dimensional smooth backward facing ramp with varying degrees of APG, despite an observed two-dimensional reattachment. Of the major findings, the complex surface flow topology caused by the surface curvature and APG was described carefully, resulting in an assertion that the surface flow characteristics could be extrapolated to the side-walls and downstream in off-wall planes (this data is also archived in the [NASA Turbulence Modeling Resource](#) website).

This led to the introduction of a three-dimensional tapered Gaussian bump. The current experiments were designed and executed under a partnership between the CFD group within Boeing Research and Technology and the experimental aerodynamics research group at the University of Notre Dame. The Boeing CFD group designed the specific bump geometry to provide well-defined, repeatable conditions for experimental measurements on a model that was ideally suited to produce benchmark data for coordinated experimental and simulation campaigns. A preliminary study conducted by Williams et al.[10] showed that the bump geometry produced a separation region that was independent of side-wall interactions, and that it will serve

as an effective canonical shape for the purpose of further investigating the mechanisms behind flow separation, and validating the CFD codes that attempt to model it.

The present experiment was performed in the Notre Dame Mach 0.6 closed-circuit wind tunnel, which is a high Reynolds number, temperature controlled, low-turbulence wind tunnel specifically designed for fundamental aerodynamic research. The experiments were conducted over a range of Mach numbers from 0.05 to 0.2 corresponding to a range of Reynolds numbers based on the test section spanwise dimension of  $1.0 \times 10^6 \leq Re_L = U_\infty L / \nu \leq 4.0 \times 10^6$ , as shown in Tables 4.1 and 4.2. With the archival nature of the experiments in mind, emphasis was placed on fully documenting the wind tunnel mean and turbulence characteristics, as well as the turbulent boundary layer inflow conditions to the bump model. The documentation of the separated flow region involved numerous measurement tools including oil based surface visualization, a photogrammetric based Oil-Film Interferometry (OFI) technique to quantify the surface shear stress, static pressure taps, dynamic pressure sensors, two-component planar particle image velocimetry (PIV) and three-component stereo PIV (SPIV). Finally, documented validation steps were applied for experimental completeness Level 3 [11] on each of the tests. A sample of the data has been compared to Boeing CFD [12] to benchmark the results [13, 14, 15]. An accompanying CFD report shows the utility of the validation data set and the current capabilities of the simulation tools and techniques deployed as part of this study.

## CHAPTER 2

### EXPERIMENTAL SETUP: WIND TUNNEL AND TEST METHODOLOGY

#### 2.1 White Field Mach 0.6 Closed Loop Wind Tunnel

The experiments were conducted in the University of Notre Dame's Mach 0.6 closed return wind tunnel. The tunnel was uniquely designed for large-scale, fundamental aerodynamic research. A top-view schematic of the tunnel is shown in Figure 2.1. The flow is driven by a 1.305 MW (1750 h.p.) variable-speed AC motor that

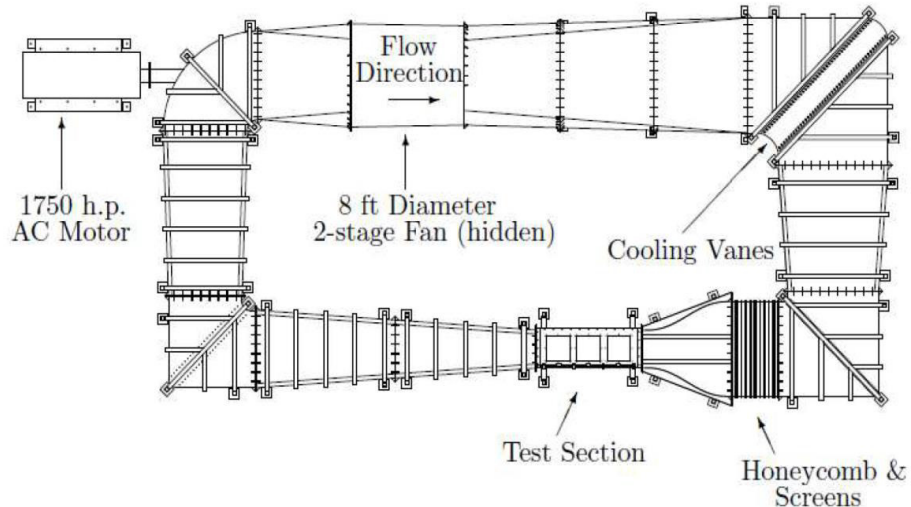


Figure 2.1. Schematic of the University of Notre Dame's White Field Mach 0.6 closed loop wind tunnel facility.

is connected to a 2.44 m (8 ft) diameter, two-stage fan with variable pitch blades. Turning vanes at the tunnel corners are designed to maintain constant tunnel air temperature with minimal pressure loss by acting as a heat exchanger. The cooling turning vanes are supplied with 4.4°C (40°F) water from a 125 ton chiller connected to a 1000 ton-hr ice storage system, with a variable internal flow rate through the

vanes. This temperature control is critical for heat transfer based measurement techniques such as hot-wire anemometry. The air temperature and speed is controlled using a computer system that allows for repeatability and accuracy in setting tunnel flow conditions. Turbulence management consists of a 152.4 mm (6.0 in) thick honeycomb section with 6.35 mm (0.25 in) cells, followed by a series of five low-solidity screens woven from 0.19 mm diameter 316-stainless steel wire loaded with 3500 lb of tension. Low freestream turbulence levels of  $\sqrt{u'^2}/U_\infty \approx 0.05\%$  were maintained over the testing conditions, and is discussed further in Section 3.1.2. One of three removable test sections was dedicated solely for this experimental work. The square test section of width  $L = 0.914$  m (3.0 ft) extends 2.743 m (9.0 ft) in the streamwise direction. On each of the tunnel side walls, three 0.61 m (24.0 in) square window slots are available. Customizable aluminum window blanks can be used for model installation and equipment installation, or clear acrylic windows can be implemented for optical access. The tunnel and test section acted as the test bed for the all of the experimental work discussed henceforth.

## 2.2 Bump Model Design and Installation

The bump model geometry was designed to provide a well defined and repeatable smooth-body flow separation case for both experimental work and simulations. The shape of the bump model, nicknamed the Boeing Bump, is shown in Figure 2.2. The bump profile is Gaussian in the streamwise,  $x$ , direction and has tapered shoulders using an error function in the spanwise,  $z$ , direction in an attempt to isolate the flow separation from side wall interactions. Its surface height,  $y_b$ , follows the distribution

$$y_b(x, z) = h \frac{1 + \operatorname{erf}((\frac{L}{2} - 2z_0 - |z|)/z_0)}{2} \exp\left(-\left(\frac{x}{x_0}\right)^2\right), \quad (2.1)$$

where  $L$  is the width of the model,  $h = 0.085L$  is the height at the apex,  $z_0 = 0.06L$ , and  $x_0 = 0.195L$ .

The experimental test model was fabricated out of 5000 series cast aluminum. A 9.5 mm (0.375 in) thick shell of the surface geometry was fabricated in two halves, which fit together using metal dowel pins and a hex nut assembly. The bump halves joined 25.4 mm (1 in) offspan with a step within  $\pm 0.08$  mm (0.003 in)– the target fabrication tolerance of the model. The joint was sealed below the bump using an RTV silicon sealant. A second bump was fabricated identically, with the addition of the instrumentation holes for static pressure taps, dynamic pressure and dynamic stress sensors (see Section 2.4.7). The non-instrumented bump was used for the oil based and optical measurement techniques, where instrumentation holes could have possibly interfered with how the oil sheared or the lasers reflected during experiments. The installation of the bump model into a boundary layer development splitter plate was designed to provide initial turbulent boundary layer (TBL) growth under nominally zero pressure gradient (ZPG) conditions prior to an interaction with the bump geometry, and a recovery back to ZPG conditions farther downstream of the bump.

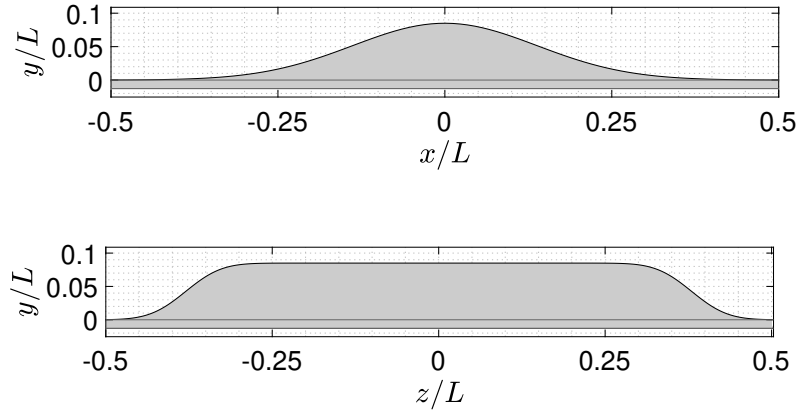


Figure 2.2. Cross-sectional views of the bump geometry, Gaussian in the streamwise direction and tapered in the spanwise direction using an error function.

Thus, the bump was installed flush into a 12.7 mm (0.5 in) thick aluminum plate assembly that was suspended from the tunnel side wall window slots using slotted L-beams, as shown in Figure 2.3. The splitter plate, which spanned the entire width of the test section, was positioned vertically so that the top edge was located  $L/2$  from the top and bottom walls. Further details on the fabrication, installation, and alignment of the splitter plate mounted bump model are given in Appendix A. The leading edge of the splitter plate consisted of a 4:1 elliptical geometry whose tip was flush with the upstream edge of the test section. At the trailing edge of the testing apparatus, an adjustable flap was deflected upward to a 2° angle to set the leading edge stagnation point near the elliptical leading edge. The test article including the splitter plate and bump sections were fabricated with a surface roughness RMS  $\approx 305\mu\text{m}$ , steps between plates  $< 0.063$  mm, and contours<sup>1</sup> within  $\pm 0.125$  mm of the CAD model. Customized cylindrical trip dots (0.292 mm tall, 1.27 mm diameter, 2.5 mm spacing between centers) were placed 51 mm downstream of the elliptical leading edge on the splitter plate and the test section walls and ceiling, in accordance with Braslow's trip criteria [16] for a TBL.

### 2.3 Bump Configurations and Coordinate Systems

The splitter plate was fabricated in several sections, so that the streamwise location of the bump apex could be varied to change the size of the incoming boundary layer. Two bump configurations were tested for the majority of the experiments in

---

<sup>1</sup>measured using a coordinate measuring machine (CMM)

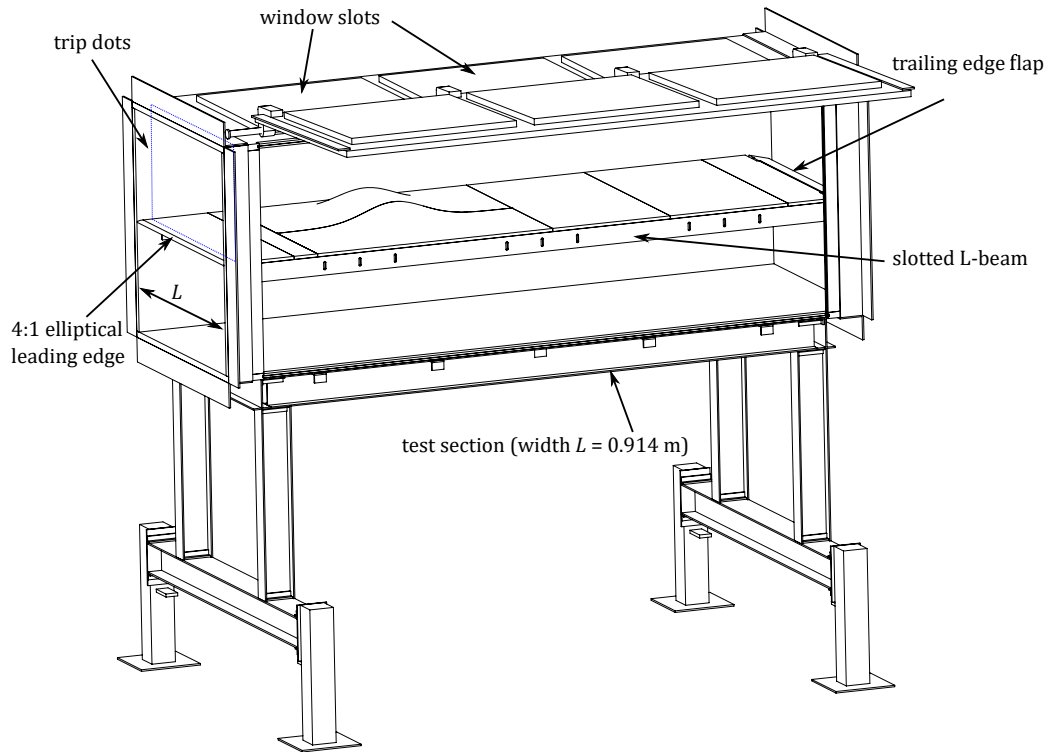


Figure 2.3. Schematic of the splitter plate mounted bump model suspended inside the Mach 0.6 closed loop wind tunnel test section.

this study. It is important to establish a few different coordinate systems based on how distances are referenced. First, a right handed global coordinate system with respect to the test section is denoted using capital  $X$ ,  $Y$ , and  $Z$  to represent streamwise, vertical, and spanwise distances from its origin, respectively. The origin of the global coordinate system (Figure 2.4) is located at the inlet of the test section, on the bottom wall, and at the centerspan between the left and right side walls.

Second, a right handed bump-based coordinate system is implemented when distances with respect to the bump are referenced, regardless of the global position of the bump apex. Here, lower case symbols  $x$ ,  $y$ , and  $z$  represent streamwise, vertical, and spanwise directions, respectively. The origin of the bump-centric coordinate system is in the same streamwise plane as the bump apex, and located vertically at  $y_b = 0$  (flush with the top surface of the flat plate), and at the centerspan of the tunnel between the left and right side walls. Figure 2.5 shows the two bump configurations with the bump coordinate system for each. Configuration A denotes the case when the bump apex is installed at a streamwise distance of  $X = X_{apex} = L$  from the inlet. The notation  $X_{apex}$  is used to describing the streamwise distance of the apex position. Configuration B denotes the case where the apex is located at  $X_{apex} = 2L$ . Occasionally, it is useful to implement a curvilinear coordinate system

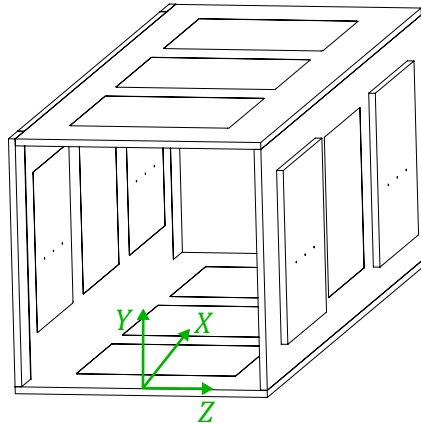


Figure 2.4. Drawing of an empty test section with the global coordinate system.

that is orthogonal to the local bump surface. For this coordinate system, the origin moves along the bump and its orientation rotates to align with the local angle of the bump surface,  $\theta_b$ . The local velocity components are also rotated to be tangent and normal to the wall surface.

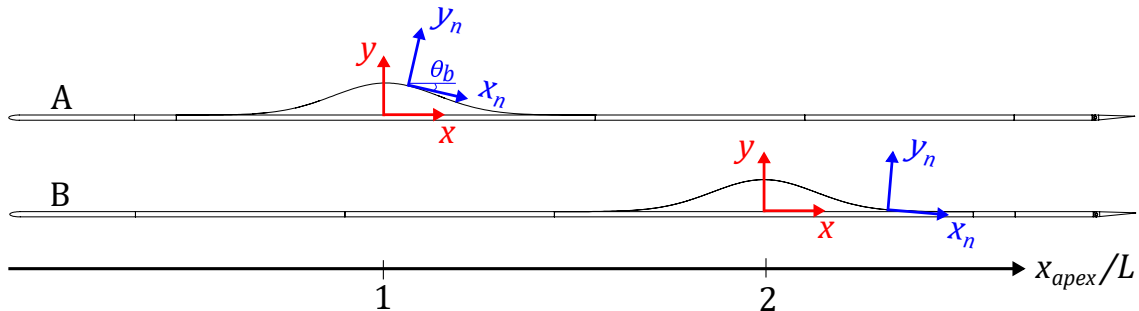


Figure 2.5. Bump configurations A and B with the bump coordinate system (red), and the moving curvilinear coordinate system (blue).

## 2.4 Flow Diagnostic Techniques

### 2.4.1 Surface Flow Visualization

A fluorescent oil mixture was applied to the bump and other critical areas of focus to visualize steady state surface flow patterns. Many techniques have been used for flow visualization in wind tunnel applications [17, 18, 19], and oil based methods are an easy and effective way to visualize skin friction lines. An oil mixture implemented by Simmons[8] was developed uniquely for experiments conducted in the Mach 0.6 facility at similar flow velocities to the present work. It is notionally a combination of two common approaches: kerosene with titanium dioxide ( $TiO_2$ ) and kerosene with aviation oil. This approach was inspired by a method recently developed by NASA Langley [20], and was adjusted based on trial and error. Specifically, the exact ratios of the mixture were adjusted depending on the flow velocity and location on the splitter plate or bump. The primary mixture by weight was as follows: 69% kerosene, 20% w100 aviation oil, 10% titanium dioxide, and 1% oleic acid. The kerosene serves as a carrier agent of the particulate  $TiO_2$ . Before the kerosene evaporates it carries the particles some distance in surface streamlines that are visible after the tunnel is turned off. The aviation oil fluoresces blue under ultraviolet (UV) to highlight the flow patterns. The oleic acid acts as an anti-clumping chemical that improves the surface streamline distribution. Prior to the application of the oil mixture, the aluminum surface would be thoroughly cleaned using isopropyl alcohol to remove previous oil residue. Diversey Spitfire cleaner removed oil and grease effectively without removing reference marks on the surface (usually made with permanent markers). The oil mixture was then mixed well in a disposable cup and brushed lightly on the surface of the bump using a sponge paint brush, which distributed the oil and  $TiO_2$  particles evenly. Once the area of interest were covered by the oil mixture, the windows were installed and the tunnel was quickly turned on to the desired speed to prevent the oil from drying up or being pulled down the bump due to gravity.

The tunnel ran and sheared the oil mixture for several minutes (typical run times were approximately 10-30 minutes, which depended on the flow velocity and the amount of mixture applied). The kerosene evaporated leaving a distribution of surface streamlines from the aviation oil and particles. The layer of oil on the surface is thin, so it retains the flow patterns of the surface with ample time to stop the tunnel, apply the UV lights, and photograph the resultant time-averaged streamlines. After the run, the top windows were unbolted and removed for the installation of the UV lights. Three light fixtures were clamped onto the edges of the window slot for ambient UV lighting of the surface (see Figure 2.6). A fourth light was available to illuminate localized areas of interest for close up images. Pictures were taken using a Canon Rebel t6 camera that has a resolution of 5184 x 3456 pixels. Select runs were also captured in real time using 5-megapixel, HD lipstick camera featuring a CMOS image sensor and a 3.6 mm wide angle lens.

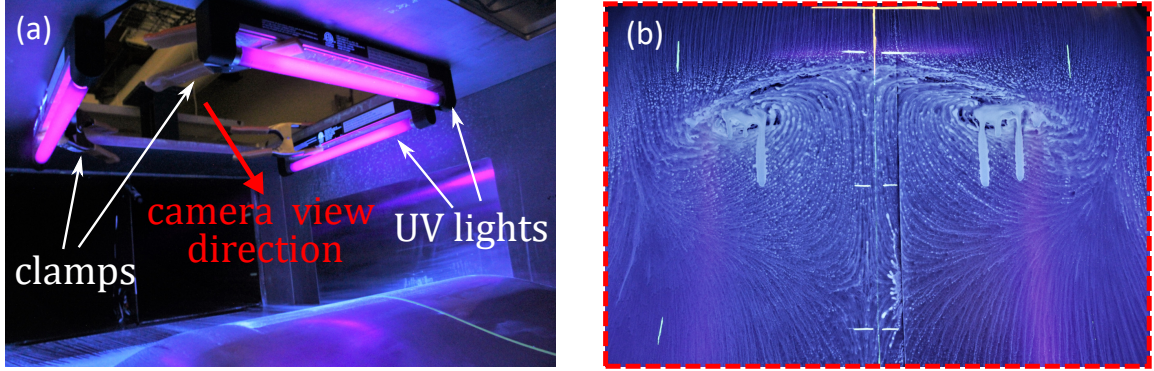


Figure 2.6. Photographs of the (a) UV light setup following a run, and (b) the resultant surface flow pattern revealed using the fluorescing oil mixture downstream of the bump apex.

#### 2.4.2 Pitot-Static Probe Instrumentation

A reference Pitot-static probe was inserted into the test section through a window on the top wall of the test section to obtain freestream dynamic pressure during test runs. A Pitot-static probe [21] uses two pressure orifices to sense a total stagnation pressure and a static pressure, whose difference yields the dynamic pressure,  $q = \frac{1}{2}\rho U^2$ . Depending on the test conducted, one of two Pitot-static probes were used to set the incoming conditions of the flow. The Pitot-probes used in the earliest tests had an inlet diameter of 1.5 mm and its leading edge was located at  $(X, Y, Z) = (0.24, 0.83, 0.37)$  m. The other probe had an inlet diameter of 1.3 mm which was placed at  $(X, Y, Z) = (0.29, 0.79, 0.37)$  m and a built in K-type thermocouple was used to acquire freestream temperature in addition to the freestream dynamic pressure. Freestream temperature was recorded using an Omega temperature logger. The reference Pitot-static probes were connected to two Setra Model 270 absolute pressure transducers via Tygon tubing. The transducers had a range of 60-110 kPa with an accuracy of 0.05% full scale with a 1 Pa resolution. Freestream velocity was calculated from differential pressure using Bernoulli's equation:

$$U = \sqrt{\frac{2\Delta P}{\rho}} \quad (2.2)$$

where  $\Delta P$  [Pa] is the difference between the total and static pressures at the reference probe, and  $\rho$  [ $\text{kg}/\text{m}^3$ ] is the air density calculated using Jones's formula [22]:

$$\rho = \frac{0.0034848}{T + 273.15} (P_{\text{atm}} - 0.0037960 * RH * P_{\text{sat}}). \quad (2.3)$$

Here,  $T$  [ $^{\circ}$ C] is the freestream temperature,  $P_{\text{atm}}$  [Pa] is the atmospheric pressure,  $RH$  [%] is the relative humidity, and  $P_{\text{sat}}$  [Pa] is the saturated water vapor pressure calculated using Teten's formula [23]:

$$P_{\text{sat}} = 0.61078 * \exp \left( \frac{17.27 * T}{T + 237.3} \right) * 1000. \quad (2.4)$$

The temperature was measured with a K-type thermocouple located in the tunnel contraction or at the reference Pitot. The atmospheric pressure and relative humidity were measured with a Fischer barometer.

Reference freestream Mach number was obtained using the ratio of the freestream velocity to the sound speed:

$$M_{\infty} = \frac{U_{\infty}}{c} = \frac{U_{\infty}}{\sqrt{\gamma R T}}, \quad (2.5)$$

where  $c$  [m/s] is the speed of sound,  $\gamma = 1.4$  is the ratio of specific heats of an ideal gas,  $R = 287.05$  (J/kg·K) is the specific gas constant of dry air, and  $T$  [K] is freestream temperature.

The Reference Reynolds numbers were recorded for each run using the freestream velocity and the kinematic viscosity of the air,  $\nu = \mu/\rho$ , where  $\mu$  is the dynamic viscosity of the air calculated using Sutherland's formula [24]:

$$\mu = \mu_0 \left( \frac{T_0 + C_0}{(T + 273.15) + C_0} \right) \left( \frac{T + 273.15}{T_0} \right)^{3/2}. \quad (2.6)$$

These constants have values of  $\mu_0 = 18.27 \times 10^{-6}$  [Pa·s],  $T_0 = 291.15$  [K], and  $C_0 = 120$  [K]. The Reynolds number based on tunnel width is given by  $Re_L = U_{\infty} L / \nu$ .

Before and after each run, the wind tunnel operator recorded the total and static pressures along with the lab ambient humidity and pressure using a Fisher traceable digital barometer. To obtain instantaneous measurements during the run, an additional transducer was implemented using T-connectors to acquire pressures identical to those sensed by the Setra transducers. A Scanivalve SSS-48C pneumatic scanner housing a PDCR23D differential pressure transducer and a SCSG2 signal conditioner was used to obtain instantaneous pressure measurements. The system's internal pressure transducer had a 17.2 kPa range with an accuracy of 0.06% full scale. Due to a mechanical failure in the Scanivalve system in the third year of testing, another differential pressure transducer system, a Validyne DP1534N1S4A 3.2 psi transducer connected to a Validyne CD280-5 module, was implemented to measure differential pressure. The freestream data were sampled digitally using a National Instruments (NI) USB 6343 data acquisition unit (DAQ) with a 16 bit analog to digital (A/D) conversion. Calibration of the additional transducers (Scanivalve or Validyne) was done by varying the tunnel speed and recording absolute pressure measurements from the Setra absolute transducers along with the additional transducer voltages. Linear calibrations (an example is shown in Figure 2.7) were done each day prior to testing.

At each tunnel speed, transducer voltages were sampled at 1 kHz for 10 seconds.

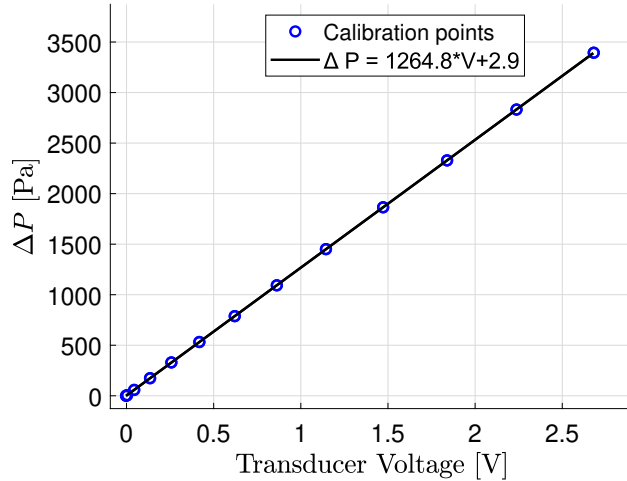


Figure 2.7. Sample linear calibration for the Scanivalve PDCR23D differential pressure transducer using the NI USB 6343 DAQ.

The uncertainty in the freestream velocities calculated from the Pitot-static probe measurements is detailed in Appendix D.1. Measurement uncertainty for the freestream conditions at a 95% confidence interval was determined to be < 0.5% for the range of tunnel speeds tested.

#### 2.4.3 Hot-wire Anemometry

Boundary layer mean velocity and turbulent shear stress profiles were taken on the boundary layer development plate, sidewalls, and bump surface using constant temperature hot-wire anemometry [25, 26]. This sensing method is based on convective heat transfer, where a relationship exists between the velocity of a fluid moving over a heated wire and the resultant change of the wire's resistance. The technique is effective in the investigation of turbulence due to its good spatial resolution near the wall, and fast temporal response allowing for high acquisition and convergence rates.

The hot-wire measurements were made using an Auspex boundary layer style probe with a  $3.8 \mu\text{m}$  thick, 1 mm long Tungsten wire that was welded onto the probe tips. In viscous units, as described in Section 4.2.1, the probe had a diameter of

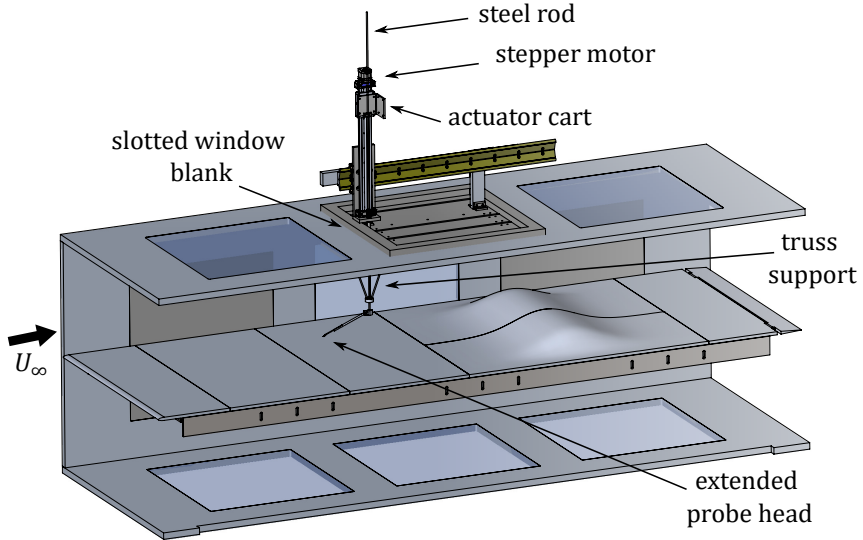


Figure 2.8. Schematic of the hot-wire traverse system installed in the middle window slot for bump configuration B.

$d^+ \approx 1$  and a length of  $l^+ \approx 150$  for the highest tunnel velocity condition tested. Figure 2.8 shows a schematic of the hot-wire system installed into the test section. The probe was fixed onto a truss support system that provided mechanical stability to prevent shaking during testing, and extended the probe head upstream away from the rest of the support. A photograph of the truss support and the extending arm holding the probe head is shown in Figure 2.9. The hot-wire probe was traversed vertically using a PBC Linear UG Series linear motion platform that housed a Nema 17 stepper motor with a step angle of  $1.8^\circ$ . The motor rotated a threaded rod so that an actuator cart stepped with a resolution of 0.05 mm/pulse. The motor was controlled by a TB6600 motor driver connected to a 12 V external power supply. Single 5 V square wave pulses were sent to the motor from a PFI channel of a National Instruments USB 6343 data acquisition unit (DAQ). The stepping motor was fixed externally to a slotted window blank and was connected to the probe extending arm through the truss support using a 4.76 mm diameter hardened 17-4 PH stainless steel rod. The window blanks were slotted so that probe head could be moved in the streamwise direction to the desired measurement location. They were sealed prior to test using 4 mil aluminum foil tape. Set screws were tightened onto the test section ceiling to fix the traverse in place and stabilize the truss system against flow induced vibrations. The ratio of the cross-sectional area of the bump, plates, and fixtures with respect to the total test section flow area was  $A_{bump}/L^2 = 7.1\%$ . The added blockage area from the truss support system was  $A_{truss}/L^2 = 0.4\%$ , creating a total blockage area with respect to the test section flow area of 7.5%.

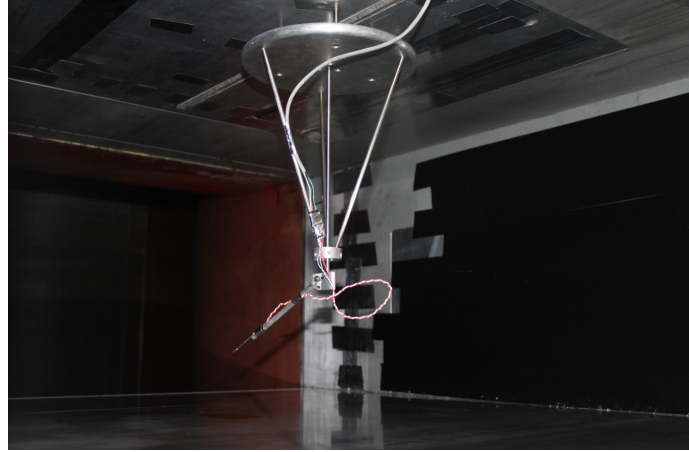


Figure 2.9. Photograph of the hot-wire traverse truss support and probe extending arm inside the test section. Flow is from left to right.

The probe was connected to a A.A. Lab Systems AN-1003 hot-wire anemometry system that housed a constant temperature anemometer (CTA) and signal conditioner module. Due to several breaks during testing, the  $3.8\ \mu\text{m}$  thick Tungsten wiring was welded onto the probe tips which were approximately 1 mm apart. Depending on the location of the weld points, and the tension of the wire during fabrication, the resistance of the probe ranged from  $3.5\text{-}4.5\ \Omega$ . The overheat ratio (OHR) was set to 1.8 for all of the measurements. No filtering was done prior to data acquisition. Wind tunnel velocity was set by adjusting the variable frequency drive fan until the desired freestream conditions were met. The 1.3 mm inner diameter reference Pitot probe located at  $(X, Y, Z) = (0.29, 0.79, 0.37)$  m was used to measured the reference freestream velocity and temperature.

Each morning prior to testing a calibration was conducted both for the reference Pitot-static probe velocity and the hot-wire velocity. For calibration, the reference Pitot probe was placed at either  $(X, Y, Z) = (0.29, 0.79, 0.37)$  m or at  $(X, Y, Z) = (1.08, 0.79, 0.37)$  m, depending on where the boundary layer measurement was taking place<sup>2</sup>. The hot-wire was then placed at  $(X, Y, Z) = (0.29\text{ or }1.08, 0.545, 0)$  m. To ensure the hot-wire was in the same streamwise plane as the Pitot-static probe, it was traversed in the streamwise direction until it crossed a laser sheet that illuminated the measurement plane. The location of the probe head was 88 mm from the plate surface ( $y/L = 0.096$ ), in the centerspan of the tunnel ( $z/L = 0$ ). The wind tunnel fan was operated at a range of speeds. At each tunnel velocity the wind tunnel operator

<sup>2</sup>The streamwise locations of the boundary layer surveys was limited by the range of the extending arm (Figure 2.8). The reference Pitot probe needed to be in the same slotted window blank that housed the hot-wire traversing system. The streamwise locations for the reference Pitot were  $X = 290$  and 1077 mm for the upstream and middle window slot locations, respectively.

recorded the reference pressures and ambient lab conditions. Calibration data (differential pressure and temperature from the reference Pitot probe and anemometer voltages) were sampled at 1 kHz for 10 seconds using the NI USB 6343 DAQ system for each tunnel speed. Differential pressure between the total and static pressures was measured using either the Scanivalve or Validyne transducer (see Section 2.4.2). First, the differential pressure voltage output from the transducer was calibrated to the tunnel Setra absolute pressure measurements using a linear fit, such as that shown in Figure 2.7. Using the calibration and Equations 2.2-2.4, the mean velocity sensed by the Pitot-static probe was assumed to be the same as that observed at the hot-wire. For several tunnel speeds, mean velocity measured by the Pitot were used to calibrate the hot-wire anemometry output voltage using a 5th order polynomial fit so that

$$U = aV^5 + bV^4 + cV^3 + dV^2 + eV + f, \quad (2.7)$$

where  $U$  is the mean velocity and  $V$  is the hot-wire anemometer voltage output, and  $a - f$  are polynomial coefficients that are adjusted to best fit the data. The 5th order polynomial fit was found to minimize the deviation between the calibration curve and the calibration points. A sample calibration fit between the velocity values obtained with the reference Pitot-static probe and the anemometer voltages is shown in Figure 2.10. Due to the dependence of the CTA technique on temperature, minor changes in tunnel freestream temperature could be confused with velocity changes. A procedure outlined by Hultmark et al. [27] was used to correct for any voltage shift caused by freestream temperature changes throughout the experimental run. The following equation was applied to the measured voltages  $E_{\text{meas}}$  to produce a corrected voltage  $E_{\text{cor}}$ :

$$E_{\text{cor}} = E_{\text{meas}} \left( \frac{T_w - T_{\text{cal}}}{T_w - T_{\text{meas}}} \right)^{1/2}, \quad (2.8)$$

where  $T_{\text{cal}} = 20.0^\circ\text{C}$  is the ambient fluid temperature at a reference calibration condition,  $T_{\text{meas}}$  is the temperature of the fluid during a measurement, and  $T_w$  is the temperature of the wire. The wire temperature is defined as

$$T_w = T_{\text{cal}} + \frac{OHR - 1}{\alpha} \quad (2.9)$$

where  $\alpha = 0.0036^\circ\text{C}^{-1}$  is the temperature coefficient of resistivity measured at  $20^\circ\text{C}$  for Tungsten, and  $OHR$  is the overheat ratio. The overheat ratio,  $OHR = R_w/R_a$ , represents the ratio between the wire resistance at operating temperature vs. ambient temperature. This was done for each calibration point as well as subsequent hot-wire runs (each wall-normal location within a boundary layer profile had a unique  $T_{\text{meas}}$  value).

The boundary layer traverse and data acquisition were controlled using the NI DAQ and interfaced using Matlab. To begin a boundary layer profile measurement, the hot-wire probe would first be traversed to the streamwise location of interest. The resolution of the traverse allowed spatial accuracy of  $\pm 1$  mm in the streamwise direction. The probe was then lowered down towards the plate using a second

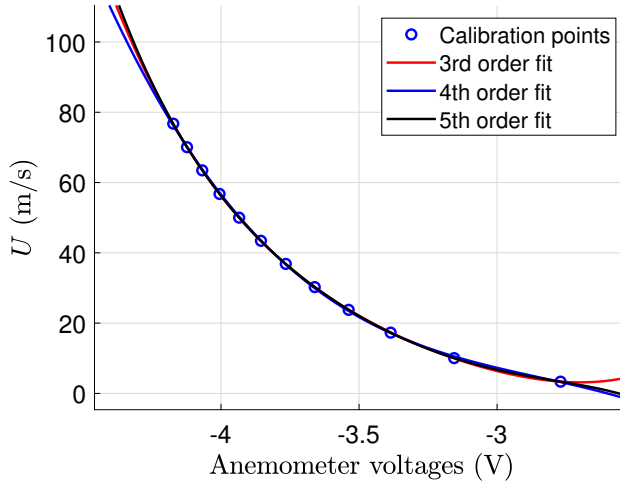


Figure 2.10. Sample calibration of the hot-wire using the velocity measured by a Pitot probe. A 3rd, 4th, and 5th order polynomial curve fit and the calibration points are shown.

wall-normal traverse actuator with a 0.05 mm step resolution. The initial location of the probe was determined by bringing the output velocity (from the converted anemometer voltages) to approximately  $0.30U_\infty$ , or 30% of the freestream velocity at that location. This was found to correspond to an initial  $y^+$  of about 10-15. Velocity data at each wall-normal location was sampled for 30 seconds at 20-40 kHz. Each profile contained 30-50 location positions, where the smallest stepping intervals were implemented near the wall and step sizes were increased as the external freestream velocity was approached. Freestream velocity was considered reached when the mean velocity of three adjacent locations were within 1.0% of each other. The external freestream velocity,  $U_e$ , for each profile in data processing was the mean of these three velocity values.

The uncertainty analysis for the hot-wire velocity measurements is provided in Appendix D.2. The uncertainty in the mean velocity measurements ranged between  $\varepsilon_U/U = 3.5$  to 8.1%, depending on the proximity of the measurement to the wall.

#### 2.4.4 Photogrammetric Oil-Film Interferometry

This section is based on the recent published work by Gluzman et al. [1]. For completeness, the details of the paper are provided herein. Skin-friction measurements are essential for characterizing and studying the topology of the flow fields. In aerodynamic studies, it is crucial for assessing viscous drag over flight vehicles and airfoil models [28], determining the position of separation [29, 30], location of laminar-turbulent boundary layer (TBL) transition [31, 32], and because of its high sensitivity to the velocity profile above the wall [33], it is often used in simulation validations

[34]. Of the available wall shear stress measurement techniques, image-based oil-film interferometry (OFI) [35] is one of the most accurate (typical uncertainty of up to 3 %) and reliable methods of measuring mean skin friction [36, 37]. Being versatile, accurate, relatively inexpensive and having a short setup time OFI is recommended to be the standard for mean skin friction measurements. It should be a part of all validation experiments conducted in wall-bounded flows where CFD performs poorly [38]. In this technique, an oil is applied to the model before the experiment with the wind tunnel off. When the wind tunnel is turned on the flow-induced shear thins the oil during the experiment. This localized thickness of the thin oil layer is used as an input to the thin-oil-film equation to obtain the local skin friction [39]. The method accuracy relies on the determination of the oil viscosity as a function of temperature during the experiment and the ability to accurately evaluate the end state of oil thickness (after the experimental run) from the acquired interferogram images by assessing the spacing between the fringes in the resulting fringe pattern [40]. The only significant errors in the OFI method are those that occur from measuring the oil viscosity and computation of fringe spacing from interferogram images [40, 41].

Recent advances in controlled temperature wind-tunnel experiments and the processing of the images using advanced digital acquisition and processing, such as the use of photogrammetry [42, 43] and improved analysis routines [44, 45] allows one to maintain an OFI accuracy of 2 – 3% (and even less than 1 % if great care is taken) in a wide range of imaging setups and complex test model geometries [46]. In particular, photogrammetry in OFI is used to determine the relationship between three-dimensional object coordinates and corresponding two-dimensional image coordinates to accurately obtain the oil thickness, for which precise camera incidence angle to each point in the interferogram on the model surface is necessary. The two-step photogrammetry approach discussed in [46], is used to eliminate the errors in determining the incidence angle due to surface curvature and also due to close camera proximity to the model surface. In addition, their approach allows for relaxing the requirement of precise measurement of camera location during testing and makes the computation of the incidence angle and model surface location for each point in the image plane straightforward. On models with significant surface curvature, such as the NASA bump model [34], the combined effects of camera proximity and model curvature made photogrammetry critical to calculating accurate skin-friction values.

However, there is some complexity in applying photogrammetry on a 3D surface. It requires knowledge of the model geometry or the tedious process of Cartesian model geometry reconstruction from images by using reference points on the model. The technique implemented in the present study was tailored to simplify this process. The technique, described in detail in Gluzman et al. [1], is a photogrammetry application on 3D surfaces without the need to know the model geometry or conduct Cartesian model geometry reconstruction via reference points.

The final formula to compute the skin friction following the formulations by Monson et al. [40] is given by

$$C_f = \frac{2n}{\lambda} \frac{\cos \theta_r \Delta x_f}{\int_0^{t_{run}} q_\infty(t) \mu_{oil}(t) dt}. \quad (2.10)$$

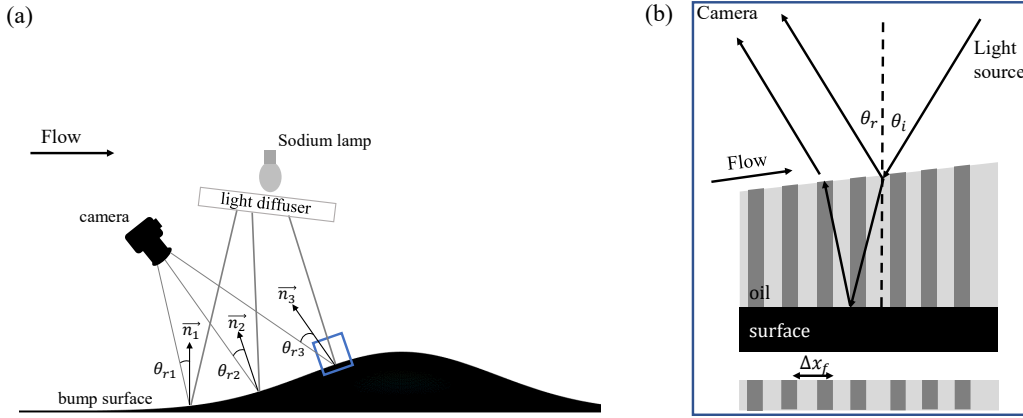


Figure 2.11. a) Test model with imaging setup, showing the impact of surface variation on refractive angle. (b) Zoomed in view of small surface area, which highlighted by blue rectangle in panel a, demonstrating the schematic of oil-film interference process. Reproduced from Fig. 1 of Gluzman et al. [1].

The above equation provides the relationship between the wall shear stress and the thinning of the oil-film where,  $\lambda$  is wavelength of the monochromatic light source,  $n$  is the index of refraction of the oil,  $\theta_r$  is the angle between the observation direction and the local surface normal, which is equal to the light incidence angle  $\theta_i$  as illustrated in imaging set up in Figure 2.11a and Figure 2.11b;  $\Delta x_f$  is the fringe spacing;  $t_{run}$  is the total run time of the wind tunnel;  $q_\infty(t)$  is the time variation of the dynamic pressure in the freestream flow region of test section; and  $\mu_{oil}(t)$  is the oil dynamic viscosity, which is a function of oil temperature during the duration of the experiment. More details on this equation can be found in [37] and its detailed derivation in [40] and [36]. To obtain the integral value  $\int_0^{t_{run}} q_\infty(t) \mu_{oil}(t) dt$  in the denominator of Equation (2.10), the time history of the dynamic pressure and model temperatures were acquired during the experimental run. Whereas the value of  $\cos \theta_r \Delta x_f$  in the nominator of Equation (2.10) is evaluated from the images of the resulting oil pattern after the experimental run, by using the simplified photogrammetry technique.

Prior to running the tunnel, a test surface was prepared so that it was optically smooth and reflective. A  $25.4 \times 51.2$  mm strip of 5 mil (0.005 in) Kapton tape was applied on the aluminum surface. The coating reflects light with about the same intensity as the air-oil interface, so a fringe pattern would be observed in the sheared oil at the end of the experiment. The enumerated orange rectangles in Figure 2.12 indicate the region where oil was applied over mounted Kapton tape surfaces. OFI measurements of skin friction were obtained along with the centerline downstream of the bump, where the skin friction lines are parallel to the streamwise direction, as shown by the superimposed surface flow visualization in Figure 2.12. Whereas, the uniformity of the streamlines upstream of the bump apex allowed for off-span samples

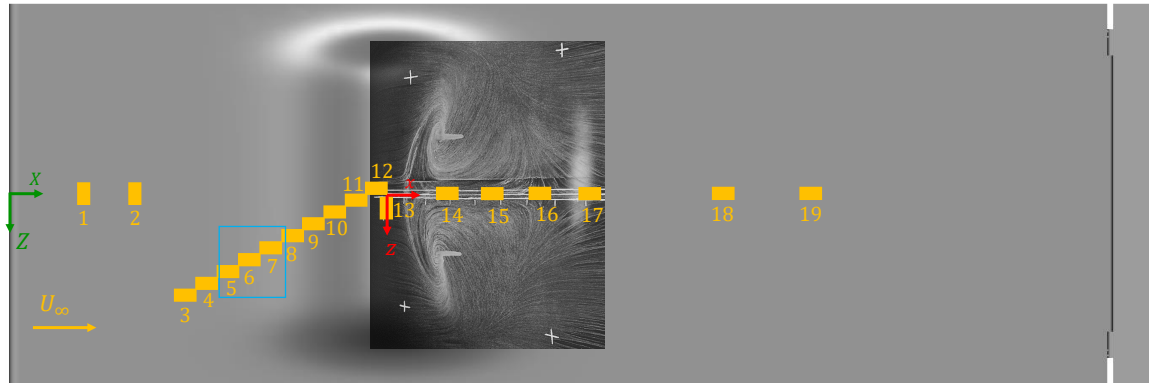


Figure 2.12. Top view of the bump model in Configuration A. The enumerated orange rectangle patches indicate the region where oil was applied over mounted Kapton tape surfaces. A fluorescent oil visualization image is superimposed onto the graphic to show the skin friction lines.

Reproduced from Fig. 2a of Gluzman et al. [1].

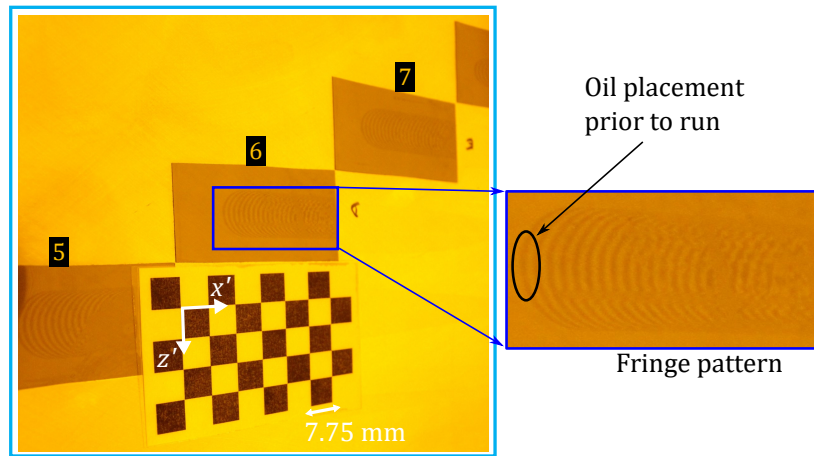


Figure 2.13. Fringe patterns after an experimental run at locations 5-7 in the highlighted blue rectangle region in Figure 2.12 and nearby checkerboard (7.75 mm square size), where we denote its local  $x'$ - $z'$  coordinate system. Reproduced from Fig. 4 of Gluzman et al. [1].

to better resolve the streamwise skin friction profile upstream of the bump in a single experimental run. A small flexible checkerboard with 7.75 mm squares was mounted near the oil patch. The checkerboard served as a local calibration board, used in the simplified photogrammetry procedure to compute  $\cos \theta_r \Delta x_f$  with high accuracy. Oil viscosity was chosen based on tunnel running conditions. The viscosity affected the fringe spacing at the end of the test, where less viscous oils will yield fringe patterns with longer wavelengths. Figure 2.13 shows the post-run fringe pattern from an oil droplet placed on the upstream edge of a Kapton strip. The application of small oil patches (a small drop or line segment) was made at a series of locations of interest on the model surface, such that it did not run into another patch, which can destroy the resulting fringe pattern.

Once the setup preparations were complete, the tunnel was closed, and the experiment started. The time histories of the dynamic pressure and model temperatures during the run were recorded. At low Mach numbers for which the aerodynamic heating of the surface is negligible, a thermocouple probe and pressure probe can be mounted in the freestream. In this study, a typical run of an experiment was about 20-30 min to allow the oil to shear and reach its final state, where 200 cSt, 1000 cSt, and 5000 cSt oil viscosities were used depending on local flow conditions. After the experiment ended, the test section was opened, and an imaging setup was installed. The setup includes a monochromatic light source and a camera (see illustration in Figure 2.11a). At least three images of the oil pattern and checkerboard were captured from different angles. The camera lens was zoomed out and set to Manual mode to avoid auto-focusing the camera in order to sustain the same intrinsic camera parameters for each image. After running the experiment, a fringe pattern was created, as photographed in Figure 2.13. The interference pattern was captured after illuminating the surface with a Sodium lamp with a wavelength of 589 nm. In this case, the images were obtained with Canon Rebel T6 camera combined with Canon EFS 18-55 mm lens.

To obtain the integral value ( $\int_0^{t_{run}} q_\infty(t) \mu_{oil}(t) dt$ ) in the denominator of Equation (2.10), the time history of  $\mu_{oil}(t)$  [Pa s] was evaluated. In this study, Clearco silicon oils were used. The computational expression (curve fit) that was provided in Clearco's viscosity to temperature charts data-sheet was given by

$$\mu_{oil}(T(t)) = \rho \times 10^{-6 + \frac{763.1}{273.16 + T} - 2.559 + \log(\nu_0)}. \quad (2.11)$$

Here  $\rho_0$  and  $\nu_0$  are oil density [ $kg/m^3$ ] and oil dynamic viscosity [cSt], respectively, both at 25 °C. Three Clearco oils were used with different properties. The first having  $\nu_0 = 200$  cSt,  $n = 1.4026$ , and  $\rho_0 = 969$   $kg/m^3$ ; the second was more viscous having  $\nu_0 = 1000$  cSt,  $n = 1.4031$ , and  $\rho_0 = 974$   $kg/m^3$ . A high viscosity oil was also tested having  $\nu_0 = 5000$  cSt,  $n = 1.4035$ , and  $\rho_0 = 975$   $kg/m^3$ . A K-type thermocouple located in the freestream reference Pitot probe was used to obtain temperature readings at 10 Hz.

The images that capture the checkerboard with the nearby fringe pattern are used to accurately obtain the  $\cos \theta_r \Delta x_f$  term in the nominator of Equation (2.10). The simplified photogrammetry technique employs camera calibration algorithms for

estimating camera intrinsic, extrinsic, and distortion parameters to accurately obtain  $\theta_r$  and  $\Delta x_f$ , without knowledge a priori of the surface geometry and camera position. In particular, a set of functions that are available in the Computer Vision Toolbox in MATLAB R2020a were used. The procedure steps are described in detail by Gluzman et al. [1], and is summarized in Appendix B.

After each of the steps were applied, the skin friction was computed using the obtained sensor and imaging data. The uncertainty analysis is outlined in Appendix D.3. The overall bias error in the mean skin friction measurements was determined to be within 2%.

#### 2.4.5 Particle Image Velocimetry

The implementation of tracing particles to visualize flow phenomena dates back to the earliest wind tunnel experiments. The rapid improvement of optical imaging technology and digital image processing over the course of the 20th century led to the well known experimental technique known as particle image velocimetry (PIV [47, 48]). The documentation of the PIV technique into the commercially available software DaVis is extensive [49, 50, 51, 52], and only the fundamental processes will here be outlined. The general basis for the use of PIV in a wind tunnel applications is the summation of a few basic principles. First, the flow must be seeded with a some kind of tracing substance whose individual particles follow the natural path of the fluid without obstructing it. These particles must be illuminated to allow for imaging. In the case of this experiment, lens elements diverge a laser beam into a light sheet to illuminate a measurement plane. The light scattered from the tracing particles needs to be recorded. The measurement plane is illuminated twice within a short interval, and the light scatter is subsequently captured twice using a CMOS camera<sup>3</sup>. The physical displacement of the particle field is determined through the evaluation of the PIV recordings, along with the calibrated relationship between the image plane and the measurement plane. Post-processing can be used to detect and eliminate invalid measurements, and to pull out flow quantities of interest. This non-intrusive flow diagnostic technique is very valuable in capturing whole fields of velocity data. However, it involves the tedious tuning of many parameters. Some of the challenges include the distribution and density of the seeding material within the flow, maximizing the intensity of the light used to illuminate the particles in the flow, and configuring the cameras and lenses to the necessary focal lengths and field of fields (FOV). Other considerations include the duration between and the length of the light pulses, reducing surface reflection and background noise, and the trade-off between spatial and temporal resolution. This section provides the final culmination of the PIV steps used to best quantify the flow features over the bump.

A 2D PIV setup was used to investigate  $x - y$  planes of the downstream bump region, whereas SPIV was used to obtain the  $z - y$  cross-planes. The former is discussed next, whereas the later is described in Section 2.4.6.1. The 2D PIV setup

---

<sup>3</sup>Two cameras are used in the case of stereoscopic PIV, as described in Section 2.4.6

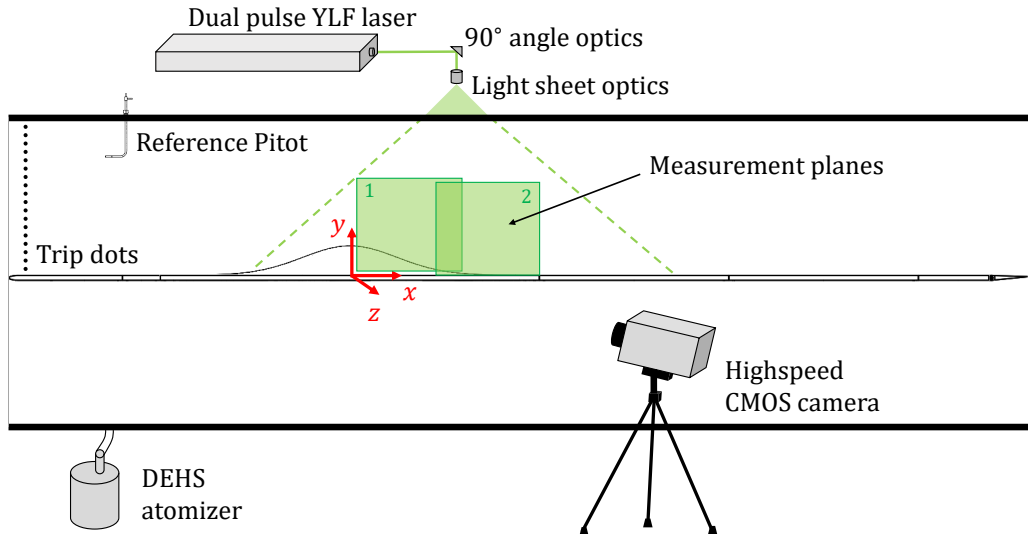


Figure 2.14. Diagram of the PIV setup used to obtain  $x - y$  flow field planes in the downstream bump region.

used to investigate the separated flow over the bump is shown in Figure 2.14. The measurement plane for the PIV was illuminated using a Litron dual pulse LDY300 527 nm wavelength laser with a neodymium-doped yttrium lithium fluoride (YLF) lasing medium. The output energy of the laser was 35 mJ for a 0.2 kHz pulsing frequency, and the D86 width of the beam was 5 mm. The beam was redirected from the laser housing using three 90° angle optics. The beam was passed through a light sheet optic to diverge the beam into a sheet illuminating a single  $x - y$  plane of the flow through a clear acrylic sheet stock optical window on the top of the test section. The spanwise location could be adjusted to acquire measurements at various spanwise distances from the test section centerline. The location of the light sheet was set to an approximate  $x$  location downstream of the bump apex and oriented within  $\pm 0.5$  mm of the desired spanwise location within the tunnel. This was done using a micrometer to measure the center of the light sheet at both edges of the optical window prior to calibration and testing. The sheet optic was adjusted to focus the beam so that the light sheet had its minimum thickness at the bump surface. The flow was seeded using di-ethyl-hexyl-sebacate (DEHS) that was atomized using a Laskin-Nozzle aerosol generator fed into the test section using a 25 mm OD tube under the splitter plate. After several seconds of pressurizing the DEHS with 10-40 psi pressure differential while running the tunnel, the particles were uniformly distributed throughout the test section. Typical sizes for DEHS particles are on the order of  $1 \mu\text{m}$ .

A  $0.9 \pm 0.01$  mm thick black matte 3M wrap film series 2080 made of cast vinyl

was adhered to the bump surface at the measurement locations to reduce surface reflections caused by the laser. The color and glossiness was chosen after a series of tests conducted on a variety of wrap options. The lowest level of laser reflection intensity was measured using "Matte Black" (M12). Black matte spray paint was used to black out the reflective side walls and window blanks in the background of the camera images. Several other anti-reflection devices were used outside of the test section to reduce glare from the laser beam exit location and optical windows.

Images were taken through a side window using a high speed Photron Fastcam SA1.1 that features a 12-bit CMOS sensor with  $20\ \mu\text{m}$  pixels and a square aspect ratio of 1024x1024 pixels. The lens used was a Nikon micro-Nikkor with a focal length of 55 mm and an *f*-stop of 3.5 for its aperture. To properly capture the full streamwise extent of the global flow field from separation to reattachment, two separate camera setups, or regions of interest (ROI), were used to acquire data with nearly identical testing conditions at each spanwise location. The mean data were then stitched together after post processing. The two ROI positions allowed for an overlap between images of about 20% of the stitched flow field. Some columns and rows of the post-processed data were removed for a smooth transition between ROIs, and to remove some noisy areas on the corners caused by reflections and poor light sheet intensity values. Five spanwise locations were investigated using PIV, and are shown in Figure 2.15. The measurement planes were located at  $z/L = -0.250$ , -0.167, -0.083, 0.000, and 0.083. The stitched data gave a measurement field from  $x/L \approx 0.03$  to 0.50 in the streamwise direction, and vertically from the bump surface to  $y/L \approx 0.2$ .

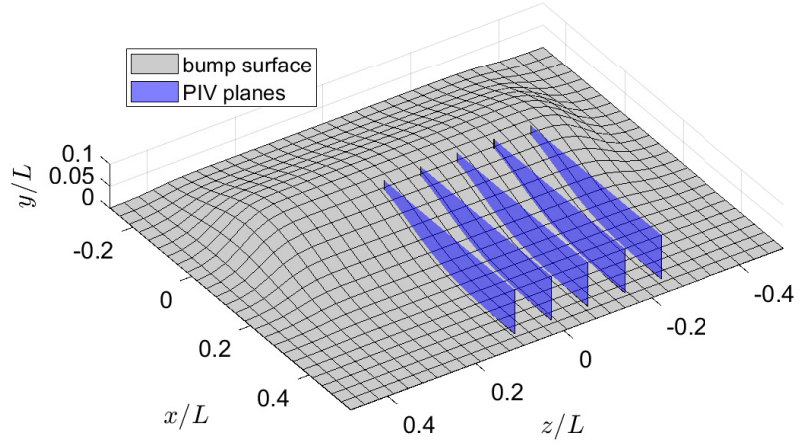


Figure 2.15. PIV measurement plane locations.

For each camera setup ROI, three sets of 1000 image pairs were taken at a frequency of 0.2 kHz. Furthermore, each of the three 5 second sets of the velocity data were independent, ensuring a proper time average of any low frequency periodicity caused by the recirculation or the tunnel acoustics. This averaging process also reduced the required processing and storage cost of the experiment. The lower data rates ensure that the samples are independent, with low correlation between samples. A thorough discussion of the uncertainty propagation of the calculated PIV quantities is given by Sciacchitano and Wieneke[53], and is briefly summarized in Appendix D.4. While the instantaneous velocity measurements are not discussed, the knowledge of the individual velocity fields were required for the computation of uncertainties, particularly for the turbulent fluctuations.

Calibration to the measurement plane was required to reduce perspective distortions in the images. A single plane,  $100 \times 100$  mm calibration board had 0.5 mm diameter dots that were located 2.5 mm from one another in both the  $x$  and  $y$  directions. The calibration board was placed so that it was near the center of the image ROI. LaVision PIV software (DaVis version 8.4) was used to calibrate the image plane to the laser plane after the light sheet was aligned to the calibration board, and the camera was focused on the dots. Since the origin of the measurement plane was set to the center of the calibration plate, the physical distance of the plate in the test section was carefully measured. The calibration uncertainty and conversion scales were recorded for each spanwise plane, and are shown in Table 2.1 (averaged over the two ROI calibrations at each spanwise location). Since the camera was on the positive  $z$  side of the test section, the scale decreases slightly as the measurement plane moves away from the camera towards the negative  $z$  wall.

TABLE 2.1

CALIBRATION UNCERTAINTY AND CONVERSION FACTORS FOR  
EACH SPANWISE CAMERA SETUP OF THE PIV EXPERIMENT.

$z/L$	$\epsilon_{\text{cal}}$ [pixel]	scale [pixel/mm]
0.083	0.064	4.19
0.000	0.049	4.08
-0.083	0.075	4.00
-0.167	0.061	3.88
-0.250	0.059	3.56

The pixel window size chosen for the double-frame cross-correlation[48] was 24 pixels, with 25% overlap to increase the spatial resolution. The accuracy of the particle shift measurement in each pixel window depends on the peak in the correlation function between subsequent frames. The cross-correlation function[47] is given by the expression

$$\Phi(dx, dy) = \sum_{i=0}^{K-1} \sum_{j=0}^{M-1} I_1(i, j)I_2(i + dx, j + dy), \quad (2.12)$$

where  $K$  and  $M$  are the dimensions of the interrogation window, and  $I_1$  and  $I_2$  are the measured intensity values in the first and second frames of an image pair. The position of the maximum value of  $\Phi$  provides the direction and distance of particle displacement for the given interrogation window.

The location of a particle can be estimated down to 0.1 pixels using an Airy intensity function, which maps the sub-pixel location of the peak in the correlation using a three-point Gaussian estimator[54]. Bias errors arise when the particles size in the images are < 1.5 pixels. This is called "peak locking", where the particle locations are locked to integer values of pixels[55]. Efforts to reduce peak locking include slightly defocusing the image to increase the particle size.

Some pre-processing was done on the raw particle image pairs for the purpose of removing the majority of the reflection noise, and to correct for the inherent elliptical shape of the beam prior to its distribution through sheet optics. A time filter was used to remove background noise. A Gaussian average was computed and subtracted from the intensity field of the raw source images every five images. Large background intensity fluctuations were filtered with a 4 pixel length scale for a constant background level. Particle intensities were normalized using a 5 pixel length min-max filter. After the images were corrected to the physical measurement plane via the calibration, a mask was used to remove any data below the surface the bump, especially the specular reflections on the bump surface from the vertical light sheet.

Once the PIV correlation function provided instantaneous velocity fields, a median filter was used to remove spurious vectors [56]. Three passes of the filter identified an outlier vector if its value was  $> 3$  standard deviations from its 8 surrounding neighbors. If it was identified as an outlier, the spurious vector would be replaced using interpolation.

Time averaging was done on the 3000 post-processed vector fields to acquire time-mean quantities for the mean flow ( $U$  and  $V$ ), as well as the Reynolds stresses ( $\overline{u'u'}$ ,  $\overline{v'v'}$ , and  $\overline{u'v'}$ ) for each of the flow conditions. The scalar fields were set to reject values that were  $> 3$  standard deviations from the temporal mean. This was done to remove any largely spurious vectors that survived the median spatial filter. An anisotropic denoising procedure [57] was implemented to reduce noise while preserving true velocity intensities.

The uncertainty quantification for PIV is still not an exact science, and the errors can propagate very differently from one experiment to another, and is an entire research topic unto its own. The calculation of the uncertainty (discussed in Appendix D.4) is limited to the random uncertainties following the framework of Sciacchitano

and Wieneke [53]. More thorough explanations of the other uncertainties that can be present in PIV experiments can be found in various publications [58, 59, 47, 60].

#### 2.4.6 Stereoscopic Particle Image Velocimetry

Stereoscopic particle image velocimetry (SPIV [61, 47]) is an experimental method for acquiring three-component velocity fields within a plane, including mean and fluctuating parts. Similar to single camera two-dimensional particle image velocimetry (2D PIV), SPIV utilizes a pulsed laser to illuminate seed particles within the measurement plane at two instances in time and cameras to capture the particle locations within the plane. SPIV differs from 2D PIV in that a minimum of two cameras are required and those cameras must have different perspectives of the same particles so that the third (out-of-plane) component of velocity may be computed using a stereoscopic cross-correlation algorithm. The reconstruction of the three-component velocity field is dependent on the perspective distortion of the displacement vector viewed by two cameras from different direction.

Two separate experiments were conducted using SPIV. For both, the hardware used was identical to that described in Section 2.4.5, with the addition of a second camera. The following subsections provide the setup procedure for both of the experiments.

##### 2.4.6.1 Downstream Cross-planes

The first SPIV experiment was conducted downstream of the bump apex so that the measurement planes were perpendicular to the flow direction, i.e., in cross-plane cuts. The laser and camera setup for this case is shown in Figure 2.16. For this cross-plane case, the laser (as described in Section 2.4.5) was introduced into the flow non-intrusively through a clear acrylic sheet stock optical window from the  $-z$  side of the test section. The beam was passed through a light sheet optic to split the beam into a sheet illuminating a single  $z - y$  plane of the flow. The laser housing was placed onto a hydraulic jack so that the vertical location of the beam exit could be adjusted to the center of the measurement plane. The location of the light sheet was set to the desired  $x$  location where its center was within  $\pm 0.5$  mm of the intended measurement plane, using a micrometer at both test section side windows. The sheet optic was adjusted to focus the beam so that the light sheet has its minimum thickness at the center of the measurement plane ( $z = 0$ ).

In order to achieve the highest correlations in particle images and lowest stereo reconstruction error, the two cameras were placed on opposite sides of the wind tunnel test section, pointed upstream at the same side of the measurement plane. The angle  $\theta_c$  between cameras was between 90 and 98°, depending on the streamwise location of the measurement plane. Scheimpflug adapters were installed onto the cameras to create an angle between the camera's sensor plane and the plane of the lens. By tilting the lenses using the adapters by an angle  $\phi$ , perspective distortion was reduced using the Scheimpflug principle [62, 63]. Camera A was a 1 mega pixel Photron Fastcam SA1.1 that features a 12-bit CMOS sensor with 20  $\mu\text{m}$  pixels and a square aspect

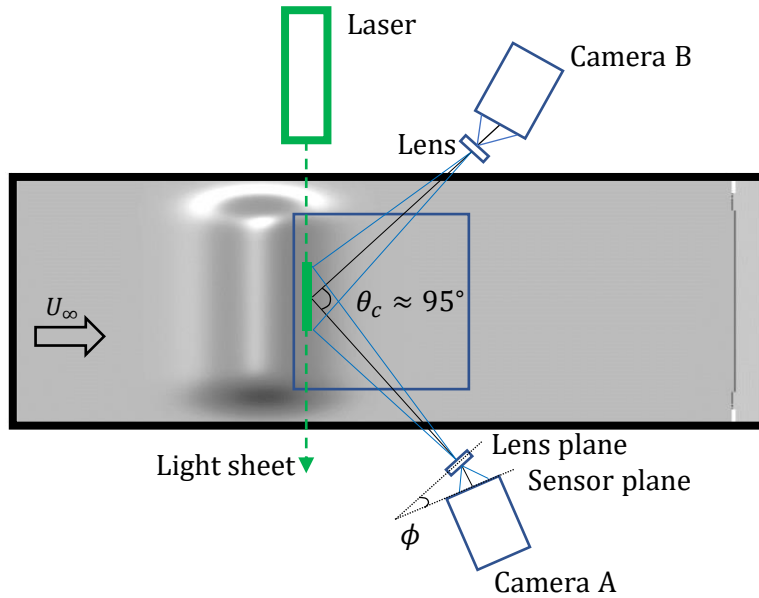


Figure 2.16. Top view diagram of SPIV cameras (with Scheimpflug adapters creating an angle  $\phi$  between the camera and lens) and laser setup to sample a cross-plane velocity field on configuration A.

ratio of  $1024 \times 1024$  pixels. The camera was affixed with a Nikon AF Nikkor 50 mm lens set to an  $f$ -stop of 1.4. The lens was attached to a  $2\times$  teleconverter. Camera A was placed on the opposite side of the test section to the laser to receive the forward light scatter from the tracing particles. Camera B was a 4 mega pixel Phantom v1840 with  $13.5\text{ }\mu\text{m}$  pixels which was binned down to 1 mega pixel resolution so that the pixels became  $27\text{ }\mu\text{m}$  with an aspect ratio of  $1024 \times 976$  pixels. A 75-300 mm telephoto lens set to  $\sim 120$  mm was used to capture the backward light scatter at an  $f$ -stop of 4.5.

Four streamwise planes were interrogated using the testing setup described above, as shown in Figure 2.17. Measured from the bump apex, the streamwise locations were  $x/L = 0.208, 0.250, 0.306$ , and  $0.361$ . The measurement planes spanned from  $z/L = \pm 0.131$ , and vertically from the bump surface to  $y/L = 0.11$ .

Prior to running the tunnel up to test conditions, calibration to the measurement plane was conducted. A two-level 204 mm square 204-15 LaVision calibration target was placed near the measurement plane using a Thorlabs two-axis adjustment platform. The cameras were adjusted on three-axis tripod mounts on three-axis rail and focused to produce similar field of views (FOV) with minimal perspective distortion. Figure 2.18 shows the FOV and calibration planes for one of the streamwise locations. The blue grid indicates the front plane, and the green grid is the back plane which

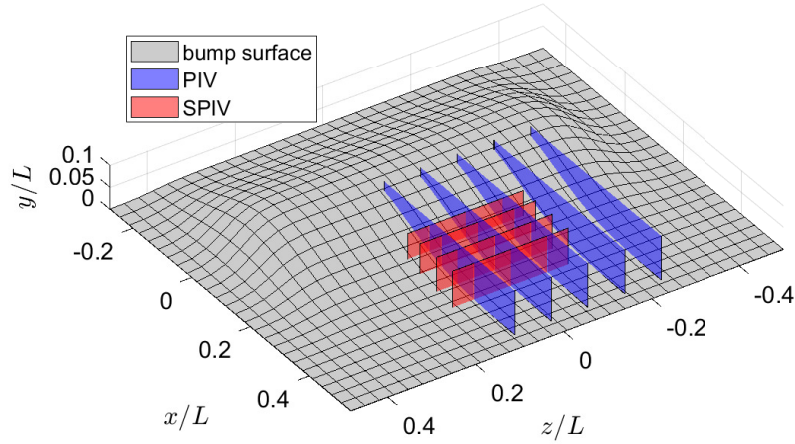


Figure 2.17. SPIV measurement plane locations.

is offset by 2 mm.

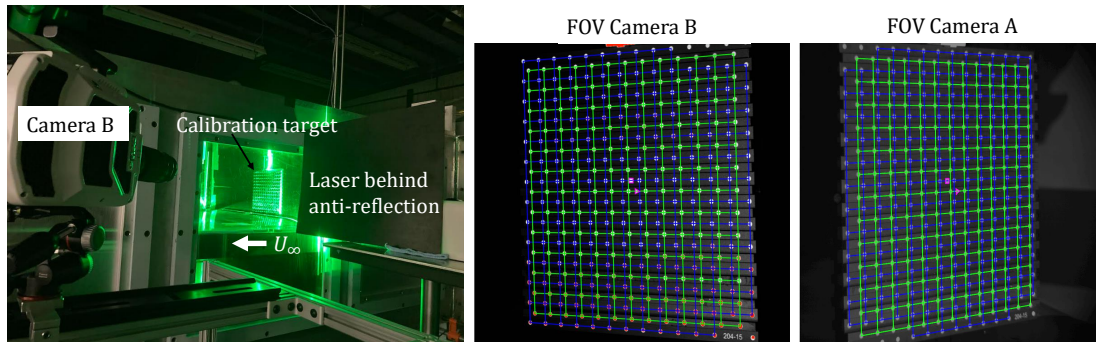


Figure 2.18. Side view of the test section with the calibration plate aligned with the laser light sheet illuminating the  $x/L = 0.208$  plane and the resultant calibration images taken by both of the cameras.

A third order polynomial fit to the calibration target dots was done through

the optical windows for each of the cameras to produce a direct pixel to spatial relationship. Next, DaVis version 12 planar self-calibration was conducted on a particle image taken by both cameras at a single point in time. This was done to remove the apparent particle disparity caused by an imperfect initial calibration. A diagram showing how a particle could have an apparent disparity with a minor laser misalignment is shown in Figure 2.19a. The resultant disparity map prior to self-calibration is shown in Figure 2.19b.

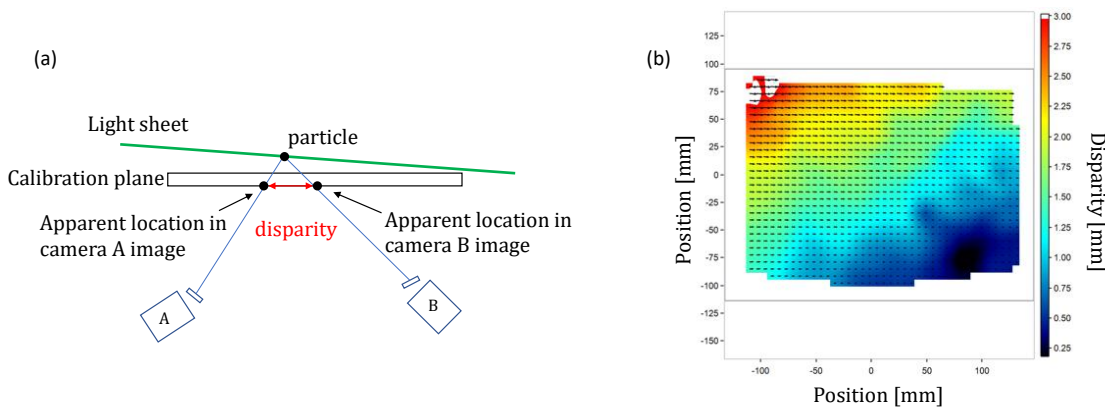


Figure 2.19. (a) Diagram showing apparent disparity in particle measurements with misalignment between the calibration plane and laser plane and (b) the resultant disparity field for a single particle field which defines the correction to be applied by the planar self-calibration.

Table 2.2 gives the angle between cameras for each calibration, as well as the final scale factor relating the pixel size to physical coordinates. The dewarped image size domain after mapping onto physical space is also given; the data was trimmed post calibration.

Particle image pairs were acquired simultaneously using a LaVision external programmable timing unit (PTU-X). The PTU had a 10 ns time resolution, jitter less than 50 ps, and variable cyclic triggering channels. Two-frame, single exposure image pairs were acquired at 0.2 kHz over 25 seconds for 5000 data points. The Litron laser utilized a Q-switch trigger with a 5.0  $\mu$ s pulse duration for both beam pulses. Illumination duration of the dual cavity laser system was 0.1  $\mu$ s. For the  $Re_L = 4.0 \times 10^6$  case, the delay between pulses, and thus image pairs, was  $\delta t = 10.0 \mu$ s.

TABLE 2.2

SPIV CROSS PLANAR CALIBRATION ANGLES BETWEEN  
CAMERAS, CONVERSION FACTORS FOR CALIBRATION  
MAPPING, AND RESULTANT DEWARPED IMAGE SIZE FOR EACH  
CROSS-PLANES.

$x/L$	$\theta_c$	Scale Factor [px/mm]	Dewarped image size [mm $\times$ mm]
0.208	88.6°	5.36	272 $\times$ 192.8
0.250	91.8°	5.10	271 $\times$ 205.7
0.306	96.1°	5.29	276 $\times$ 194
0.361	102.9°	5.72	267.9 $\times$ 185.9

For each of the particle images, pre-processing was done prior to cross correlation. For each pixel in the image, the intensity over the entire data set was averaged and subtracted from each image to eliminate background noise and large reflections caused by the laser on the bump surface [64]. The image was then divided into square interrogation windows with 48 pixel lengths. To maximize the spatial resolution, an 87.5% overlap was used between adjacent interrogation windows. A single SPIV vector calculation (single pass) [61] was done for each of the windows. For vector validation, a universal outlier detection algorithm [65] was run on the resulting vector field to reject and replace spurious vectors in the flow field. By averaging over the 5000 instantaneous vector field measurements the mean and turbulence flow field statistics were obtained and analyzed.

Uncertainty in the flow velocities computed using the stereoscopic cross-correlation algorithm in LaVision's DaVis 12 software was quantified using the correlation statistics method also implemented within DaVis [59].

#### 2.4.6.2 Upstream Flow Development

The second SPIV experiment was conducted upstream of the bump apex so that the measurement planes were parallel to the flow direction. The laser and camera setup for this case is shown in Figure 2.20. The beam in this case was redirected from the laser housing using three 90° angle optics. The beam was passed through a light sheet optic to split the beam into a sheet illuminating a single  $x - y$  plane of the flow from the top of the test section. The location of the light sheet was set to an approximate  $x$  location and oriented within  $\pm 0.5$  mm of the centerspan of the

tunnel ( $z/L = 0$ ). This was done using a micrometer to measure the center of the light sheet at both edges of the optical window prior to calibration and testing. The sheet optic was adjusted to focus the beam so that the light sheet had its minimum thickness at the bump surface.

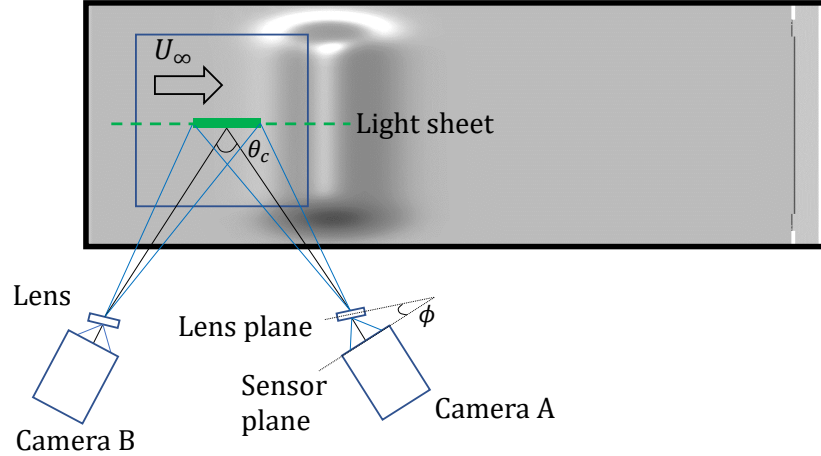


Figure 2.20. Top view diagram of SPIV cameras (with Scheimpflug adapters creating an angle  $\phi$  between the camera and lens) and laser setup to sample an upstream velocity field on bump configuration A. The angle between cameras is denoted by  $\theta_c$ .

The two cameras were placed on the same side of the wind tunnel test section, viewing in the  $-z$  direction so that flow moved from left to right with respect to the viewing angle. The angle between cameras ( $\theta_c$ ) was between 19 and 63°, depending on the streamwise location of the measurement plane and the optical access from the side wall. Camera A was a 1 mega pixel Photron Fastcam SA1.1 that features a 12-bit CMOS sensor with 20  $\mu\text{m}$  pixels and a square aspect ratio of 1024×1024 pixels. The camera was affixed with a Nikon Micro AF Nikkor 105 mm lens, set to an  $f$ -stop of 2.8. Camera B was a 4 mega pixel Phantom v1840 with 13.5  $\mu\text{m}$  pixels, which was binned down to a 1 mega pixel resolution so that the pixels became 27  $\mu\text{m}$  with an aspect ratio of 1024×976 pixels. A Nikon AF Nikkor 28-105 mm lens with a minimum  $f$ -stop of 1.8 was used. A focal length doubler was implemented on Camera B to match the FOV of Camera A. Scheimpflug adapters were installed onto the cameras to create an angle between each camera's sensor plane and the plane of

the attached lens. By tilting the lenses using the adapters by an angle  $\phi$ , perspective distortion was reduced by applying the Scheimpflug condition [63].

Prior to running the tunnel up to test conditions, calibration to the measurement plane was conducted. A two-level 106 mm square 106-10 LaVision calibration target was aligned with the  $z/L = 0$  plane at several streamwise positions. The cameras were adjusted on three-axis tripod mounts on three-axis rail and focused to produce similar FOVs. Figure 2.21 shows the calibration target installed in the tunnel for the upstream-most position, for the bump configuration A. In this case, the target is on the flat plate portion of the bump. The streamwise and spanwise location of the calibration plate was measured using a micrometer. Its vertical center was the half height of the calibration plate. This process was done for each interrogation region prior to calibration.

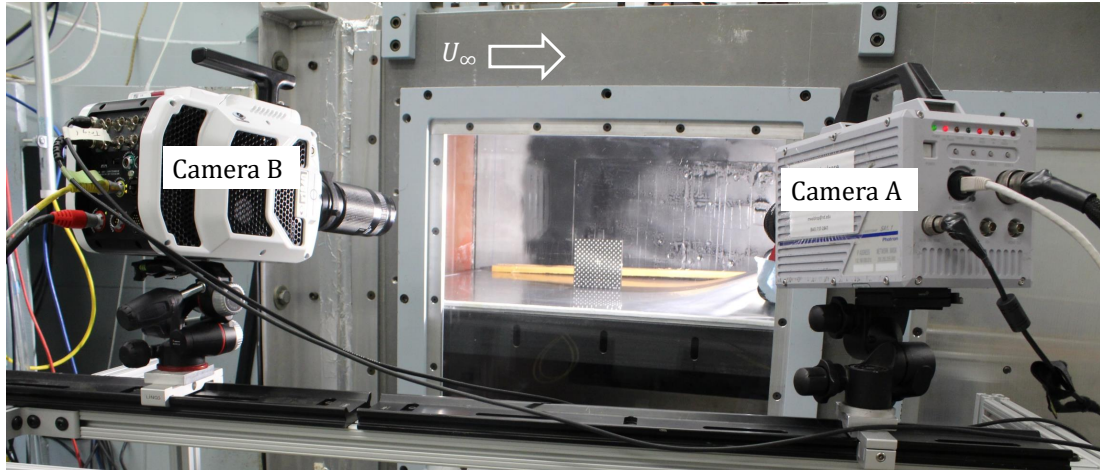


Figure 2.21. Photograph of the side view of the test section in bump configuration A. Both cameras were focused on the LaVision 106 mm two-plane calibration target placed on the flat surface upstream of the bump curvature.

A third order polynomial fit to the calibration target dots was done through the optical windows for each of the cameras to produce a direct pixel to spatial relationship. Next, DaVis version 12 planar self-calibration was conducted on a particle image taken by both cameras at a single point in time. This was done to

remove the apparent particle disparity caused by an imperfect initial calibration, as shown in Figure 2.19.

Three interrogation regions in the  $x - y$  plane on the tunnel centerline were interrogated using the testing setup described above for configurations A and B. The exact locations of the interrogation regions changed between configurations. The three positions reflected the need to identify the boundary layer upstream of the bump curvature, its acceleration leading up to the apex, and an additional position in between them. Table 2.3 provides the streamwise position of each of the interrogation windows for each bump configuration. The notation  $x_i$  and  $x_f$  denotes the upstream and downstream edges of the measurement window, respectively. The calibration angles and scale factors between the image size and the physical measurement planes are also included.

TABLE 2.3

SPIV MEASUREMENT LOCATIONS, CALIBRATION ANGLES  
BETWEEN CAMERAS, AND CONVERSION FACTORS FOR  
CALIBRATION MAPPING.

Config.	Location #	$x_i/L$	$x_f/L$	$\theta_c$	Scale Factor [px/mm]
A	1	-0.42	-0.31	56.1°	9.02
A	2	-0.24	-0.13	36.6°	9.39
A	3	-0.10	0.00	32.3°	8.93
B	1	-0.57	-0.43	62.7°	9.15
B	2	-0.27	-0.15	34.9°	9.93
B	3	-0.10	0.00	19.9°	9.37

Particle image pairs were acquired simultaneously using a LaVision external programmable timing unit (PTU-X). The PTU had a 10 ns time resolution, jitter less than 50 ps, and variable cyclic triggering channels. Two-frame, single exposure image pairs were acquired at 0.2 kHz over 25 seconds for 5000 data points. The Litron laser utilized a Q-switch trigger with a  $5.0 \mu\text{s}$  pulse duration for both beam pulses. Illumination duration of the dual cavity laser system was  $0.1 \mu\text{s}$ . For the  $Re_L = 4.0 \times 10^6$

the delay between pulses, and thus image pairs, was  $\delta t = 12.0 \mu\text{s}$ .

For each of the particle images, pre-processing was done prior to cross correlation. For each pixel in the image, the intensity over the entire data set was averaged and subtracted from each image to eliminate background noise and large reflections caused by the laser on the bump surface [64]. SPIV vector calculations [61] were done using a multi-pass function for each of the windows. A first pass of 64 pixel length windows was implemented with 50% overlap, then three passes with 16 pixel length windows using 75% overlap was run to increase spatial resolution. For vector validation, a universal outlier detection algorithm [65] was run on the resulting vector field to reject and replace spurious vectors from the flow field. Scalar fields were then averaged over the 5000 vector fields, and resulting mean and turbulence statistics were obtained and analyzed. An anisotropic denoising procedure [57] was implemented to reduce noise while preserving true velocity intensities.

Uncertainty in the flow velocities computed using the stereoscopic cross-correlation algorithm in LaVision's DaVis 12 software was quantified using the correlation statistics method also implemented within DaVis [59].

#### 2.4.7 Instrumented Bump

##### 2.4.7.1 Surface Static Pressure Taps

The pressure field over the Boeing bump was quantified using an array of 94 static pressure taps along several streamwise and spanwise planes. The pressure coefficient  $C_p$  was used to normalize the pressure field to the dynamic pressure of the freestream, so that

$$C_p = \frac{\Delta P_i}{q_\infty} = \frac{P_i - P_\infty}{\frac{1}{2}\rho U_\infty^2} = \frac{P_i - P_\infty}{P_0 - P_\infty}, \quad (2.13)$$

where  $P_i$  is the local static pressure on the surface of the bump,  $P_\infty$  and  $P_0$  are the freestream static and total pressures taken by the reference Pitot-static probe upstream of the bump, respectively. The locations of the static pressure taps were chosen with high enough resolution to determine the streamwise pressure gradients at the centerspan  $z/L = 0$ , as well as two offspan planes of  $z/L = 0.083$  and  $0.167$ . Similarly, spanwise arrays of pressure ports were placed along the apex of the bump  $x/L = 0$ , as well as on the streamwise geometric inflection point  $x/L = 0.138$ – a location of interest due to the change in sign of the surface curvature from concave to convex. Figure 2.22 shows the top view of the location of the pressure taps on the bump from a top view. The locations of the taps are given in the appendix.

The pressure ports have sufficient spatial resolution to determine the pressure gradients and their derivatives ( $dC_p/dx$  and  $d^2C_p/dx^2$ ). The spatial resolution of the streamwise arrays are also higher near the bump apex in order to capture the location of the peak  $C_p$ . For configuration A, a spacing plate with three additional static pressure taps was placed upstream of the bump section to quantify the pressure gradient of the flow before it encountered the bump geometry at  $x/L = -0.632$ ,  $-0.611$ , and  $-0.590$ . For configuration B the spacing plate was placed downstream of the bump section so that the three ports were located at  $x/L = 0.590$ ,  $0.611$ , and  $0.632$ .

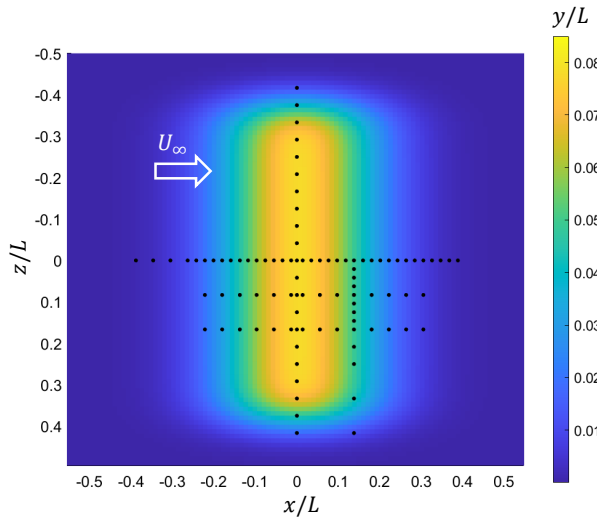


Figure 2.22. Top view of bump section with locations of the static pressure ports shown by black dots with flow from left to right.

The static pressure ports were machined normal to the local wall surface and had a diameter of 0.79 mm (0.0313 in). The ports were counter-bored from the underside of the 9.53 mm (0.375 in) thick bump shell with a 1.59 mm (0.063 in) diameter, where the stainless steel tubulations were glued. Soft Tygon tubing with 1.59 mm (0.063 in) inner diameters were used as the pressure lines to the pressure transducer. A Scanivalve SSS-48C pneumatic scanner housing a PDCR23D differential pressure transducer with a SCSG2 signal conditioner was used to sequentially measure each channel. The transducer has a differential range of 2.5 psi with an accuracy of 0.06% FS. An adjustable voltage gain setting allowed the transducer output voltage to be set to match the input range of the data acquisition (DAQ) unit. The DAQ used in these experiments was a National Instruments USB 6343, a 16 bit A/D converter with a voltage input range of  $\pm 10$  V. The data were sampled at 100 Hz for 30 seconds to allow full convergence at each port.

The Scanivalve scanner housing has one reference and 48 cycling channels, therefore three runs were required to obtain pressure data at each reference Reynolds number on all of the ports (1. centerline ports, 2. offspan ports, and 3. lateral apex and geometric inflection point ports). If a static line was not attached to the transducer during a run, it was sealed using pop rivets. Each port was checked using a handheld pressure seal tester to ensure there was no leakage during the experimental runs. A 6.35 mm thick aluminum bump cover used to reduce cavity flow on the underside on the bump was modified to enable the egress of the tubing from the test section. The reference channel of the transducer was connected to the static port of the reference Pitot-static probe located at  $X = 0.29$  m. The tunnel was set to a specified reference

Reynolds number using Setra model 270 absolute pressure transducers with a range of 600-1100 hPa, and an accuracy of 0.05% FS.

Calibration of the differential pressure transducer was conducted using the Setra model 270 pressure transducers. The pressure tubing from the reference Pitot-static probe was split using "T" connections so that both transducer systems (Scanivalve differential system used for final  $C_p$  measurements and the absolute Setra transducers used to set the tunnel conditions) experienced the test section reference total and static freestream pressures. The tunnel fan speed was adjusted to vary the freestream conditions from no flow to a dynamic pressure of  $q_\infty \approx 4.0$  kPa, which is beyond the expected values of  $|\Delta P| = |P_i - P_\infty|$  for runs up to  $M = 0.2$ . A sample calibration fit is shown in Fig. 2.23. Negative values were acquired by swapping the static and total pressure tubing. Initial and final values for no flow ( $U_\infty = 0$ ) were both used in the calibration fit. Acquisition at each tunnel freestream speed consisted of taking 1000 samples per second for 10 seconds. After the transducer was calibrated, the data were sampled at 100 Hz for 30 seconds to allow full convergence at each port. The differential pressure transducer stepped through the various channels to acquire mean voltage data for each port. Channel 0 was connected to the total pressure line of the reference Pitot-static port. The acquisition software was set up so that channel 0 was acquired before and after the rest of the channels to determine a mean dynamic pressure ( $q_\infty = P_0 - P_\infty$ ) that would be used to normalize the differential pressures for the rest of the port locations (Equation 2.13).

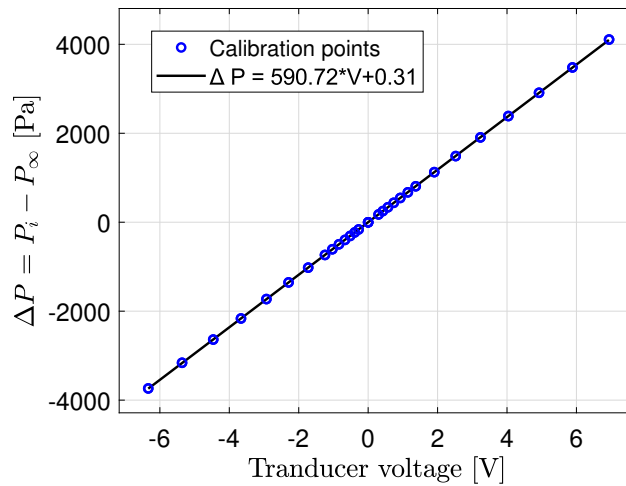


Figure 2.23. Linear calibration fit from Scanivalve differential pressure transducer voltage to Setra absolute pressure transducers, connected to the same pressure lines.

Tap locations are found in Appendix C. The uncertainty analysis for the  $C_p$  data is provided in Appendix D.5.

#### 2.4.7.2 Dynamic Pressure Sensor Instrumentation

Instantaneous pressure signals, such as those obtained using Kulite dynamic pressure sensors, can give insight into the dynamics of complex flow fields. In the case of separated flow, identification of the unstable modes which govern the physics of the separated shear layer is of particular interest. In the presented experiment, an array of Kulite sensors were mounted on the Boeing bump in the separated flow region. The sensors used were Kulite model XCS-093-5A miniature pressure transducers. These sensors were 2.41 mm in diameter, and 9.53 mm tall from the sensing head to the Teflon insulated wires. The nominal pressure range of the sensors were 34473.8 Pa absolute, and the pressure response for this sensor type is linear up to three times the nominal range. The sensors' diaphragms were protected using the Kulite B-type screen. The sensors had a dynamic response up to 150 kHz: the natural frequency of the sensor type used. Six sensors were oriented in a streamwise array near the centerline of the test section, at  $z/L = 0.0278$ , located in the streamwise positions of  $x/L = [0.076, 0.138, 0.201, 0.264, 0.326, 0.389]$ , as shown in Figure 2.24.

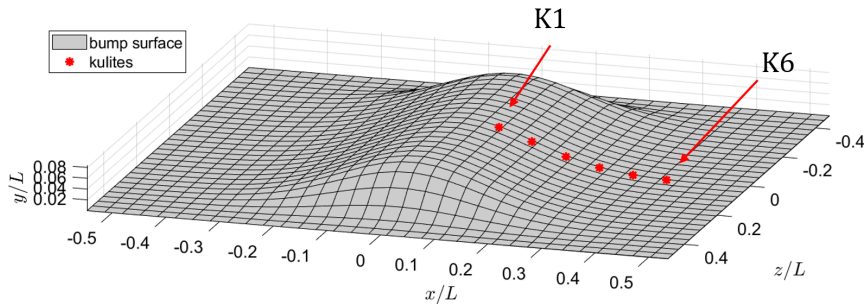


Figure 2.24. Kulite sensor locations on the downstream side of the bump section.

The sensors were labeled K1-K6 in streamwise order. They were mounted wall-normally using counter-bored holes cut the underside of the bump, with an outer diameter of 2.49 mm (to house the sensor) and a smaller 0.79 mm diameter that led up to the bump surface. The sensors were sealed using Dow Corning RTV 734 sealant. The seals were confirmed using a vacuum pump after a 24 hour cure. The wiring was soldered onto DB9 shielded plug connectors, which were pulled out of the

test section through a side window. They were then plugged into the input connectors of the Kulite KSC-2 signal conditioners. The signal conditioners provided the sensors with 10 V bipolar excitation and DC coupling. The return signal was pre-gained by 8, and post-gained by 16. The low pass cut-off filter was set to 127.5 kHz. A 12-bit Teledyne Lecroy HDO8108A 1 GHz high definition oscilloscope was used to record the six dynamic pressure signals simultaneously. The oscilloscope was set to 1 MΩ DC coupling, with a 200 MHz low pass filter cut-off frequency. Voltage data was sampled at 100 or 250 kHz for 50 seconds at each test condition.

Because the experimental pressures were outside of the nominal pressure range, a manual calibration was obtained after each test. This was done using a Heise differential reference transducer with a  $\pm 13789.5$  Pa (2 psi) pressure range. Prior to calibration of each sensor, the ambient lab pressure was recorded from the Setra model 270 transducers, and the sensors were auto-balanced to 0 V. A Mityvac vacuum pump was used to apply several different vacuum pressures to the sensors with a range that slightly exceeded the pressures the sensors were expected to see during the experiments, which were identified for each location using the static pressure tap data along the centerline of the bump. A Fluke 116 multimeter was used to measure the sensor voltage output at each calibration point, while the Heise transducer displayed the pressure difference from ambient conditions. The calibration curves, as shown in Figure 2.25, were used to obtain the pressure sensitivities for each of the sensors, both for time-averaged mean and fluctuation intensities. The sensors displayed a linear relationship between applied differential pressure and the output voltage within the calibrated pressure range. An example set of sensor sensitivities obtained from a calibration with the bump in the A configuration is shown in Table 2.4

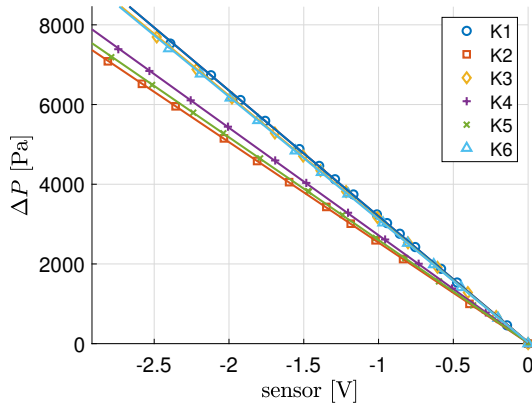


Figure 2.25. Kulite calibration data referenced to the ambient lab conditions at the time of calibration. The symbols represent the calibration points for each of the sensors, and the solid lines of matching colors denote the linear calibration fits used for converting voltages to pressures.

TABLE 2.4

SAMPLE KULITE SENSOR PRESSURE SENSITIVITY OBTAINED  
VIA CALIBRATION.

sensor #	$x/L$	sensitivity [Pa/mV]
K1	0.076	3.2
K2	0.138	2.5
K3	0.201	3.1
K4	0.264	2.7
K5	0.326	2.6
K6	0.389	3.1

## CHAPTER 3

### BOUNDARY CONDITIONS AND FLOW QUALITY

#### 3.1 Empty Tunnel Flow Characterization

##### 3.1.1 Freestream Pitot-Static Rakes

A traversing Pitot-static probe was used to investigate the uniformity of the empty test section prior to installation of the testing model or fixtures. The unoccupied test section was investigated using a  $6 \times 6$  grid of measurement points at five streamwise plane positions of  $X = 0, 0.49, 1.02, 1.37$ , and  $1.73$  m. A cross-sectional view of the grid locations is shown in Figure 3.1. The measurements were taken using grid points vertically at  $Y = 0.25, 0.28, 0.37, 0.50, 0.59$ , and  $0.80$  m, and at the spanwise locations of  $Z = \pm 0.05, \pm 0.14$ , and  $\pm 0.23$  m.

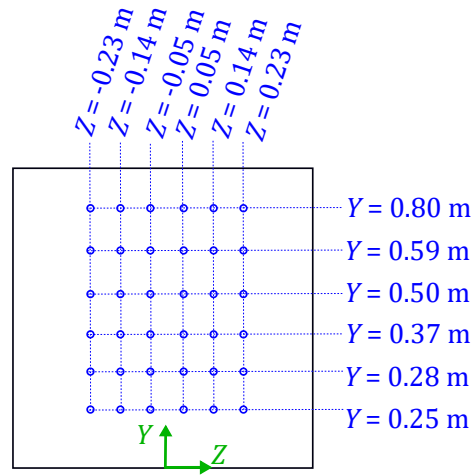


Figure 3.1. Empty tunnel Pitot-static probe freestream uniformity grid locations.

Measurements were taken using a straightened Pitot-static probe with a 1.3 mm inlet diameter. A photograph of the probe mounting is shown in Figure 3.2. The

probe was affixed to a 3-axis traversing system that was mounted into the test section using machinable aluminum window blanks. Streamwise and spanwise traversing was controlled with three PBC Linear actuators using stepper motors with a stepping resolution of 0.05 mm. The spanwise actuator was held in an airfoil shaped housing that spanned between the tunnel side walls and was connected to the two streamwise actuators. The vertical axis was traversed by a Faulhaber Series Am1524 micro stepping motor. The probe was extended away from the traverse using a 3D printed airfoil shaped holder connected to several connecting bracket plates.

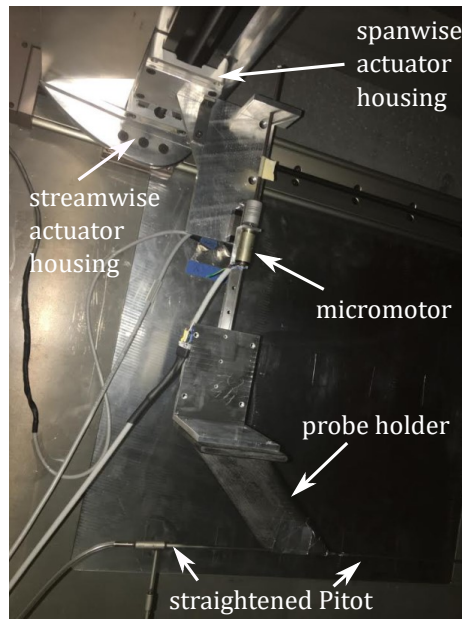


Figure 3.2. Labeled photograph of the empty tunnel traversing Pitot-static probe freestream uniformity setup. Flow is from right to left.

Freestream velocity data were sampled at each location at 1 kHz for 60 seconds, using the calibration procedure outlined in Section 2.4.2 and equations 2.2-2.6. The straightened Pitot probe was connected to the Scanivalve transducer system. The freestream data were sampled digitally using a National Instruments USB 6343 data acquisition unit (DAQ). Reference conditions were set using a reference probe with an inlet diameter of 1.5 mm located at  $(X, Y, Z) = (0.24, 0.83, 037)\text{m}$ , connected to the wind tunnel Setra Model 270 absolute pressure transducers. The 3-axis traverse could be configured so that the five streamwise grids of 36 data locations could be

measured. The most efficient way to acquire the data was to complete 6 spanwise strips of 6 locations per plane. The tunnel controller first set free-stream Mach number to exactly 0.200 (control panel resolution to three digits), and once the pressure stabilized the DAQ would begin sampling differential pressure voltages from the Scanivalve. The tunnel speed was untouched for the remainder of the testing period. After the first location was sampled for 60 seconds the traverse would move the probe to the next spanwise location, always starting at the negative most  $Z$  position and traversing in the  $+Z$  direction. Once each of the 6 locations were sampled, the tunnel fan would be shut off, bringing the tunnel velocity to zero. Then the traverse would be moved either vertically or streamwise, depending on the current configuration of the window blanks. It should be noted that for the testing period for each of the spanwise strips, the tunnel fan speed was unchanged. Figure 3.3 shows the velocity data obtained at each grid location.

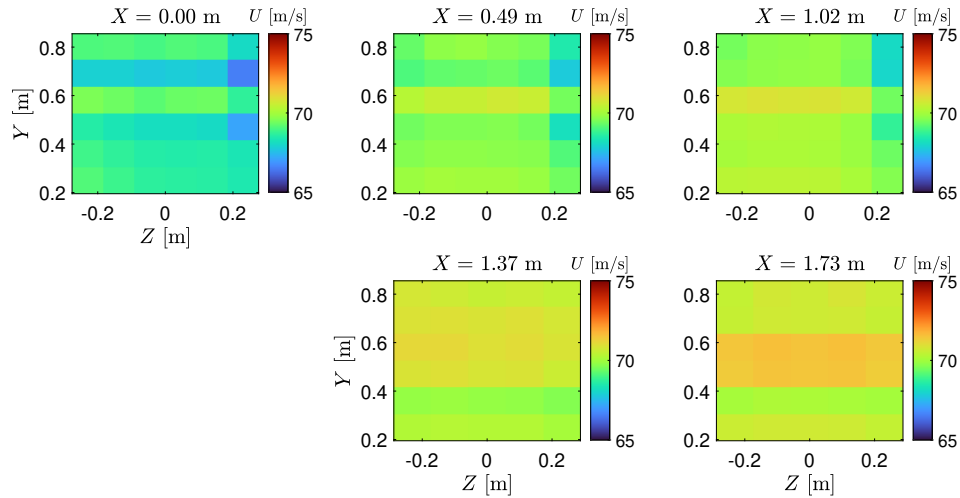


Figure 3.3. Freestream velocity acquired across the empty test section at a single reference velocity of  $U_\infty = 69$  m/s (corresponding to  $M = 0.2$  and  $Re_L = 4.0 \times 10^6$ ).

A minor acceleration (3.3% increase from  $X = 0.00$  to  $1.73$  m) is caused by the flow area reduction resulting from the streamwise growth of the displacement thickness of the sidewall boundary layers. The uniformity of the mean velocity was within  $\sigma_{U_{grid}}/U_{grid} < 0.92\%$ , where  $\sigma_{U_{grid}}$  and  $U_{grid}$  are the standard deviation and

the mean of the 36 velocity measurements at each streamwise plane, respectively. The uncertainty of the measurements is calculated in Appendix D.6, and is  $\varepsilon_U/U < 0.7\%$  across the 5 measurement planes (95% confidence).

### 3.1.2 Freestream X-Wire Rakes

A traversing x-wire probe was used to investigate the freestream angularity and turbulence intensities within the empty test section prior to installation of the testing model or fixtures. The unoccupied test section was sampled using a  $4 \times 4$  grid of measurement points at four streamwise plane positions of  $X = 0.49, 1.02, 1.37$ , and  $1.73$  m. A cross-sectional view of the grid locations is shown in Figure 3.4. The measurements were taken using grid points vertically at  $Y = 0.28, 0.37, 0.50$ , and  $0.59$  m, and at the spanwise locations of  $Z = \pm 0.05$  and  $\pm 0.14$  m.

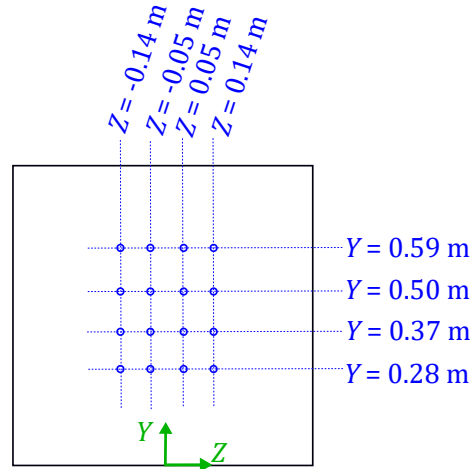


Figure 3.4. Empty tunnel x-wire probe freestream angularity grid locations.

Measurements were taken using an Auspex X-wire probe. The x-wire consists of two  $5\ \mu\text{m}$  thick 1 mm long Tungsten hot-wires configured perpendicular to each other. For the duration of the test entry, the two wires were placed in the tunnel so that they were both  $45^\circ$  to the streamwise axis. The instantaneous velocity field is described using the equation

$$u_{total} = u\hat{i} + v\hat{j} + w\hat{k}, \quad (3.1)$$

where  $\hat{i}$ ,  $\hat{j}$ , and  $\hat{k}$  are unit vectors oriented in the streamwise, vertical, and spanwise

directions, respectively. The total velocity field can then be described by the following equation:

$$u_{total} = (U + u')\hat{i} + (V + v')\hat{j} + (W + w')\hat{k}, \quad (3.2)$$

where the velocity fluctuations of the aforementioned components are denoted using an apostrophe, and the means are capitalized.

The x-wire probe used two wires connected to the CTA hot-wire system described in 2.4.3. Each of the wires sense the velocity normal to the wire axis. Hence, two components of velocity can be determined in a single experimental run. In order to find the third component, the x-wire probe was rotated about the streamwise axis by 90°. Figure 3.5a shows a diagram of how three components of velocity were resolved in two separate orientations. Figure 3.5b shows a diagram of a typical flow that is at a slight angle to the streamwise axis. A resultant angle to a wire,  $\theta_w$ , was defined for the relationship between the flow angle and the wire axes. Considering the assumption that the wires were both placed so they were 45° with respect to the streamwise axis, the relationship between the normal components of the velocity sensed by wires A and B ( $U_A$  and  $U_B$ , respectively, as shown in Figure 3.5b) have the following geometric relations:

$$U_A = U_{total} \sin(90^\circ - \theta_w) = U_{total} \cos \theta_w, \text{ and} \quad (3.3)$$

$$U_B = U_{total} \sin(\theta_w). \quad (3.4)$$

Here, the parameter  $U_{total}$  is the velocity contribution sensed by the combination of wires A and B, with the angle  $45^\circ - \theta$  representing the instantaneous flow angularity. The components of  $U_{total}$  are of interest and were computed by

$$U = U_{total} \cos(45^\circ - \theta_w) = U_{total} (\cos 45^\circ \cos \theta_w + \sin 45^\circ \sin \theta_w), \text{ and} \quad (3.5)$$

$$V = U_{total} \sin(45^\circ - \theta_w) = U_{total} (\sin 45^\circ \cos \theta_w + \cos 45^\circ \sin \theta_w). \quad (3.6)$$

The components can then be expressed as a function of the sensed velocities  $U_A$  and  $U_B$  by

$$U = \frac{\sqrt{2}}{2}(U_A + U_B), \text{ and} \quad (3.7)$$

$$V = \frac{\sqrt{2}}{2}(U_A - U_B). \quad (3.8)$$

The same procedure was done to obtain the  $U$  and  $W$  components when the probe was rotated 90° around the streamwise axis.

Figure 3.6a shows the x-wire testing setup during calibration. Calibration of the x-wire probe was done using a Pitot-static probe placed in the same streamwise plane. The location of the x-wire probe during calibration was  $(X, Y, Z) = (1.02, 0, 0.61)$  m. The straightened Pitot probe used to obtain velocity for calibration was located at  $(X, Y, Z) = (1.02, -0.06, 0.057)$  m.

The calibration of the individual hot-wires followed the same procedure outlined in Section 2.4.3. The angle of both of the wires were assumed to be at a 45° angle to

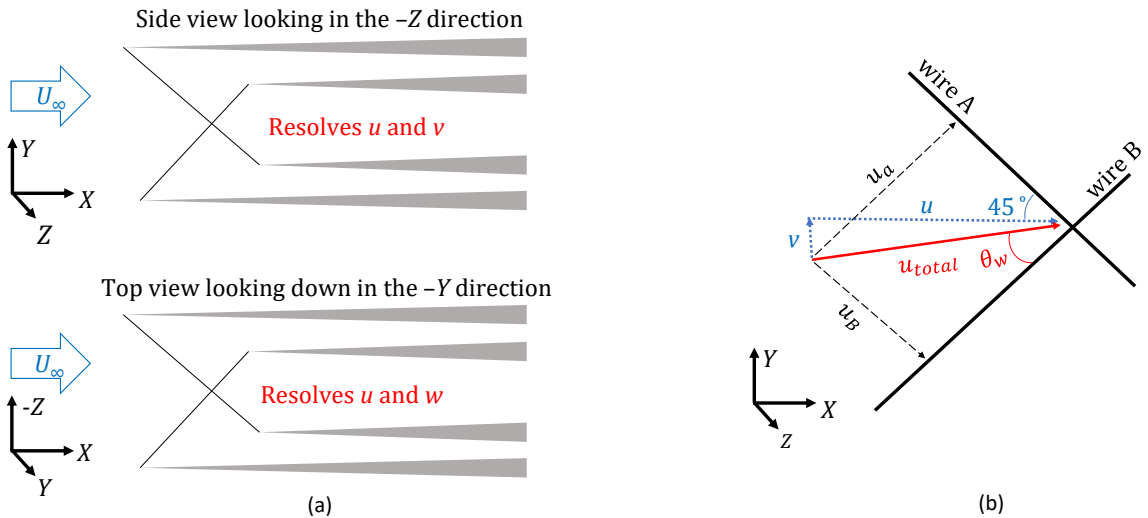


Figure 3.5. (a) Diagram of the x-wire orientations and (b) geometric relationships used to evaluate instantaneous flow angularity and velocity components.

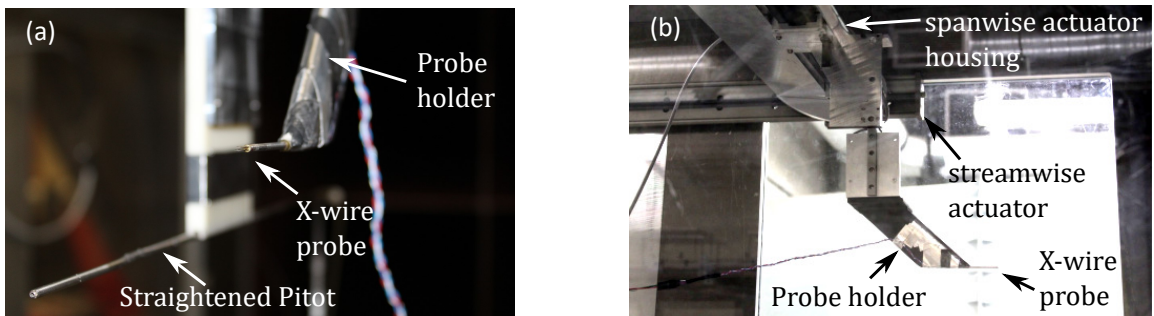


Figure 3.6. (a) Setup of the x-wire and straight Pitot probe used to calibrate the x-wire anemometer channels against the velocity obtained by the Pitot probe, and (b) the setup of the x-wire for data acquisition on selected measurement grids.

the velocity sensed by the Pitot probe,  $U_{Pitot}$ . Thus, the flow velocity measured by

either wire was

$$U_{norm} = \frac{\sqrt{2}}{2} U_{Pitot}. \quad (3.9)$$

Figure 3.7 shows a sample 5th order calibration fit between the two hot-wires and the sensed normal velocity. Using the sum of squares, the total instantaneous velocity can be obtained by the following relationship between the instantaneous velocity components sensed by each of the wires:

$$u_{total} = \sqrt{u_A + u_B} \quad (3.10)$$

The flow angle can be determined using simple geometric relations

$$\theta = 45 - \arccos(u_A/u_{total}) = 45 - \arcsin(u_B/u_{total}) \quad (3.11)$$

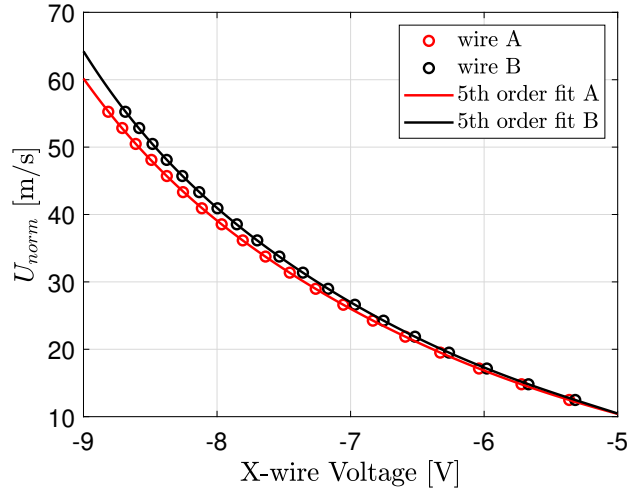


Figure 3.7. Sample 5th order calibration fit of two hot-wire channels used during the x-wire test entry.  $U_{norm}$  is the velocity perpendicular to each wire given by Equation 3.9.

Depending on the orientation of the probe in tunnel, the instantaneous  $\theta$  represented either the angle between  $u$  and  $v$  or  $u$  and  $w$ . The angle can be used to determine the magnitude of fluctuations in each direction. An example of this would be when the probe is oriented to detect  $u$  and  $v$ . Here time series data would be

found with the simple calculations  $u = u_{total} \cos \theta$  and  $v = u_{total} \sin \theta$ .

Turbulence root-mean-squared (RMS) values ( $\sqrt{u_i^2}$ ) were normalized by the reference freestream velocity to gather turbulence intensities as a percentage of each of the three velocity components.

Figure 3.6b shows the setup during the measurement of the freestream velocity data. The x-wire probe was affixed onto a 3-axis traversing system that was mounted into the test section using machinable window blanks. The streamwise and spanwise traversing was controlled using PBC Linear actuators that contained stepper motors with a stepping resolution of 0.05 mm. The spanwise actuator was held in an airfoil shaped housing that spanned between the tunnel side walls and connected to the two streamwise actuators. The vertical axis was traversed by a Faulhaber Series Am1524 micro stepping motor. The probe was extended away from the traverse using a 3D printed airfoil shaped holder. The 3-axis traverse was configured so that the four streamwise grids of 16 data locations could be measured. The most efficient way to acquire the data was to complete 4 spanwise strips of 4 locations per plane. The tunnel controller first set the freestream condition (control panel resolution was three digits for  $M_\infty$ ). Once the pressure stabilized the DAQ began sampling bridge voltages from the x-wires. The tunnel speed was untouched for the remainder of the testing period. Data was acquired at 20 kHz for 30 seconds at each grid location. After the first location was sampled for 60 seconds the traverse would move the probe to the next spanwise location, always starting at the negative most  $Z$  position and traversing in the  $+Z$  direction. Once each of the 4 locations were sampled, the tunnel fan would be shut off, bringing the tunnel velocity to zero. Then the traverse would be moved either vertically or streamwise, depending on the current configuration of the window blanks. This process was done twice to obtain data for  $u$  and  $v$ , and subsequently  $u$  and  $w$ . Only the  $u$  from the first set was used. After acquisition, the calibration fit was applied to the anemometer voltages and analysis described above was applied. An 8th order Butterworth band-pass filter was applied to the time-series data to remove spectral energy content below 100 Hz and above 4.5 kHz for the RMS quantities.

Figures 3.8-3.11 shows the  $4 \times 4$  grids of measured three-component mean velocity and turbulence RMS data at each of the streamwise planes for a reference freestream velocity of  $U_\infty = 69$  m/s ( $M = 0.2$  and  $Re_L = 4.0 \times 10^6$ ). Figure 3.12 shows the three-component mean velocity and turbulence RMS data for a repeat acquisition at  $X = 1.37$  m at a reference velocity of  $U_\infty = 69$  m/s ( $M = 0.2$  and  $Re_L = 4.0 \times 10^6$ ). Figure 3.13 shows the three-component mean velocity and turbulence RMS data at  $X = 1.37$  for a reference freestream velocity of  $U_\infty = 34$  m/s ( $M = 0.1$  and  $Re_L = 2.0 \times 10^6$ ). The flow angles were averaged across the four measurement planes. For the  $M = 0.2$  case, the average flow angles were found to be  $\theta_y = \tan^{-1}(V/U) = 2.2^\circ$  and  $\theta_z = \tan^{-1}(W/U) = 1.5^\circ$ . For the  $M = 0.1$  grid taken at a single plane, the average flow angles were found to be slightly lower at  $\theta_y = 1.9^\circ$  and  $\theta_z = 1.1^\circ$ . The angularity was determined to be negligible, as the uncertainty in probe alignment was  $3^\circ$  in either direction. The average turbulence intensity for the  $M = 0.2$  case was  $\sqrt{u'^2}/U_\infty = 0.06\%$  across the four planes. For the  $M = 0.1$  measurement grid it was

$$\sqrt{\bar{u^2}}/U_\infty = 0.02\%.$$

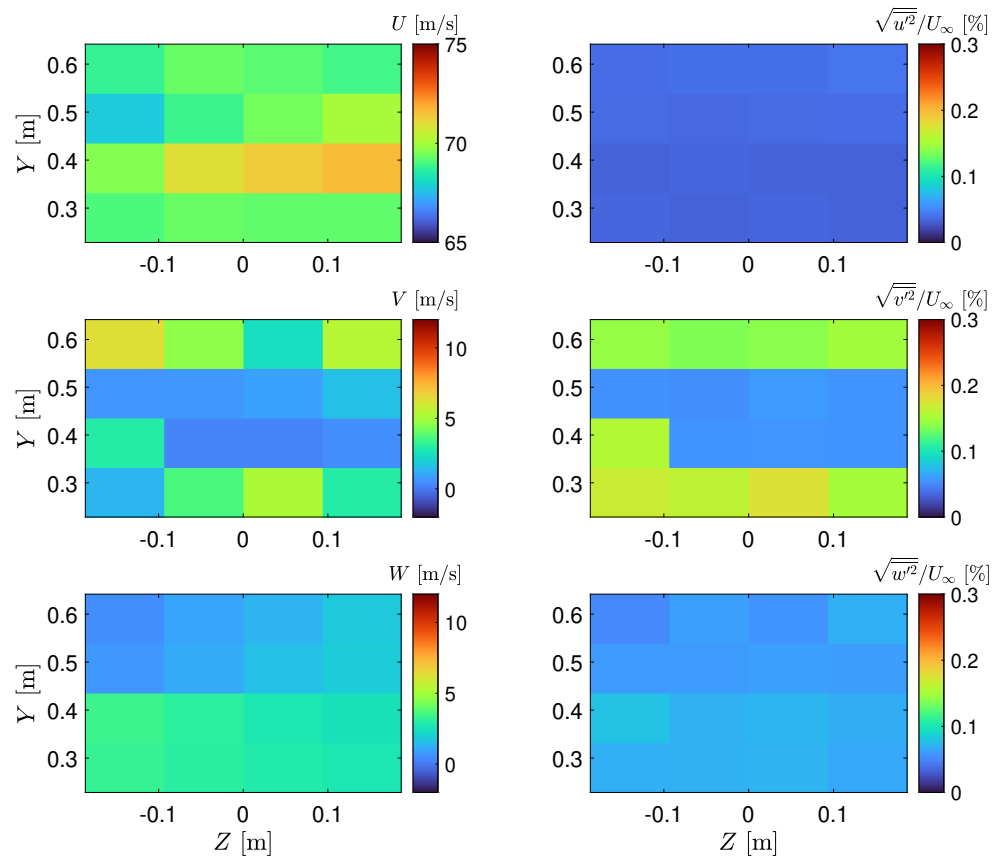


Figure 3.8. Three-component mean velocity and turbulence RMS measured on a  $4 \times 4$  grid by a traversing x-wire at  $X = 0.49$  m for a freestream reference velocity of  $U_\infty = 69$  m/s, corresponding to freestream Mach and Reynolds numbers based on tunnel width of  $M = 0.2$  and  $Re_L = 4.0 \times 10^6$ , respectively.

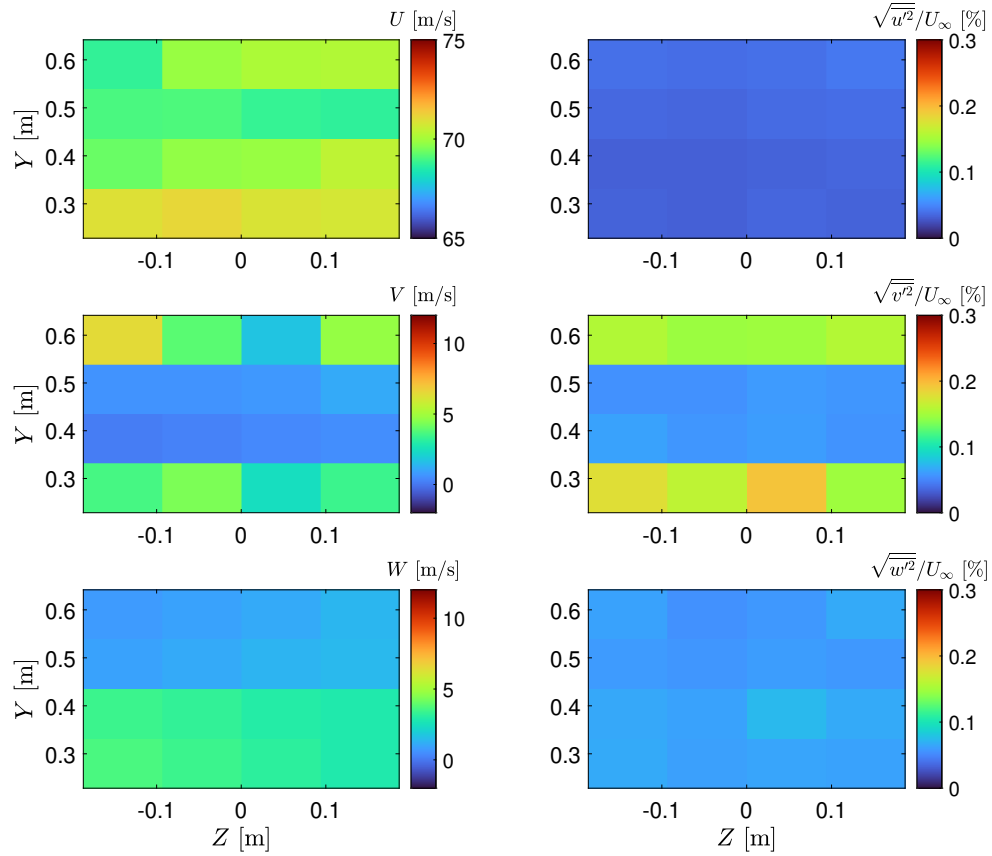


Figure 3.9. Three-component mean velocity and turbulence RMS measured on a  $4 \times 4$  grid by a traversing x-wire at  $X = 1.02$  m for a freestream reference velocity of  $U_\infty = 69$  m/s, corresponding to freestream Mach and Reynolds numbers based on tunnel width of  $M = 0.2$  and  $Re_L = 4.0 \times 10^6$ , respectively.

### 3.1.3 Total Pressure Probe Boundary Layer Investigation

A traversing total pressure boundary layer style probe was used to investigate the boundary layer development on each of the four test section walls prior to the installation of the testing model or fixtures. Measurements for the boundary layer surveys were taken using a United Sensor BA-025-12-C-11-.650 boundary layer total pressure probe. The probe has an inlet diameter of 0.32 mm (0.0125 in), which is half the tube diameter of 0.64 mm (0.025 inches). Local dynamic pressure was obtained by measuring the difference between the total pressure at the boundary layer probe and the static pressure from a straightened Pitot-static probe. Velocity was computed using Equations 2.2-2.4, where the  $\Delta P$  value was the local dynamic pressure. The pres-

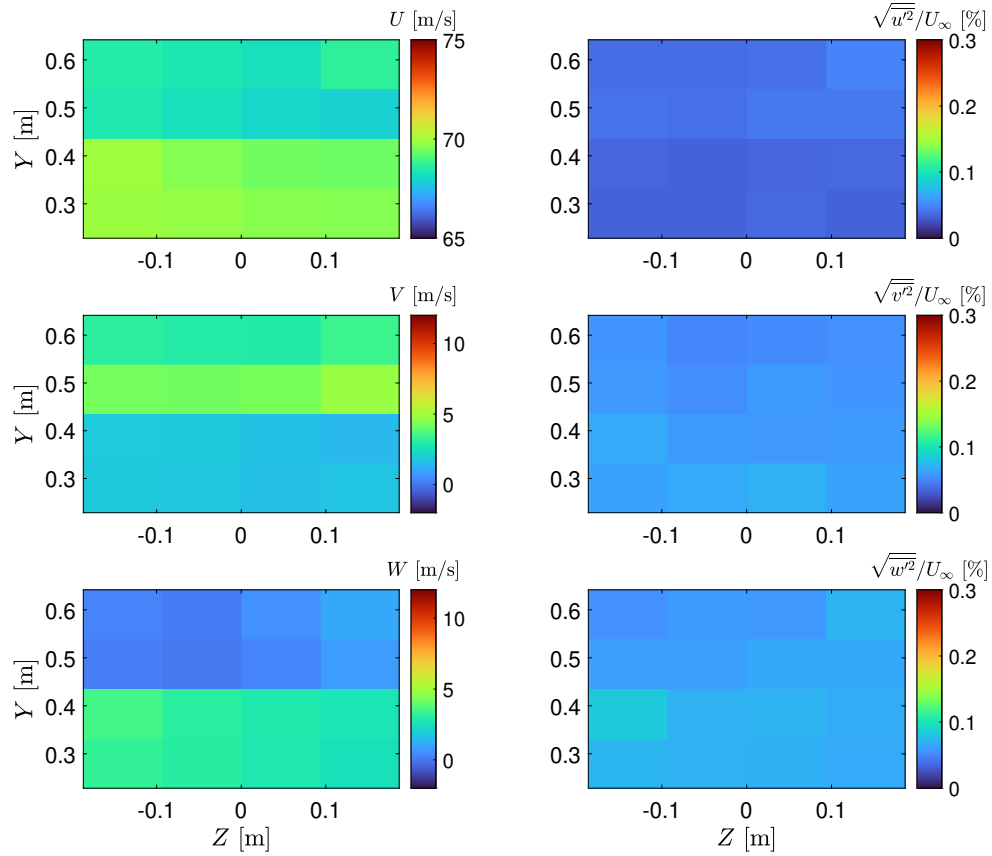


Figure 3.10. Three-component mean velocity and turbulence RMS measured on a  $4 \times 4$  grid by a traversing x-wire at  $X = 1.37$  m for a freestream reference velocity of  $U_\infty = 69$  m/s, corresponding to freestream Mach and Reynolds numbers based on tunnel width of  $M = 0.2$  and  $Re_L = 4.0 \times 10^6$ , respectively.

sure lines were connected to a linearly calibrated Scanivalve transducer system (see Section 2.4.2 for details) via Tygon tubing fed out from the back of the test section. Four streamwise planes were tested at the same locations investigated in Sections 3.1.1 and 3.1.2, i.e.,  $X = 0.49, 1.02, 1.37$ , and  $1.73$  m. At each streamwise locations, 12 boundary layers were measured using the total pressure probe. Figure 3.14 shows the locations and naming convention of the boundary layer survey locations. The local coordinate,  $y_w$ , denotes the wall-normal distance of the measurement from the wall where the profile originated. Three profiles were measured on each wall. For the top and bottom walls, the  $y_w = 0$  locations were found at  $Z = \pm 0.23$ , and  $0.00$  m. For the sidewalls, the profiles began at  $Y = 0.23, 0.57$ , and  $0.69$  m.

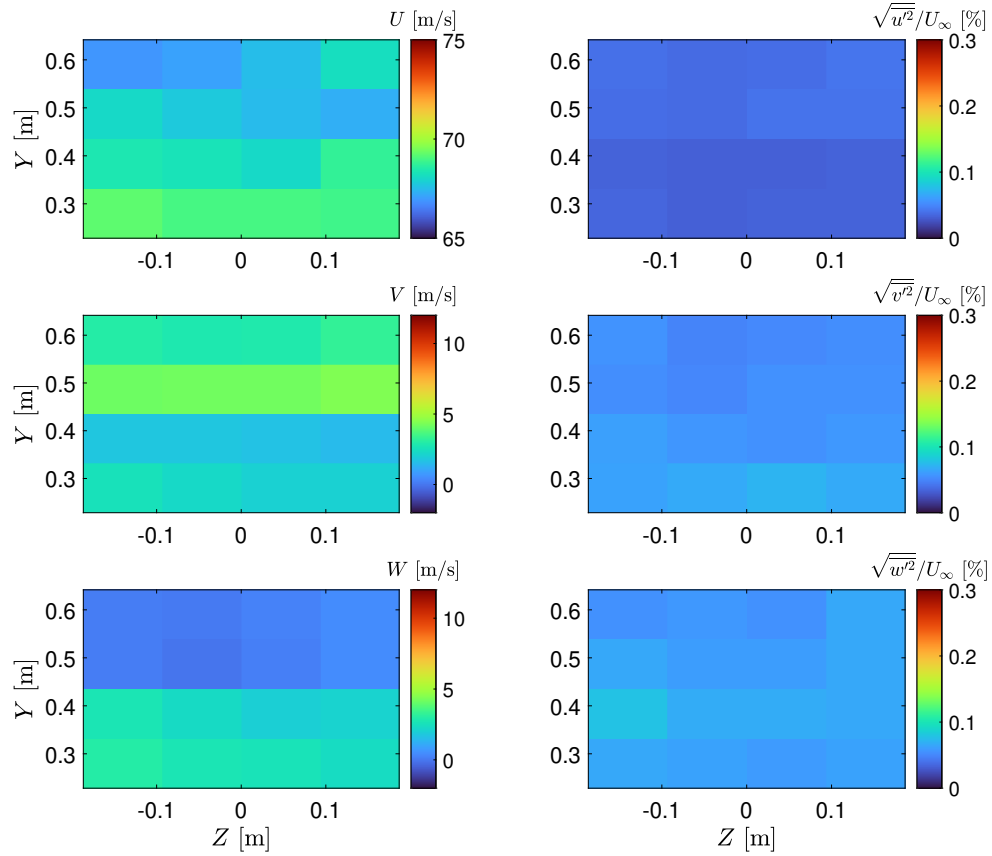


Figure 3.11. Three-component mean velocity and turbulence RMS measured on a  $4 \times 4$  grid by a traversing x-wire at  $X = 1.73$  m for a freestream reference velocity of  $U_\infty = 69$  m/s, corresponding to freestream Mach and Reynolds numbers based on tunnel width of  $M = 0.2$  and  $Re_L = 4.0 \times 10^6$ , respectively.

Figure 3.15 shows the probe and traverse system setup used to acquire velocity profiles on each of the empty tunnel walls. The total pressure probe head and Pitot probe were aligned in the same streamwise plane during measurements. The two probes were placed in the tunnel by 3D printed holders that were attached to a 3-axis traversing system. Movement was controlled using PBC linear actuators with stepper motors with stepping resolution of 0.05 mm. An airfoil shaped housing that spanned between the tunnel side walls was connected to two streamwise actuators fixed to aluminum window blanks. The wall-normal axis of the traversing system was traversed by a Faulhaber Series Am1524 micro stepping motor controlled using an Arduino Uno micro-controller. A reference Pitot-static probe located at  $(X, Y, Z) =$

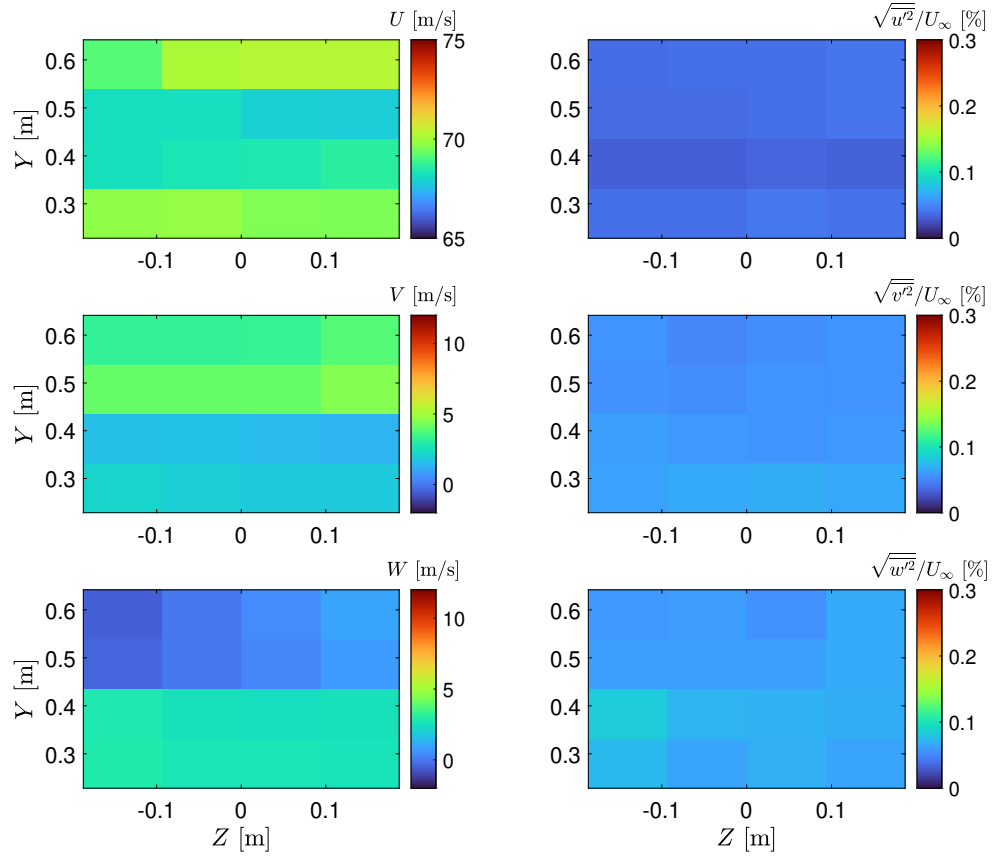


Figure 3.12. Three-component mean velocity and turbulence RMS measured on a  $4 \times 4$  grid by a traversing x-wire at  $X = 1.37$  m (repeat measurement) for a freestream reference velocity of  $U_\infty = 69$  m/s, corresponding to freestream Mach and Reynolds numbers based on tunnel width of  $M = 0.2$  and  $Re_L = 4.0 \times 10^6$ , respectively.

(0.24, 0.83, 0.37) m was connected to the tunnel Setra model 270 absolute pressure transducers to set the tunnel speed to the reference velocity.

Before each boundary layer survey, the boundary layer probe was traversed to the desired location in the test section with an estimated accuracy of 1 mm in each direction. Once the probe was placed, the tunnel controller would set freestream Mach number (control panel resolution is three digits). After the pressure stabilized, the micrometer would be pulsed down to the wall using an Arduino Uno and an L298N dual H bridge motor driver. Each pulse stepped 0.05 mm (1/512 in) towards the wall until the boundary layer probe made contact with the wall ( $y_w = 0$ ). The position where the probe was closest to the wall was determined by selecting the minimum

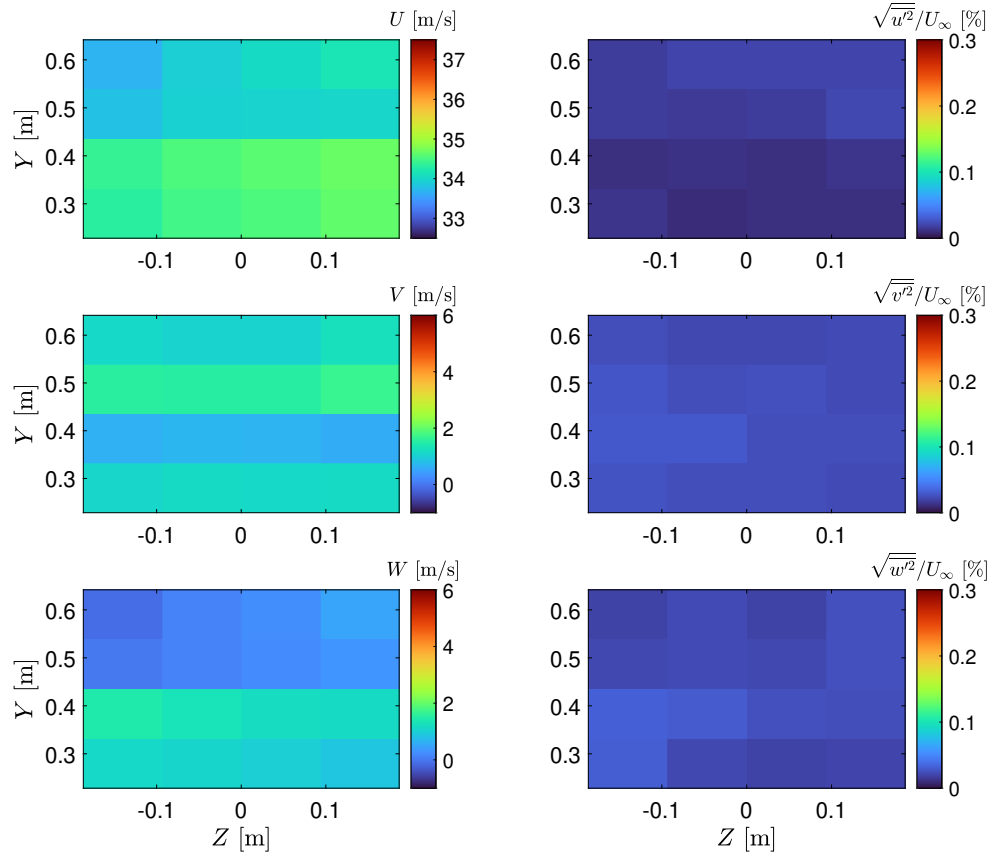


Figure 3.13. Three-component mean velocity and turbulence RMS data measured on a  $4 \times 4$  grid by a traversing x-wire at  $X = 1.37$  m for a freestream reference velocity of  $U_\infty = 34$  m/s, corresponding to freestream Mach and Reynolds numbers based on tunnel width of  $M = 0.1$  and  $Re_L = 2.0 \times 10^6$ , respectively.

velocity at each wall-normal position. The low thickness and high flexibility of the probe resulted in a lifting motion when it was stepped too far into the wall. As a result, the probe head would lift into a higher velocity region in the boundary layer, as shown in Figure 3.16. Once the measured velocity increased after a step towards the wall, a single step back away from the wall would return the mean velocity to its minimum value,  $U_{\min}$ , found closest to the wall. Using this procedure, the first wall-normal location was determined to be half a probe diameter (0.32 mm) from the wall. With a friction velocity of  $u_\tau \approx 2.5$  m/s, determined later using the Clauser method, this corresponded to a  $y^+ \approx 50$ . This process was done prior to acquiring velocity data at each of the profile locations.

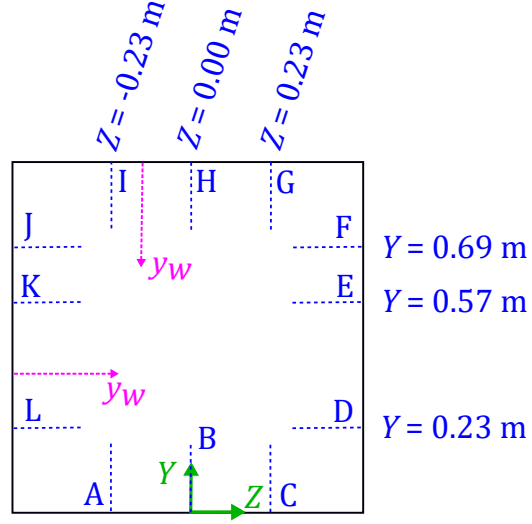


Figure 3.14. Empty tunnel boundary layer measurement locations and naming convention.

Velocity data was sampled at 1 kHz for 30 seconds at each wall-normal position in each of the boundary layer surveys. A 16 bit National Instruments USB 6343 DAQ set to a  $\pm 5$  V range was used to convert the analog transducer data to discrete points. Each profile consisted of 37 measurements of the streamwise velocity  $U$ , with step size between points increasing towards the freestream velocity. Figure 3.17 shows the 12 profiles plotted together for each of the  $X$  planes for a reference velocity of  $U_\infty = 69$  m/s ( $M = 0.2$ ,  $Re_L = 4.0 \times 10^6$ ). Figure 3.18 shows the plots of select boundary layer profiles (B, F, J, and H) measured at  $X = 0.49$  and  $1.02$  m for a reference velocity of  $U_\infty = 34$  m/s ( $M = 0.1$ ,  $Re_L = 2.0 \times 10^6$ ). Figure 3.19 shows the plots of select boundary layer profiles (B, F, J, and H) measured at  $X = 0.49$  and  $1.02$  m for a reference velocity of  $U_\infty = 17$  m/s ( $M = 0.05$ ,  $Re_L = 1.0 \times 10^6$ ). Measurement uncertainties with a 95% confidence interval are plotted using bars at each measurement point. The detailed uncertainty analysis conducted for these measurements can be found in Appendix D.7. It can be seen that the boundary layer grows with streamwise distance, and is uniform across each of the tunnel side walls within the measurement uncertainty.

### 3.2 Splitter Plate Only (No Bump)

#### 3.2.1 Leading Edge and Side Wall Streamlines

After the test entry investigating flow quality within the empty test section, the splitter plate and associated fixtures were inserted into the test section. Prior to installing the bump section, the entire test bed consisted of flat plate sections to create a canonical flat plate testing article. The purpose of this test entry was to set

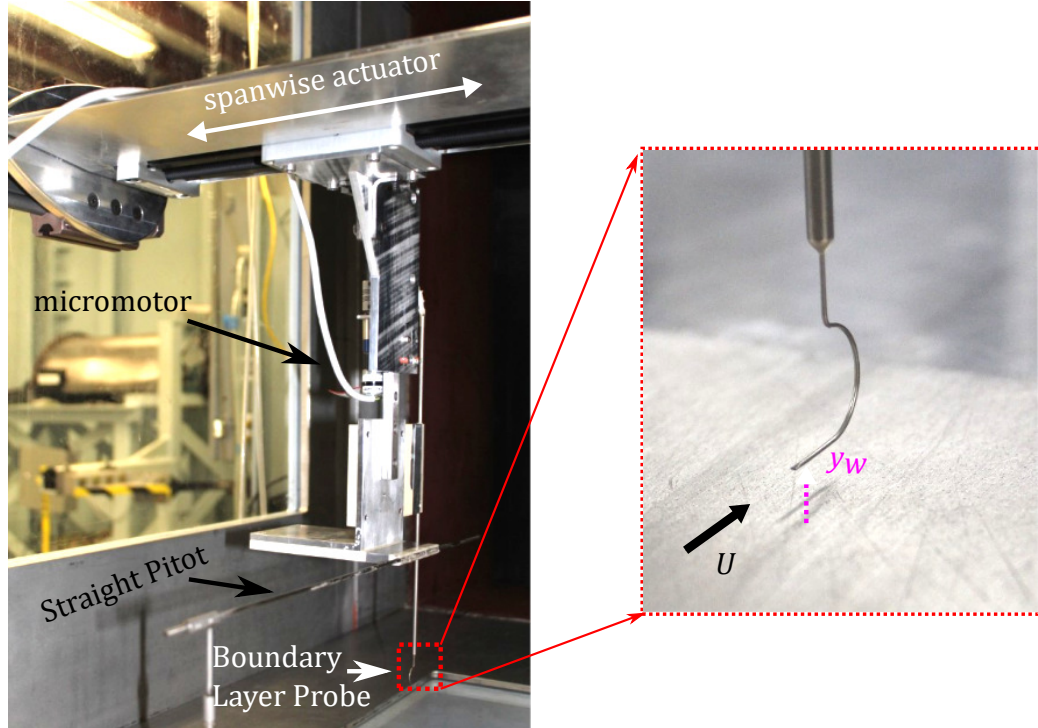


Figure 3.15. Photograph of the traversing mechanism used to place a total pressure probe near the empty test section walls for boundary layer measurements.

the trailing edge flap angle to that no separation was present at the leading edge, and that the stagnation point of the flow occurred upstream of the tripping dots. Flow visualization (see Section 2.4.1) was used to investigate the presence of any corner flow phenomenon, and that the splitter plate did not have leakage from the top edge to the lower half of the test section. Figure 3.20a shows the leading edge skin friction lines. The stagnation point is upstream of the boundary layer tripping dots, so the flap angle of  $2^\circ$  was deemed appropriate. The streamlines were also shown to be parallel to the streamwise axis. Figure 3.20b shows a flow visualization of the corner junction of two of the plate sections with the  $+Z$  side wall at  $X = 1.8$  m. The transition from one plate was deemed hydrodynamically smooth, and there was no detected leakage or circulating fluid near the corner junction.

### 3.2.2 Boundary Layer Development

The boundary layer growth on the splitter plate and side walls was measured using the traversing hot-wire anemometry system described in Section 2.4.3. The four streamwise positions investigated were  $X = 0.49, 1.02, 1.37$ , and  $1.73$  m. Figure 3.21 shows a cross-sectional view of where the boundary layer profiles were obtained

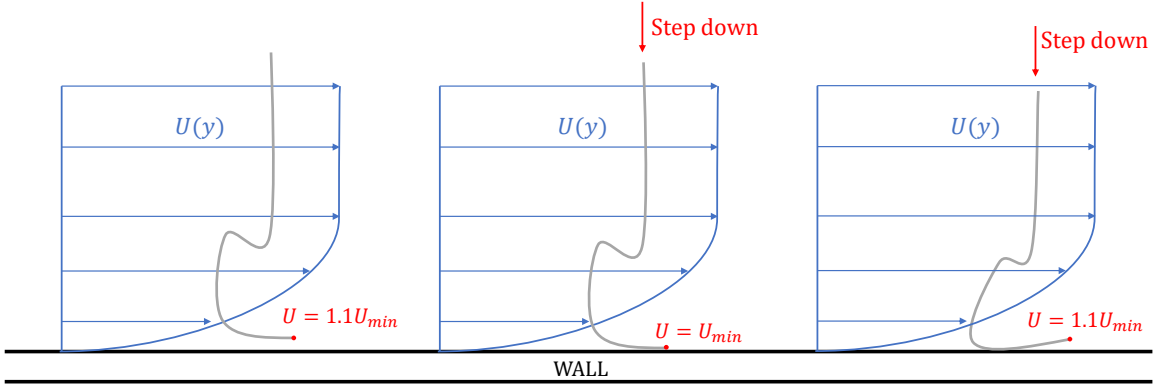


Figure 3.16. Diagram of the total pressure probe in an empty tunnel side wall boundary layer. When the probe was stepped towards the wall, the mean velocity sensed would decrease until a minimum velocity (and minimum  $y_w$ ) was reached. When a step down resulted in a velocity increase, the probe had gone too far, and required a single step away from the wall.

in the test section. Profiles A, B, and C in the flat plate case are at the same spanwise locations as the related measurements in the empty tunnel case (see Section 3.1.3) at  $Z = -0.23$ , 0.00, and 0.23 m, respectively, but they originate on the plate surface at  $Y = 0.46$  m. The side wall locations investigated were F, J, and K and had locations identical to those in Section 3.1.3 with the same notation. The perpendicular distance from the wall for each of the profiles is denoted as  $y_w$ .

The streamwise velocity boundary layer profiles were measured at  $U_\infty = 34$  m/s ( $M = 0.1$ ,  $Re_L = 2.0 \times 10^6$ ) and  $U_\infty = 69$  m/s ( $M = 0.2$ ,  $Re_L = 4.0 \times 10^6$ ), and are shown in Figures 3.22 and 3.23, respectively. Some repeat measurements were taken for redundancy and confirmation of test repeatability which are also plotted. Measurement uncertainties with a 95% confidence interval are plotted using bars at each measurement point. The detailed uncertainty analysis conducted for these measurements can be found in Appendix D.2. It can be seen that the boundary layer grows with streamwise distance. The uniformity of the profiles on the plate surface (A-C) is within the measurement uncertainty.

The boundary layer is thicker on the sidewalls (profiles F, J, and K), since they have more time to develop after the contraction of the wind tunnel. Figure 3.24 shows the average boundary layer thickness ( $y_w = \delta$  where  $U(y_w) = 0.99U_e$ ) for each of the streamwise measurement planes. The average boundary layer thickness on the flat surface (profiles A, B, and C) is shown next to the averaged boundary layer thickness measured on the side walls (profiles F, J, and K). The boundary layer thicknesses from the empty tunnel measurements were also averaged across the streamwise planes

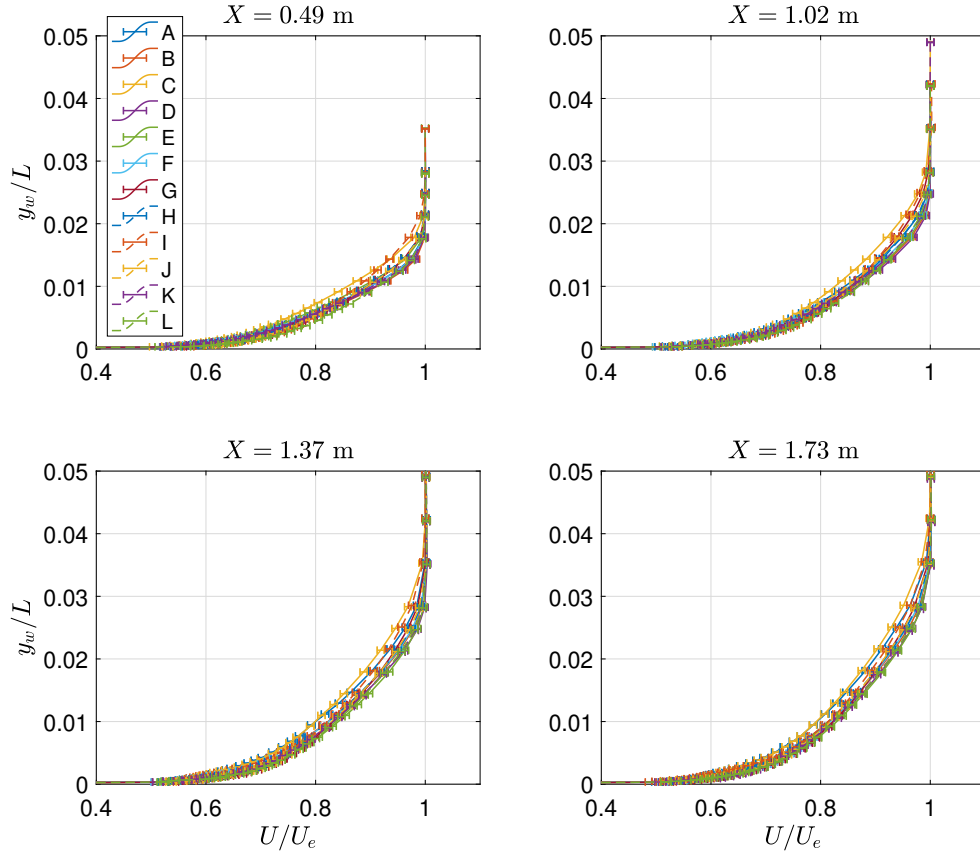


Figure 3.17. Boundary layer profiles obtained on each of the four empty test section side walls at a reference freestream velocity of  $U_\infty = 69 \text{ m/s}$ , corresponding to freestream Mach and Reynolds numbers based on tunnel width of  $M = 0.2$  and  $Re_L = 4.0 \times 10^6$ , respectively. Uncertainty bars indicate a 95% measurement confidence interval.

(all profiles A through L). Canonical ZPG TBL growth for a flat plate is given by the empirical curve  $\delta(X) = 0.37/Re_X^{1/5}$  [2], and is plotted in Figure 3.24 along with the experimental data beginning at  $X = 0.051 \text{ m}$ , i.e., the location of the boundary layer trip dots. The empty tunnel boundary layer had the same thickness as the side wall measurements when the flat plate was installed, and they are both larger than the expected flat plate TBL growth because they have a origin upstream of the splitter plate leading edge. This is in contrast to the TBL measurements on the flat plate surface, that show a slightly slower growth than expected. This is due to a minor acceleration of the flow (FPG flow) induced by the reducing flow area with the streamwise growth of the boundary layer displacement thickness.

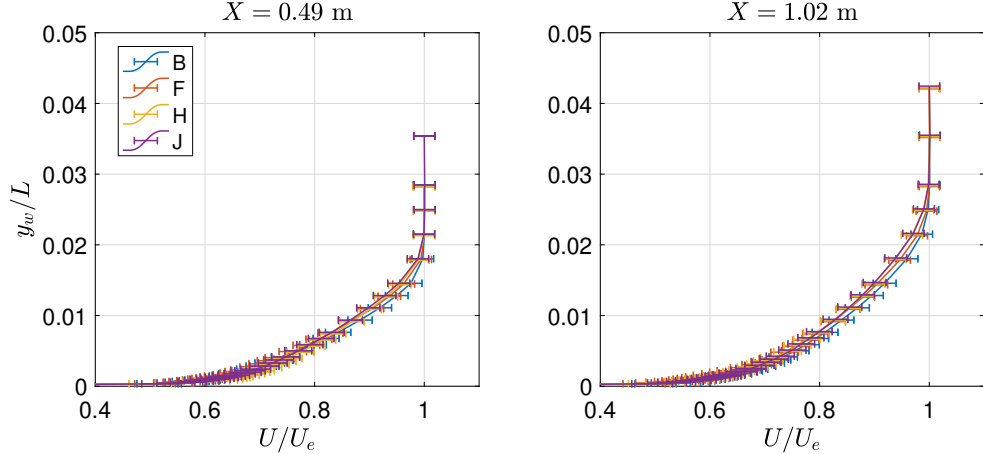


Figure 3.18. Boundary layer profiles obtained on each of the four empty test section side walls at a reference freestream velocity of  $U_\infty = 34$  m/s, corresponding to freestream Mach and Reynolds numbers based on tunnel width of  $M = 0.1$  and  $Re_L = 2.0 \times 10^6$ , respectively. Uncertainty bars indicate a 95% measurement confidence interval.

### 3.2.3 Skin Friction Measurements

In addition to the boundary layer velocity profiles acquired using the hot-wire system, oil-film interferometry measurements were made along the flat plate using the procedure laid out in Section 2.4.4. Figure 3.25 shows the skin friction coefficient along the centerspan of the flat plate. The measurements made with OFI are compared with the indirect Clauser measurements conducted on the boundary layer B profiles (the B profile originated at the plate surface at  $z/L = 0$ , see Figure 3.21). Skin friction measurements can be estimated from the boundary layer profiles using the Clauser method [66]. The logarithmic layer of a TBL follows the relation

$$\frac{U}{u_\tau} = U^+ = \frac{1}{k} \ln(y^+) + B, \quad (3.12)$$

where  $u_\tau = \sqrt{\tau/\rho}$  is the friction velocity, and  $k = 0.384$  (von Kármán constant) and  $B = 4.17$  (additive) are empirical constants for a ZPG TBL [67]. The shear stress,  $\tau$ , in this case is equivalent to the wall shear stress  $\tau_w$ . The wall-normal distance in wall units is  $y^+ = u_\tau y / \nu$  where  $\nu$  is the kinematic viscosity of the air. The value of  $u_\tau$  can be estimated by fitting a curve from Equation 3.12 (linear in a logarithmic plot) to the normalized mean velocity data for each profile. The resulting  $C_f = 2 \left( \frac{u_\tau}{U_\infty} \right)^2$  values acquired using the Clauser method on the TBL profiles are also plotted on 3.25. The  $C_f$  data obtained using various techniques agree well and follow the empirical power-law curve described in [1, 3] for a smooth flat plate TBL at high Reynolds

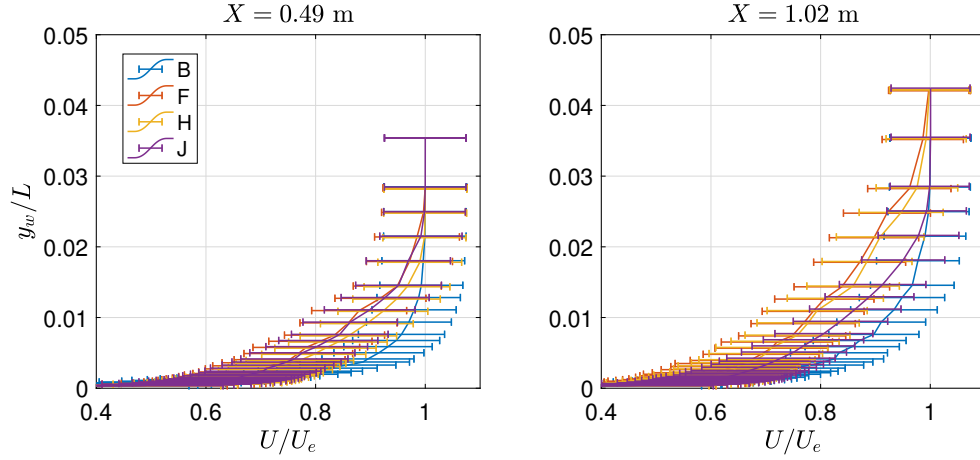


Figure 3.19. Boundary layer profiles obtained on each of the four empty test section side walls at a reference freestream velocity of  $U_\infty = 17$  m/s, corresponding to freestream Mach and Reynolds numbers based on tunnel width of  $M = 0.05$  and  $Re_L = 1.0 \times 10^6$ , respectively. Uncertainty bars indicate a 95% measurement confidence interval.

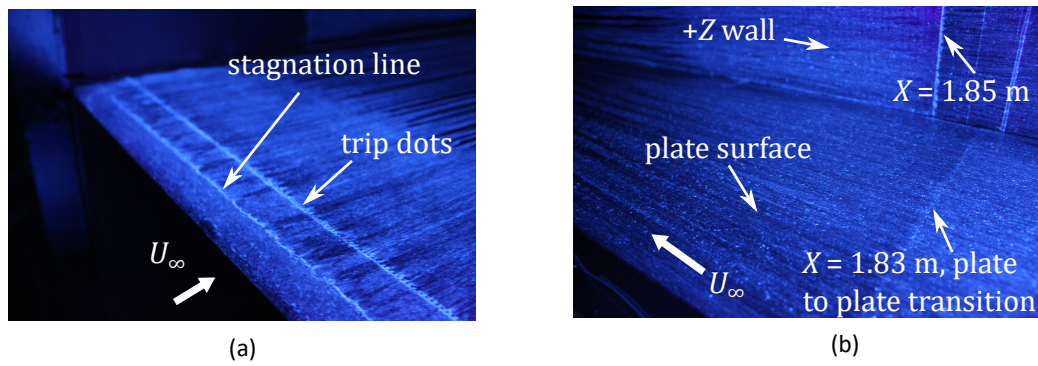


Figure 3.20. Flow visualization for the (a) leading edge of the flat plate and (b) a corner junction between the flat plate and a side wall near  $X = 1.8$  m.

numbers, following the relationship  $C_f = 0.017Re_x^{-0.1237}$ .

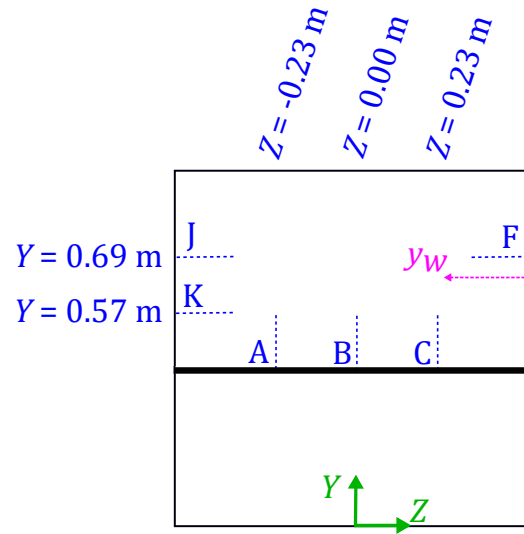


Figure 3.21. Flat plate boundary layer measurement locations and naming convention.

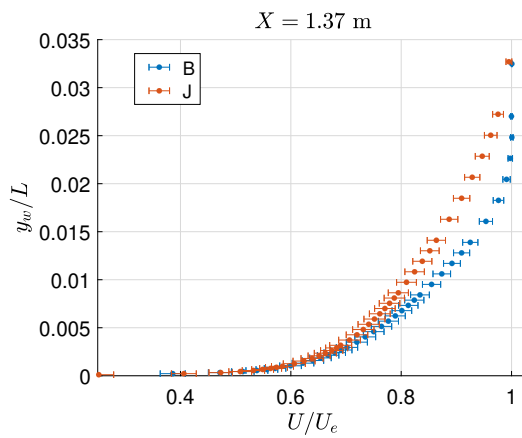


Figure 3.22. Boundary layer profiles obtained on the flat plate surface and a test section side wall at a reference freestream velocity of  $U_\infty = 34\text{ m/s}$ , corresponding to freestream Mach and Reynolds numbers based on tunnel width of  $M = 0.1$  and  $Re_L = 2.0 \times 10^6$ , respectively. Uncertainty bars indicate a 95% measurement confidence interval.

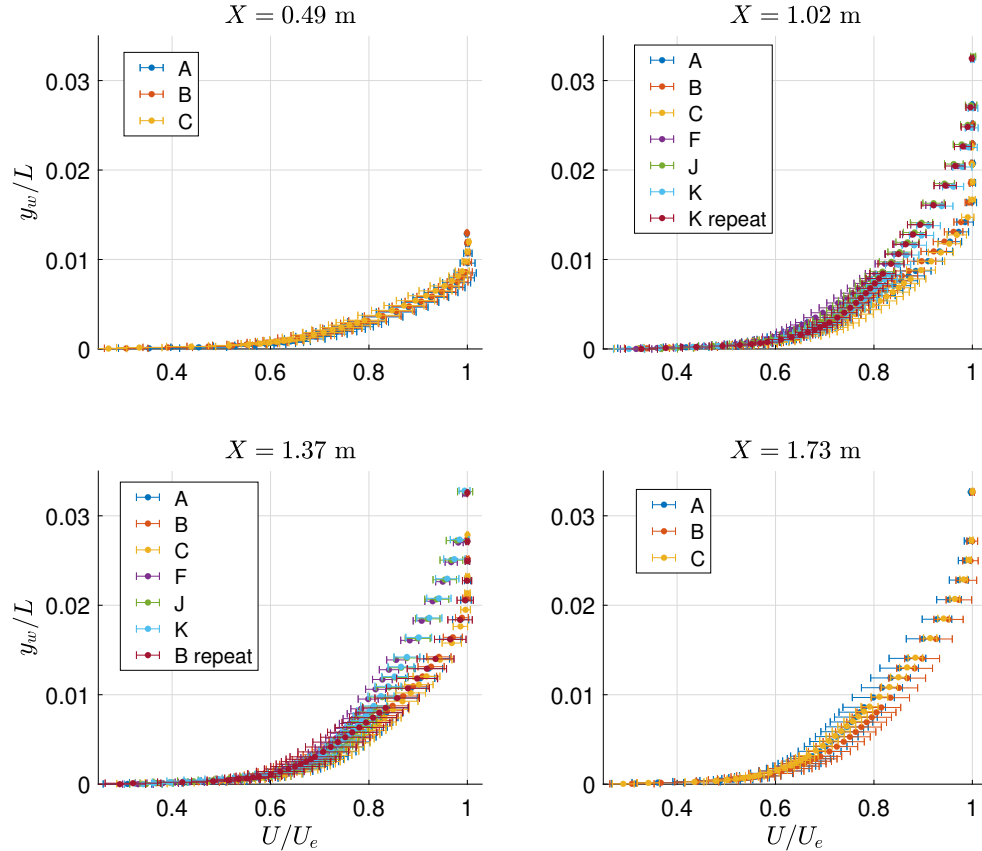


Figure 3.23. Boundary layer profiles obtained on the flat plate surface and test section side walls at a reference freestream velocity of  $U_\infty = 69$  m/s, corresponding to freestream Mach and Reynolds numbers based on tunnel width of  $M = 0.2$  and  $Re_L = 4.0 \times 10^6$ , respectively. Uncertainty bars indicate a 95% measurement confidence interval.

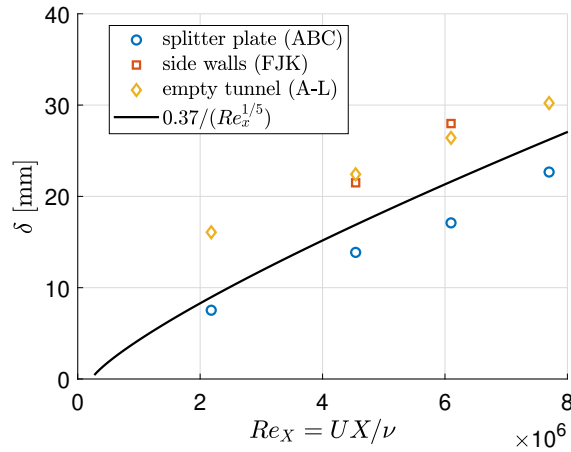


Figure 3.24. Boundary layer thicknesses for the flat plate configuration at  $U_\infty = 69$  m/s ( $M = 0.2$ ,  $Re_L = 4.0 \times 10^6$ ) averaged over the TBL measurements on the plate surface (blue circle) and the side walls (red square) for each streamwise plane. The average boundary layer thicknesses for the empty tunnel case (yellow diamond) and the empirical growth curve for a turbulent boundary layer on a smooth flat plate (Schlichting [2]).

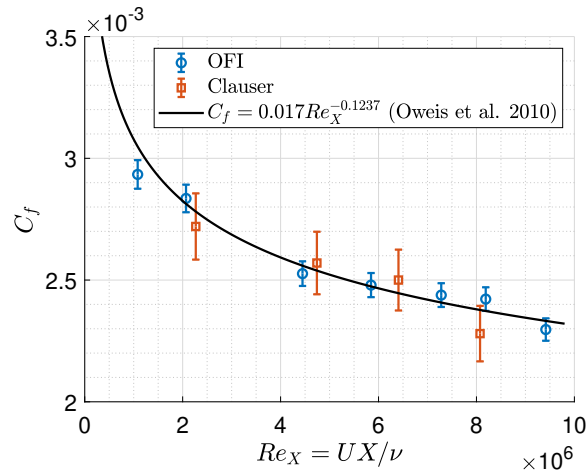


Figure 3.25. Skin friction coefficient over the centerspan of the flat plate configuration at  $U_\infty = 69$  m/s ( $M = 0.2$ ,  $Re_L = 4.0 \times 10^6$ ) using the photogrammetric OFI method (blue circles, with 2% uncertainty bars) and the indirect Clauser method on the flat plate B profiles (red squares with 4% uncertainty bars). The measurements follow the empirical curve of Oweis et al. [3] for a smooth flat plate TBL at high  $Re$ . Reproduced from Fig. 8a of Gluzman et al. [1].

## CHAPTER 4

## DOCUMENTATION OF FLOW OVER THE BUMP

## 4.1 Testing Conditions

Once the bump model was installed into the boundary layer development plate, a series of flow diagnostics were conducted to quantify the flow field over the bump surface. Two experimental parameters were varied to alter the flow field over the bump. The first was the bump location, which was tested closer to the splitter plate leading edge in configuration A and further downstream from the leading edge in configuration B (see Section 2.3 and Figure 2.5). The second was the wind tunnel speed for which a range of values were tested to investigate the sensitivity of the quantities of interest to the freestream velocity. The freestream Mach number was the parameter used as the set point for the wind tunnel controller and will be used herein to denote the flow condition being discussed. A freestream Mach number of  $M_\infty = 0.2$  was the primary flow condition tested, as CFD solvers could be validated without the need for low speed preconditioning. At this condition, the experimental data set for each test location and flow diagnostic tool is comprehensive. For several tests, a sweep of freestream speeds were analysed experimentally, down to a reference Mach number of  $M_\infty = 0.05$ , where the flow was found to remain attached, thus presenting an interesting comparison for flow physics between fully separated and fully attached flows. The range of nominal tunnel conditions set using the reference Pitot probe are presented in Table 4.1.

A high-level tabular summary of all the experimental data obtained with the bump model installed is provided in Table 4.2 which shows the flow speeds tested using each of the diagnostic tools described in Sections 2.4.1-2.4.7. The table also specifies the bump configuration tested at the reference condition (A, B, or both). The quantities measured and corresponding experimental techniques employed include: the boundary layer profiles using the hot-wire anemometry system (HW), the flow fields upstream of the bump using SPIV (SPIV), the surface streamlines in the separated flow region using flow visualization oil (FlowViz), the mean and instantaneous static pressure over the bump ( $C_p$  and Kulite, respectively), the mean skin friction over the bump ( $C_f$ ), the separated flow field downstream of the bump using PIV (PIV), and the separated flow field downstream of the bump in cross-planes using SPIV (SPIVcross). The  $\dagger$  symbol indicates that for  $M = 0.057, 0.064$ , and  $0.070$ , only a single SPIV cross-plane at  $x/L = 0.250$  was taken at those conditions. Additional data summary tables are provided at the start of each subsection of Chapter 4 which indicate the specific locations where data was obtained within the flow field for the measurement type being discussed.

TABLE 4.1

REFERENCE FREESTREAM MACH NUMBERS TESTED AND THE ASSOCIATED VELOCITY AND REYNOLDS NUMBER BASED ON TUNNEL WIDTH.

$M_\infty$	$U_\infty$ [m/s]	$Re_L = U_\infty L / \nu$
0.050	17	$1.0 \times 10^6$
0.057	19	$1.1 \times 10^6$
0.064	22	$1.3 \times 10^6$
0.070	24	$1.4 \times 10^6$
0.075	26	$1.5 \times 10^6$
0.100	34	$2.0 \times 10^6$
0.125	43	$2.5 \times 10^6$
0.150	51	$3.0 \times 10^6$
0.175	60	$3.5 \times 10^6$
0.200	69	$4.0 \times 10^6$

## 4.2 Upstream Flow Development

### 4.2.1 Boundary Layer Development

The boundary layer leading up the bump apex was measured using the hot-wire anemometry system (described in Section 2.4.3) for both bump configurations. Profiles of the centerline TBL were measured using the hot-wire probe traversing vertically to acquire time-averaged mean and turbulent statistics for the streamwise velocity component. The locations of the profiles and the tunnel speeds tested at each bump configuration are given in Table 4.3. Data was sampled at 40 kHz for 30 seconds for about 40 vertical points in the measurement station. Depending on the thickness of the TBL, the number of measurement points in the profile either increased or decreased. Vertical spacing ranged from 0.05 mm for the smallest increment near the surface to 2.0 mm in the outer portion near the freestream velocity. Figure 4.1 shows the mean streamwise velocity profile measured from the bump surface height,  $y_b$ , determined from Equation 2.1. The profiles were obtained at two freestream Mach numbers ( $M_\infty = 0.1$  and  $0.2$ ). The blue symbols indicated that the measurements were taken on the bump in configuration A, and the red symbols are the measurements for configuration B. The location of the leading edge of the bound-

TABLE 4.2

FREESTREAM SPEED TESTED FOR EACH OF THE FLOW  
DIAGNOSTIC TECHNIQUES FOR BUMP CONFIGURATIONS A AND  
B. THE  $\dagger$  SYMBOL INDICATES THAT ONLY A SINGLE  
CROSS-PLANE OF SPIV WAS MEASURED AT THE SPECIFIED  
TUNNEL SPEED.

$M_\infty$	HW	SPIV	FlowViz	$C_p$	Kulite	$C_f$	PIV	SPIVcross
0.050		AB		AB	AB	AB	AB	A
0.057				A	A			A $\dagger$
0.064				A	A			A $\dagger$
0.070				A	A			A $\dagger$
0.075			AB	AB	A			A
0.100	AB	AB	B	AB	AB	AB	AB	A
0.125				A	A			A
0.150		AB		AB	AB			A
0.175				A	A			A
0.200	AB	AB	AB	AB	AB	AB	AB	A

ary layer development plate was  $x/L = 1$  and 2 for configurations A ( $X_{apex} = L$ ) and B ( $X_{apex} = 2L$ ), respectively. The vertical axis is normalized by the test section width  $L$ , and the streamwise velocities are normalized by the outer velocity at each profile,  $U_e$ . The TBL thickness grows with streamwise distance up to  $x/L = -0.469$ . The sensitivity to Mach number is very minimal for each of the streamwise stations. The effect of the different bump configuration can be seen at  $x/L = -0.469$ , where the TBL in configuration case A has not had the same streamwise distance to grow as in case B. At the apex ( $x/L = 0$ ) the acceleration of flow caused by the presence of the bump thins the TBL to a similar shape and size for both configurations.

Integral properties of the TBLs, namely the momentum thickness,

$$\theta = \int_0^\delta \frac{U}{U_\infty} \left(1 - \frac{U}{U_\infty}\right) dy, \quad (4.1)$$

TABLE 4.3

HOT-WIRE BOUNDARY LAYER PROFILE LOCATIONS AND  
TUNNEL SPEEDS.

$M_\infty$	$x/L = -1.683$	$-1.469$	$-0.822$	$-0.683$	$-0.639$	$-0.469$	$-0.083$	$0.000$
0.100	B	B	B	A	B	AB	B	AB
0.200	B	B	B	A	B	AB	B	AB

the displacement thickness,

$$\delta^* = \int_0^\delta \left(1 - \frac{U}{U_\infty}\right) dy, \text{ and} \quad (4.2)$$

and the shape factor,

$$H = \delta^*/\theta, \quad (4.3)$$

were computed using the mean velocity profiles measured with the hot-wire system. Additionally, the viscous boundary layer thickness  $\delta$  was determined via linear interpolation of the velocity data to find the  $y$  (wall-normal) location corresponding to 99% of  $U_\infty$ .

For a zero pressure gradient (ZPG) turbulent boundary layer, expected values for  $H$  are in the range of 1.3-1.5 [4]. One of the objectives of this test was to confirm that a canonical ZPG turbulent boundary layer was developing prior to the flow encountering the strong pressure gradients present near the bump. In addition to shape factor, another way to identify a well-developed TBL is to confirm the presence of the logarithmic region in the mean velocity profiles. An estimate of skin friction can be obtained from the boundary layer profiles using the Clauser method [66], as described in Section 3.2.3, by adjusting the variable  $u_\tau$  so that the mean velocity profile fits the logarithmic relation given by Equation 3.12. Tables 4.4 and 4.5 provide the relevant profile quantities for the  $M_\infty = 0.1$  and  $0.2$  flow cases, respectively. The Reynolds number with respect to streamwise distance ( $Re_X = UX/\nu$ ) and boundary layer momentum thickness ( $Re_\theta = U\theta/\nu$ ) are provided, along with the skin friction coefficients and shape factors. The integral properties and  $C_f$  were not computed for  $x/L > -0.469$  due to high surface curvature and pressure gradients.

For the  $M_\infty = 0.2$  case, the third profile of configuration B ( $x/L = -0.822$ ) was also compared to the composite TBL profile fit developed by Chauhan et al. [4]. This fit was successfully applied to over 500 TBL from 22 sources to recommend a criteria for a well-behaved canonical profile. Another comparison was done using a data set for high Reynolds number ZPG TBLs [5]. In this study, several ZPG

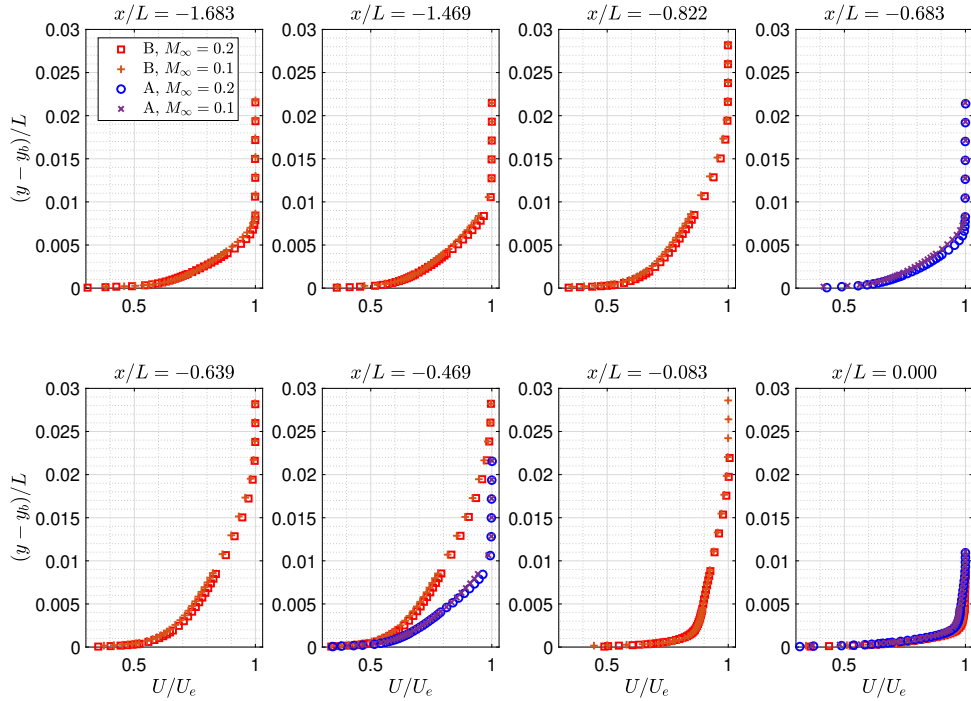


Figure 4.1. Mean streamwise velocity profiles of the incoming TBL measured using the hot-wire anemometry system for bump configurations A (cool colors) and B (warm colors) for  $M_\infty = 0.1$  and  $0.2$ . Vertical distance is referenced from the surface of the bump  $y_b$ . Streamwise velocity is normalized by the local external velocity  $U_e$ .

boundary layers were measured over a range of Reynolds numbers to provide test and simulation validation TBL measurements. The profile used for comparison in this study had a Reynolds number based on momentum thickness of  $Re_\theta = 7.2 \times 10^3$  and  $u_\tau = 0.73$  m/s and was tripped using 40-grit sandpaper at the leading edge of the tunnel inlet. The present test profile had  $Re_\theta = 8.3 \times 10^3$  with  $u_\tau = 2.49$  m/s. The profiles were normalized in outer units and shown in Figure 4.2a, and in viscous units in Figure 4.2b. It is clear that the test data provides evidence of a well-behaved, fully developed TBL which matches both the composite fit profile and the other experimental ZPG TBL, and has an evident logarithmic layer.

The profiles of the RMS values of the streamwise velocity are shown in Figure 4.3. Sensitivities between the freestream speed at individual profile stations is insignificant. At each of the streamwise stations the turbulence peak occurs near the surface and has a peak of  $\sim 12\%$ , then quickly drops to  $\sim 7\%$  with a small increase in distance from the wall. The RMS values are expected to decrease to zero as

TABLE 4.4

INCOMING BOUNDARY LAYER PROPERTIES AT BOTH BUMP  
CONFIGURATIONS FOR THE  $M_\infty = 0.1$  CASE.

Config.	$x/L$	$Re_x$	$Re_\theta$	$H$	$C_f$
A	-0.683	$0.64 \times 10^6$	$1.80 \times 10^3$	1.47	$3.70 \times 10^{-3}$
A	-0.469	$1.07 \times 10^6$	$2.88 \times 10^3$	1.46	$3.10 \times 10^{-3}$
A	0.000	$1.97 \times 10^6$	—	—	—
B	-1.683	$0.64 \times 10^6$	$1.88 \times 10^3$	1.47	$3.60 \times 10^{-3}$
B	-1.469	$1.08 \times 10^6$	$2.76 \times 10^3$	1.44	$3.25 \times 10^{-3}$
B	-0.822	$2.34 \times 10^6$	$4.58 \times 10^3$	1.37	$2.95 \times 10^{-3}$
B	-0.638	$2.71 \times 10^6$	$5.17 \times 10^3$	1.39	$2.80 \times 10^{-3}$
B	-0.469	$3.12 \times 10^6$	$6.62 \times 10^3$	1.42	$2.50 \times 10^{-3}$
B	-0.083	$3.85 \times 10^6$	—	—	—
B	0.000	$4.04 \times 10^6$	—	—	—

$y \rightarrow y_b$ , a trend that was unable to be captured with the hot-wire system. With the streamwise development of the boundary layer, the distance between the surface and the freestream (where  $\sqrt{\overline{u'^2}}/U_e < 1\%$ ) also increases. Measurements are limited to  $y^+ > 10$ , so the expected RMS trend towards zero near the surface is not captured using this method.

The turbulence stress profile at  $x/L = -0.822$  for bump configuration B also was compared to the ZPG TBL data from Marusic et al. [5] described above. The streamwise normal turbulent stress profiles from the present experiment ( $Re_\theta = 8.3 \times 10^3$ , red square) and the reference data ( $Re_\theta = 7.2 \times 10^3$ , black circle) are plotted in viscous units in Figure 4.4.

#### 4.2.2 Upstream SPIV Flow Fields

The SPIV measurement system described in Section 2.4.6.2 was used to obtain mean velocity and turbulence data for the flow approaching and interacting with the upstream side of the bump. The streamwise locations of the center of the SPIV measurement windows and associated tunnel speeds tested for each of the bump configurations are given in Table 4.10. A sample of the velocity data is shown in Figure 4.5 for the bump configuration B and a freestream Mach number of  $M_\infty = 0.2$ . The background color represents the total magnitude of the mean velocity vector [ $U$

TABLE 4.5

INCOMING BOUNDARY LAYER PROPERTIES AT BOTH BUMP  
CONFIGURATIONS FOR THE  $M_\infty = 0.2$  CASE.

Config.	$x/L$	$Re_x$	$Re_\theta$	$H$	$C_f$
A	-0.683	$1.26 \times 10^6$	$3.08 \times 10^3$	1.41	$3.25 \times 10^{-3}$
A	-0.469	$2.11 \times 10^6$	$5.39 \times 10^3$	1.43	$2.60 \times 10^{-3}$
A	0.000	$3.89 \times 10^6$	—	—	—
B	-1.683	$1.28 \times 10^6$	$3.56 \times 10^3$	1.45	$2.90 \times 10^{-3}$
B	-1.469	$2.14 \times 10^6$	$5.04 \times 10^3$	1.41	$2.75 \times 10^{-3}$
B	-0.822	$4.65 \times 10^6$	$8.35 \times 10^3$	1.36	$2.55 \times 10^{-3}$
B	-0.638	$5.32 \times 10^6$	$9.32 \times 10^3$	1.36	$2.50 \times 10^{-3}$
B	-0.469	$6.03 \times 10^6$	$1.20 \times 10^4$	1.39	$2.20 \times 10^{-3}$
B	-0.083	$7.58 \times 10^6$	—	—	—
B	0.000	$7.94 \times 10^6$	—	—	—

TABLE 4.6

CENTER LOCATIONS OF THE UPSTREAM SPIV MEASUREMENT  
WINDOWS AND ASSOCIATED TEST CONDITIONS RUN FOR EACH  
OF THE BUMP CONFIGURATIONS.

$M_\infty$	$x/L = -0.5$	$-0.37$	$-0.21$	$-0.18$	$-0.04$
0.050	B	A	B	A	AB
0.100	B	A	B	A	AB
0.150	B	A	B	A	AB
0.200	B	A	B	A	AB

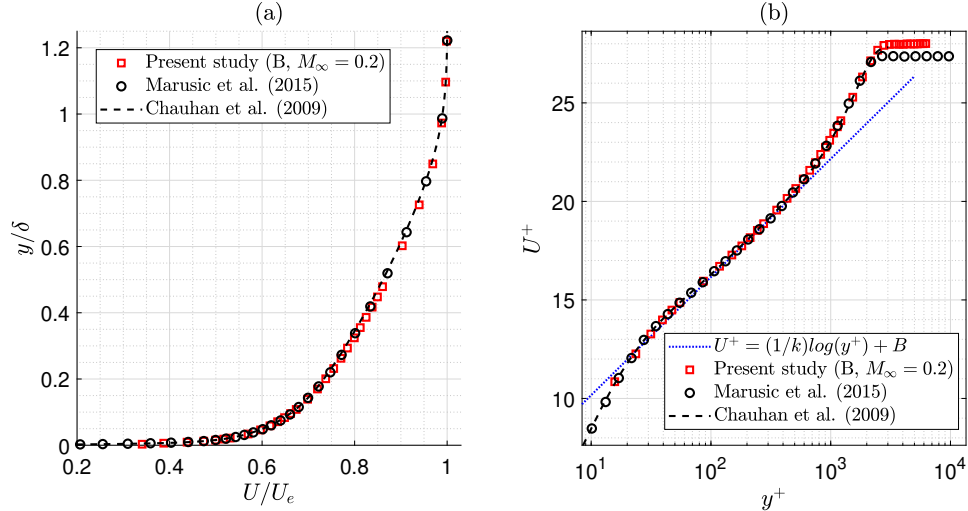


Figure 4.2. Boundary layer mean velocity profile obtained using the hot-wire system at  $x/L = -0.822$  in bump configuration B compared to a composite fit [4], and another experimentally acquired ZPG TBL [5] at a similar  $Re_\theta$ , plotting in (a) outer variable scaling and (b) viscous unit scaling.

$V W]$ , obtained from the sum of squares so that  $U_{total} = \sqrt{U^2 + V^2 + W^2}$ . The velocity was normalized by the reference velocity measured at the Pitot-static probe near the test section inlet ( $U_\infty$ ). The streamlines shown in white follow the direction of  $[U V]$ . The upstream-most location shows the flow in a region where the influence of the bump is minimal, i.e., before the flow is accelerated by the bump. Velocity measurements within the boundary layer were captured to within 0.9 mm of the wall, corresponding to  $y^+ \approx 140$  at  $x/L = -0.5$ . At this position, the flow is parallel to the streamwise direction, and has not yet encountered the pressure gradients or the surface curvature associated with the bump. At the second location the mean flow changes direction as the streamlines follow the contours of the bump surface, and the favorable pressure gradient accelerates the fluid. The boundary layer is still visible, but it begins to thin. At the third station near the apex, the fluid has been accelerated to a velocity almost 50% higher than at the reference probe. The boundary layer has thinned enough that much of its profile is not captured by the SPIV measurement. The streamlines continue to follow the surface curvature because the flow remains attached up to the bump apex. Figure 4.6 provides the individual scalar components of the mean velocity and turbulent stresses captured using the SPIV setup for the upstream flow development.

Several hot-wire boundary layer profiles were obtained in regions also investigated with SPIV. A comparison of the streamwise velocity and turbulence intensity RMS

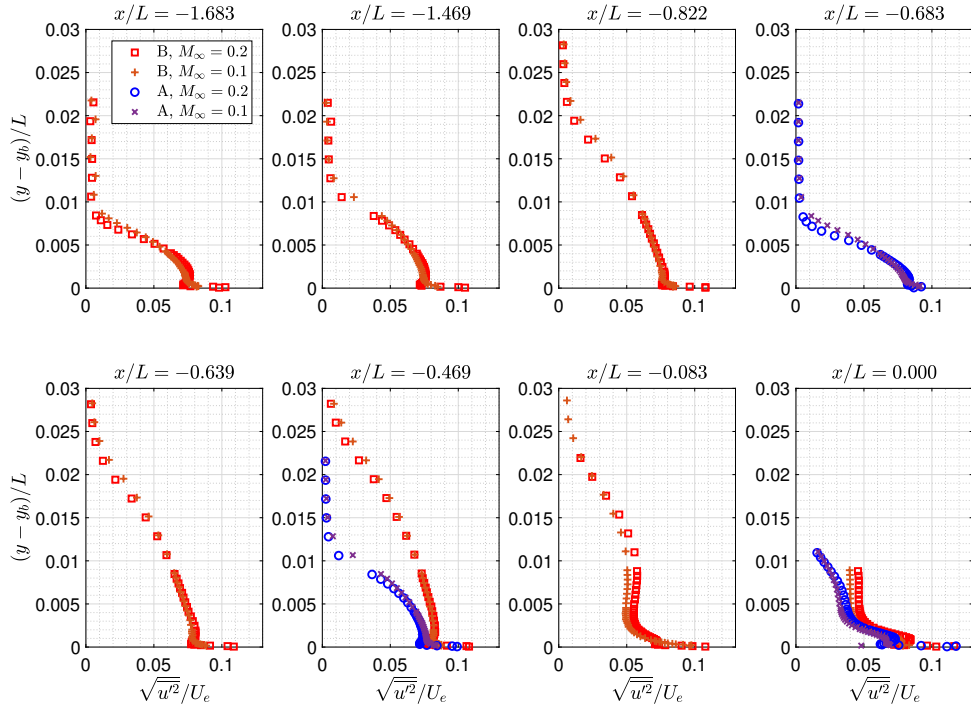


Figure 4.3. Streamwise RMS turbulence profiles of the incoming TBL measured using the hot-wire anemometry system for bump configurations A (cool colors) and B (warm colors) for  $M_\infty = 0.1$  and  $0.2$ . Vertical distance is referenced from the surface of the bump  $y_b$ . Turbulence data is normalized by the local external velocity  $U_e$ .

profiles taken at  $x/L = -0.469$  for both hot-wire and SPIV at the  $M_\infty = 0.2$  case are shown in Figure 4.7. The mean velocity profiles are in excellent agreement. Despite the lack of SPIV data for  $y/L < 0.001$  because of the laser light reflection, a majority of the boundary layer profile was captured and aligns well with the profile measured using the hot-wire technique. The streamwise turbulence intensities are similar but the peak turbulence intensity values near the surface are different in magnitude by about 0.6%. Additionally, the SPIV returned a higher freestream turbulence intensity of about 1.6%, while the hot-wire measurement had a value of 0.3%. Some of this difference can be attributed to measurement uncertainty. Mean velocity fields obtained with SPIV can have relatively low uncertainty because the noise inherent in the individual instantaneous fields is attenuated by the averaging process. The more instantaneous fields obtained, the more the noise is mitigated. Conversely, derived statistics like turbulence intensity are computed from the noisy instantaneous velocity fields and the noise is not attenuated by the averaging process because the

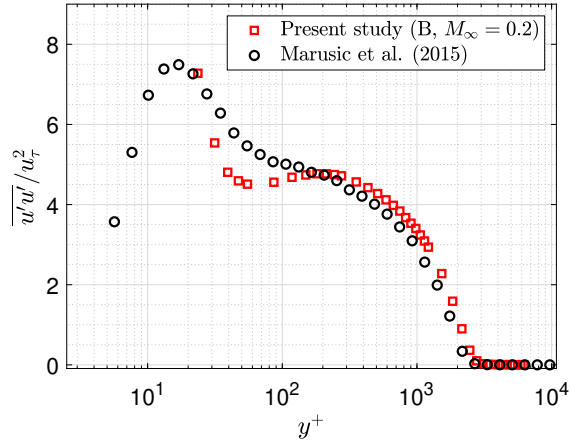


Figure 4.4. Boundary layer turbulence profile obtained using the hot-wire system at  $x/L = -0.822$  in bump configuration B (red squares) compared to data from another experimentally acquired ZPG TBL [5] at a similar  $Re_\theta$  (black circles), plotting in viscous unit scaling. The profile from the present experiment used a friction velocity of  $u_\tau = 2.49$  m/s; the other used  $u_\tau = 0.73$  m/s.

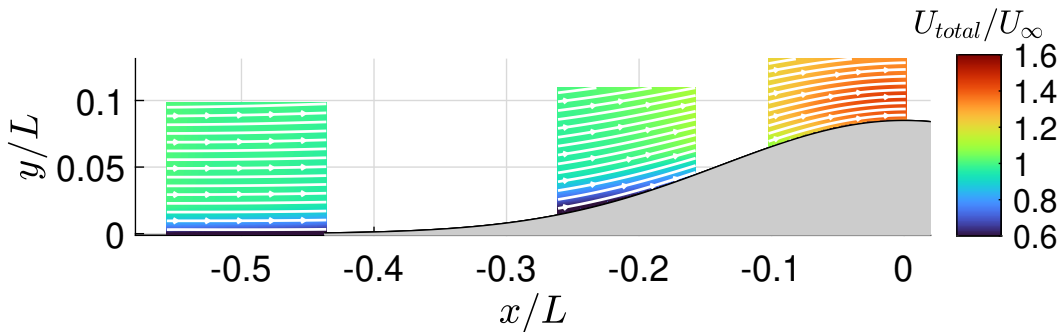


Figure 4.5. Total velocity field measured using the SPIV system upstream of the bump apex at three interrogation windows for the B configuration at  $M_\infty = 0.2$ . White streamlines follow the  $[U \ V]$  flow vectors.

velocity fluctuation components are multiplied by each other (e.g.  $u'u'$  or  $u'v'$  etc.). Therefore, turbulence intensities calculated within regions of low turbulence tend to be overstated by PIV due to the noise in the instantaneous velocity fields.

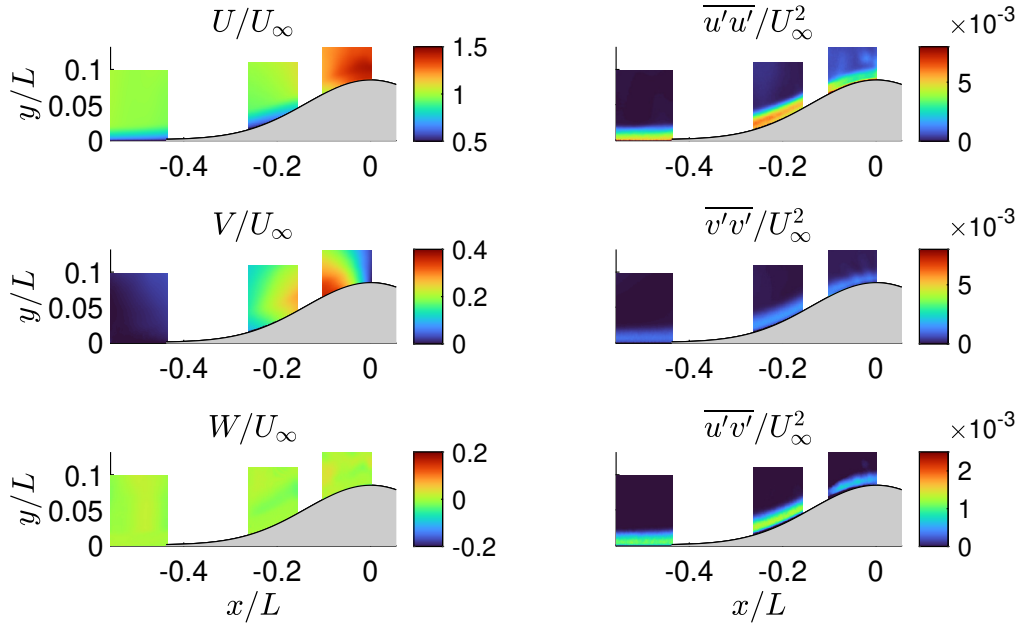


Figure 4.6. Normalized mean and turbulent stress components measured on the upstream side of the bump in the B configuration using SPIV at  $M_\infty = 0.2$ .

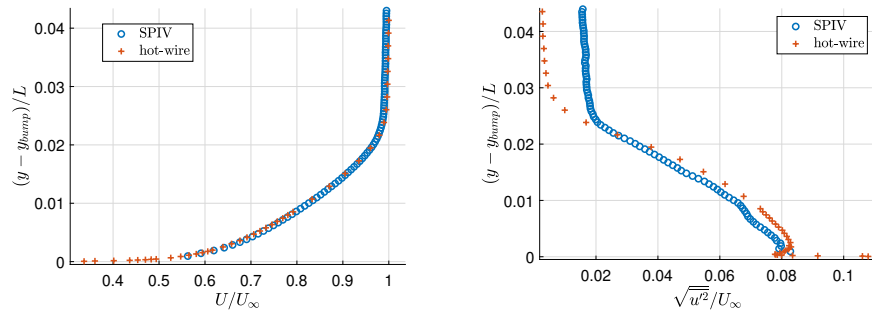


Figure 4.7. Comparisons of the boundary layer profile measurements between SPIV and hot-wire for the normalized (a) mean streamwise velocity and (b) streamwise turbulence intensity RMS obtained at  $x/L = -0.469$  in bump configuration B at  $M_\infty = 0.2$ .

### 4.3 Surface Streamlines

The fluorescent oil mixture described in Section 2.4.1 was applied to the downstream region of the bump to visualize the time-mean surface streamlines produced by the separated flow. Both bump configurations were tested at flow speeds ranging from  $M_\infty = 0.075$  to 0.2. Below the  $M_\infty = 0.075$  case, the oil mixture was too viscous to be sheared by the surface stresses. Figure 4.8 shows the separated flow topology at  $M_\infty = 0.2$  for bump configuration A. The flow is moving from top to bottom, with the apex highlighted by the horizontal orange line near the top of the photograph. In this image three orange markers are used to locate the centerspan line at  $z/L = 0$ , with two more fiducial markers on either side at  $z/L = \pm 6.4$  mm (0.25 in). The plane where the two halves of the bump section were joined together after fabrication can be recognized 25.4 mm (1 in) to the right of the centerline. While visually conspicuous when covered with the fluorescent oil, the junction did not affect the flow field. This line just slightly alters the observed surface flow pattern, and can be distracting to the eye. The small blue horizontal tick marks indicate 51 mm (2 in) arc length increments beginning at the downstream edge of the plate section (in this example the downstream edge is located at  $X = 1.32$  m). The green crosses are located at  $z/L = \pm 0.25$ . The top pair of crosses is at  $x/L = 0.06$ , and the bottom are at  $x/L = 0.39$ .

The separation topology is consistent with the *owl-face pattern* of the 1st kind, as described by Perry and Hornung[68]. The basic features of this type of three-dimensional separated flow is described by Delery [6], and the mathematical theory was provided by Tobak and Peake[69]. The eyes of the owl-face pattern are the symmetric foci labeled **F1** and **F2**. They are the origin of lifting vortices that spiral away from bump surface. Above the foci on the centerspan is a saddle point **S1** where the flow bifurcates into a separated streamsurface **S** shown by the dashed line. The saddle point diverts the flow into **F1** and **F2**, where the flow must lift off of the surface in accordance with the Helmholtz vortex theorem (i.e. a vortex tube cannot end within a fluid). The region just downstream of this line exhibits flow reversal which is caused by the suction of the strong APG pulling fluid upstream. Farther downstream another critical line labelled **R** can be found where the separated streamsurface reattaches to the surface. The reattachment saddle point node **S2** is the symmetric center of the reattachment line at the tunnel centerspan.

The centerline separation point (**S1**) is located at the upstream-most tick mark, which was made at  $x/L = 0.06$ . Centerline reattachment (**S2**) occurred half-way between two of the marking lines at  $x/L \approx 0.36$ . The streamwise extent of mean separation in the case shown in Figure 4.8 was  $0.30L$  for the centerspan. The centerspan plane,  $z/L = 0$ , was determined to be the plane of symmetry for the flow topology. For the owl-face pattern of the first kind, this is also the plane with the largest distance from mean separation to reattachment. The foci were measured at a streamwise location of  $x/L \approx 0.14$ . The geometry inflection point of the bump surface, where curvature changes from convex to concave, is located  $x/L = 0.138$ . The change of concavity at the inflection point is suspected to play a role in vortex development.

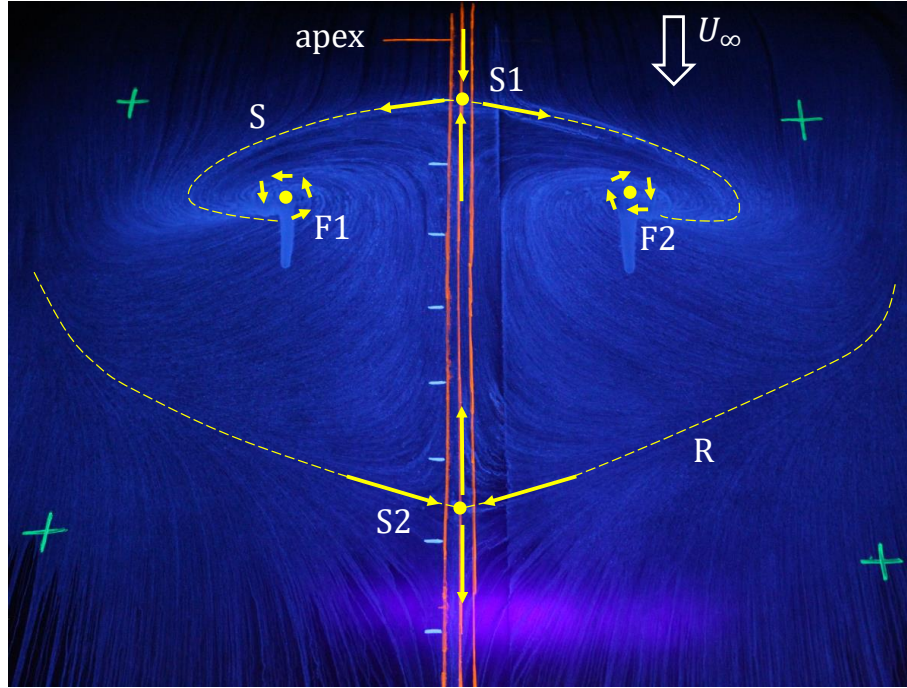


Figure 4.8. Downstream flow topology for bump configuration A at  $M_\infty = 0.2$  using fluorescent oil flow visualization, flow from top to bottom. Critical features were identified and denoted using notation from [6]. Surface markings were used to estimate the distance between mean separation and reattachment.

## 4.4 Surface Static Pressure

### 4.4.1 Time-Averaged Surface Pressure

The bump model was instrumented with several arrays of pressure taps to quantify the time-mean surface static pressure field across the bump. The experimental setup used to acquire the  $C_p$  data can be found in Section 2.4.7.1. The tap arrays and tunnel speeds tested for each of the bump configurations are given in Table 4.7.

Figures 4.9, 4.10, and 4.11 provide the  $C_p$  curves on the centerline ( $z/L = 0$ ), along two off-center streamwise axes ( $z/L = -0.083$  &  $-0.167$ ), and along two lateral axes ( $x/L = 0$  &  $0.138$ ), respectively. The data is shown for configuration A for the full range of freestream tunnel speeds. Error bars are shown at each tap location to indicate a 95% confidence interval. The full uncertainty analysis conducted on the measurements is presented in Appendix D.5.

Beginning upstream near  $x/L = -0.6$  on the centerline, shown in Figure 4.9, the surface pressure is close to the freestream static pressure, i.e.,  $C_p$  is roughly zero. Upstream of the first pressure port, the TBL is subjected to a nominally

TABLE 4.7

LOCATIONS OF THE STREAMWISE ARRAYS (LEFT) AND THE SPANWISE ARRAYS (RIGHT) AND THE NUMBER OF TAPS IN EACH, AND THE TUNNEL SPEED RUN FOR EACH OF THE BUMP CONFIGURATIONS.

$M_\infty$	$z/L = 0$ (x39)	$-0.083$ (x15)	$-0.167$ (x15)	$x/L = 0$ (x21)	$0.138$ (x13)
0.050	AB	AB	AB	AB	AB
0.057	A	A	A	A	A
0.064	A	A	A	A	A
0.070	A	A	A	A	A
0.075	AB	AB	AB	AB	AB
0.100	AB	AB	AB	AB	AB
0.125	A	A	A	A	A
0.150	AB	AB	AB	AB	AB
0.175	A	A	A	A	A
0.200	AB	AB	AB	AB	AB

ZPG ( $dC_p/dx \approx 0$ ). Approaching the bump section and the beginning of the concave curvature at  $x/L = -0.4$ , the static pressure is greater than zero, indicating a slight adverse pressure gradient (APG) due to the blockage of the bump. The pressure curves reach a maximum at  $x/L \approx -0.3$ , where the gradient crosses zero prior to flipping sign to that of a FPG due to the presence of the bump which accelerates the fluid by reducing the flow area.

Starting near  $x/L = -0.2$ , both at the centerline and at the offspan arrays (Figure 4.10) the surface pressure begins to drop rapidly (i.e, a FPG develops) due to the acceleration of the flow as the flow area contracts. Peak suction occurs just upstream of the apex at  $x/L = -0.02$  where the pressure gradient crosses zero and becomes adverse.

The lateral array of pressure taps on the apex (Figure 4.11) reveal that the lowest pressures (and highest flow velocity) occur towards the bump centerspan but that the magnitude of the local pressure extrema is lower offspan near the bump shoulders. As the tunnel speed increases, a concavity in the peak suction along the apex develops, and is more pronounced at larger tunnel velocities. The slight concavity or "dip"

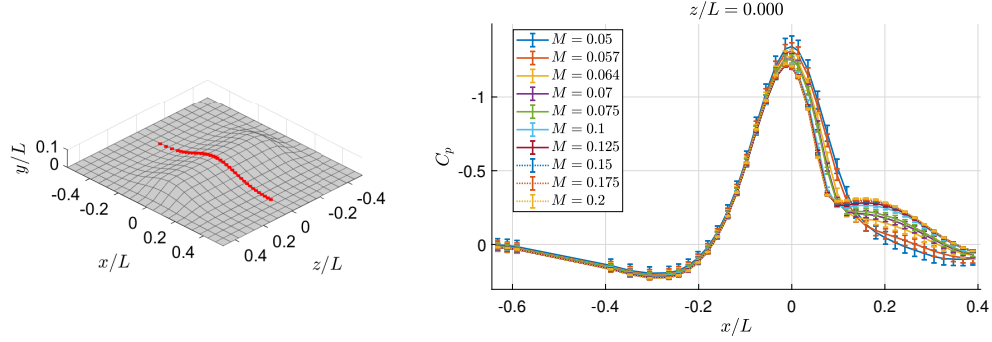


Figure 4.9. Time-averaged pressure coefficient distribution measured using surface taps along the bump centerline,  $z/L = 0$ , for the bump configuration A at various tunnel speeds. Uncertainty bars indicate a 95% measurement confidence interval. The locations of the pressure taps are denoted in red on the bump geometry on the left plot.

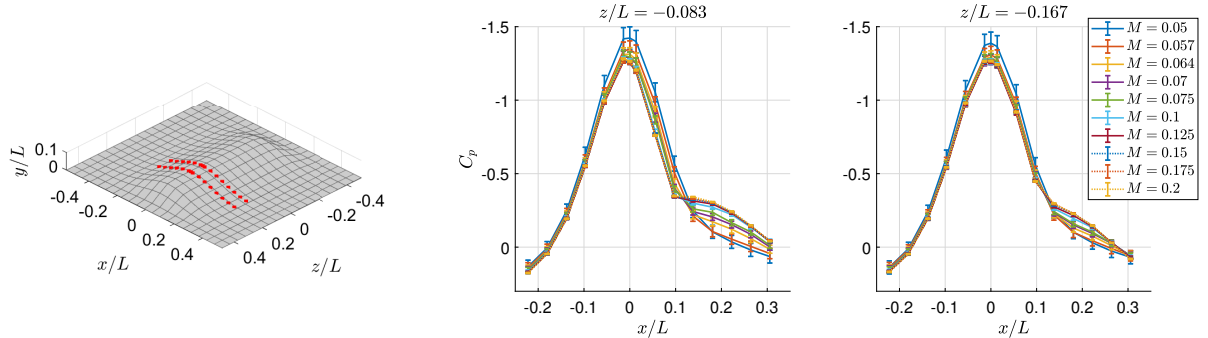


Figure 4.10. Time-averaged pressure coefficient distribution measured using surface taps on the  $z/L = -0.083$  and  $-0.167$  planes, for the bump configuration A at various tunnel speeds. Uncertainty bars indicate a 95% measurement confidence interval. The locations of the pressure taps are denoted in red on the bump geometry on the left plot.

near the bump centerline is likely due an upstream moving pressure effect from the presence of the separation region. As the size of the separation region grows, the dip in pressure suction on the centerline increases in depth. For the highest tunnel Mach number,  $M_\infty = 0.2$ , the peak suction does not occur at the centerline, but rather near  $z/L = \pm 0.2$ , with minor asymmetry. Moving farther offspan towards the bump shoulders, the magnitude of suction decreases as the flow is less accelerated due to the flow area cross-section increase towards the bump shoulders. Comparisons were also

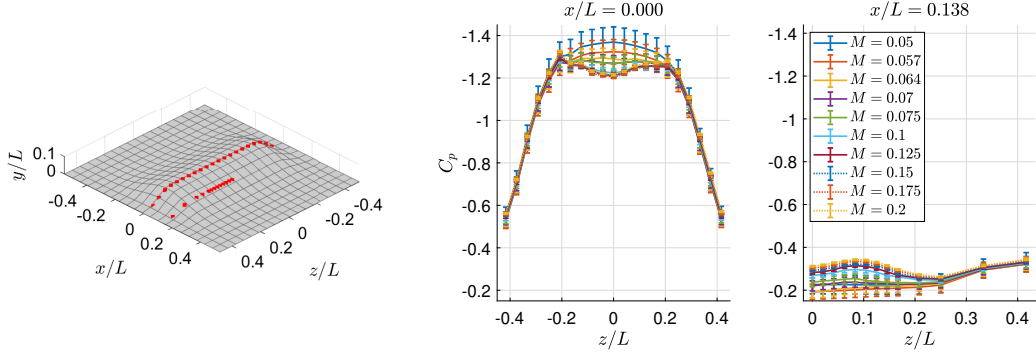


Figure 4.11. Time-averaged pressure coefficient distribution measured using surface taps on the apex ( $x/L = 0$ ) and at the downstream geometric inflection point ( $x/L = 0.138$ ), for the bump configuration A at various tunnel speeds. Uncertainty bars indicate a 95% measurement confidence interval. The locations of the pressure taps are denoted in red on the bump geometry on the left plot.

made for the spanwise oriented profiles located on the bump apex and the geometric inflection point of the bump ( $x/L = 0.138$ ). At the inflection point, a pair of counter-rotating vortices originating on the bump which lift off from the surface were identified using flow visualization (see Figure 4.8). Thus, it was deemed appropriate to place an array of pressure taps here to identify the effect of high vorticity on the pressure field. The array of taps also provide a valuable data set for comparison with simulations, as it captures the spanwise distribution of reversed flow pressures in the centerline and passes through the surface reattachment point towards the bump shoulders.

#### 4.4.2 Instantaneous Surface Pressure

Dynamic pressure measurements were taken on the downstream side of the bump using the Kulite sensors described in Section 2.4.7.2. The locations and tunnel speeds ran at each of the bump configurations is shown in Table 4.8.

The time-average data was compared to the centerline  $C_p$  distribution obtained using static pressure taps (see Sections 2.4.7.1 and 4.4.1). Figure 4.12 shows the mean pressure data obtained by the Kulite sensors at a nominal freestream Mach number of  $M_\infty = 0.2$  in configuration A, compared to data obtained using pressure taps at the same test condition. The mean Kulite pressure measurements are in very good agreement with the static pressure measurements.

The pressure RMS ( $\sqrt{p^2}$ ) for the time-series of pressure signals were used to evaluate the intensity of turbulence in the separation bubble, as the turbulent interactions off the wall were felt by the pressure field at the wall. Figure 4.13 shows the RMS of the six pressure signals normalized by the reference dynamic pressure,  $q_\infty = P_0 - P_\infty$ . Pressure fluctuations grow beginning upstream of mean separation

TABLE 4.8

KULITE DYNAMIC PRESSURE SENSOR LOCATIONS AND TUNNEL SPEEDS RUN FOR EACH OF THE BUMP CONFIGURATIONS.

$M_\infty$	$x/L = 0.076$	0.138	0.201	0.264	0.326	0.389
0.050	AB	AB	AB	AB	AB	AB
0.057	A	A	A	A	A	A
0.064	A	A	A	A	A	A
0.070	A	A	A	A	A	A
0.075	A	A	A	A	A	A
0.100	AB	AB	AB	AB	AB	AB
0.125	A	A	A	A	A	A
0.150	AB	AB	AB	AB	AB	AB
0.175	A	A	A	A	A	A
0.200	AB	AB	AB	AB	AB	AB

at the upstream-most sensor K1 as the reversed flow creates large spanwise oriented vorticity. The growth in the fluctuation intensity subsides with the final sensor K6, which is located downstream of mean reattachment.

The power spectral density of the pressure signals were also analysed to identify relevant frequency modes of the separated shear layer. The auto spectrum of the fluctuations of pressure signal  $p'(t) = p(t) - P$ , is denoted as  $S_{xx}$ , where  $p(t)$  is the time-series pressure signal and  $P$  is the time-average pressure. Figure 4.14 shows the auto spectra for all six sensors premultiplied by the frequency at the  $M_\infty = 0.2$  test condition for both bump configurations. The acquisition frequency was 100 and 250 kHz for configurations A and B, respectively. The premultiplied auto spectra for each of the six sensors are shown, averaged over 200 ensembles with a Hanning window applied to reduce spillage between adjacent frequencies. The premultiplied spectra provide insight to the development of the shear layer. In the four downstream most sensors, K3-K6, a visible energy peak can be identified near 190 and 230 for the A and B configurations, respectively. These sensors are downstream of the shear layer development, and are detecting the waves associated with the spanwise oriented roll-up caused by the large wall-normal velocity gradient in the streamwise velocity. This frequency mode can be seen developing with streamwise distance. In the upstream most sensor, K1, there is no visible energy peak, as the flow has not yet separated (in the time-mean sense). At sensor K2, the shear layer has begun to develop, and

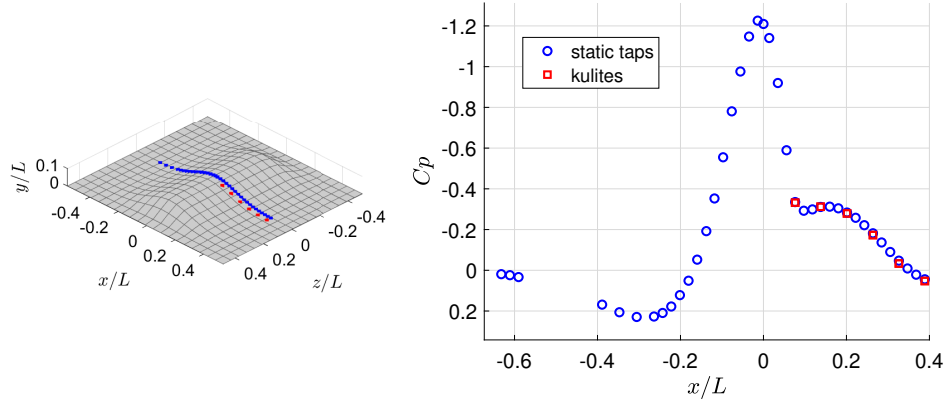


Figure 4.12. Mean static pressure coefficient measured by pressure taps ( $z/L = 0$ ) and Kulite sensors ( $z/L = 0.028$ ) for configuration A at  $M_\infty = 0.2$ . The locations of the pressure taps and Kulites are denoted on the bump geometry on the left plot by blue and red symbols, respectively.

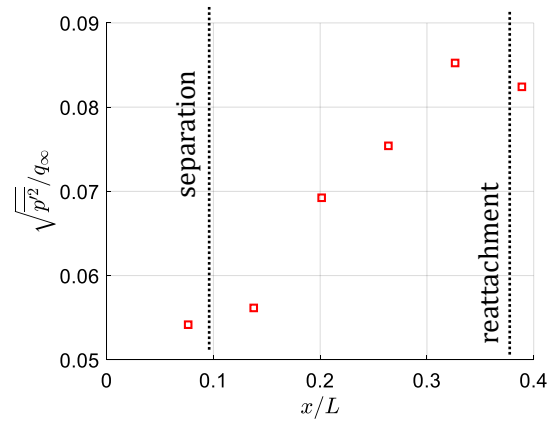


Figure 4.13. Static pressure fluctuation RMS normalized by the reference dynamic pressure for configuration A at  $M_\infty = 0.2$ .

the pressure spectrum grows in magnitude. By the location of sensor K3, the shear layer is well developed.

Data was obtained at each sensor for a range of Mach numbers. Figure 4.15 shows the auto spectra of the pressure signals obtained by K4 for each of the freestream tunnel speeds tested for both bump configurations. With increasing tunnel speeds, the spectral energies of the pressure fluctuations increase, and the peaks are found

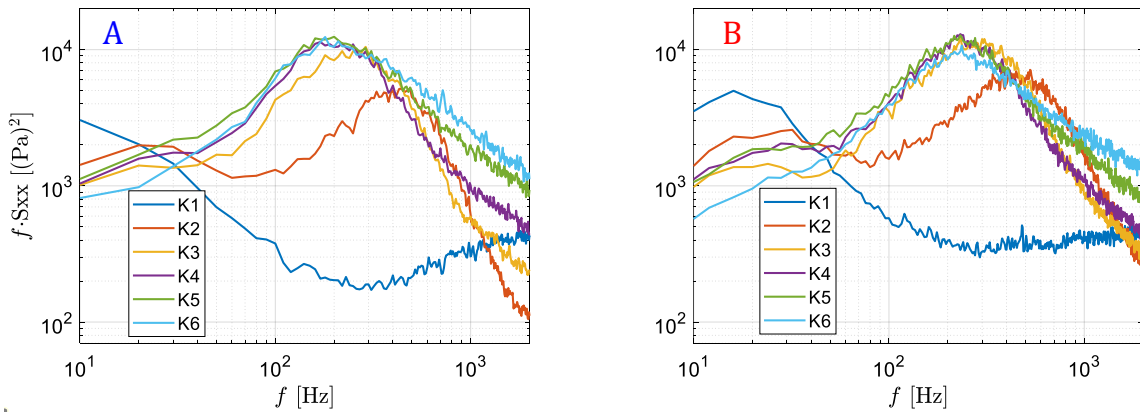


Figure 4.14. Premultiplied auto spectra of the pressures measured using the Kulite sensors, showing a peak frequency of  $\sim 190$  Hz for configuration A and  $\sim 230$  Hz for B.

at higher frequencies.

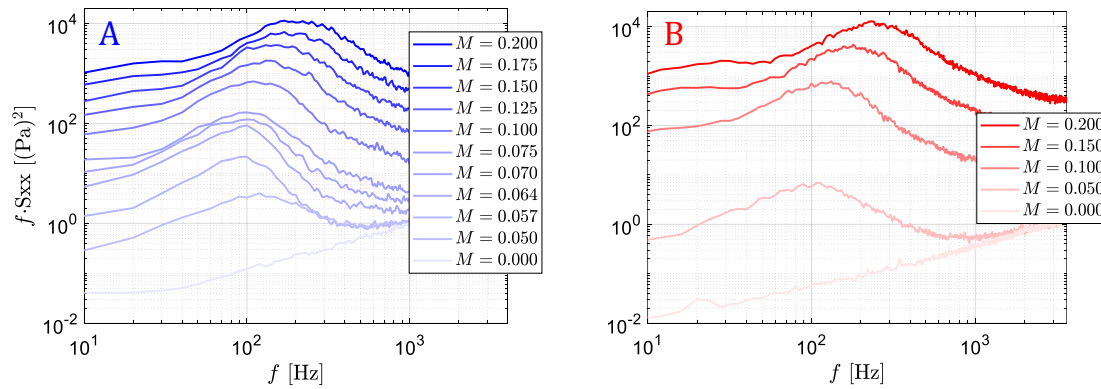


Figure 4.15. Premultiplied auto spectra of the pressures measured using the K4 sensor at each of the reference speeds tested.

#### 4.5 Surface Skin Friction

The skin friction coefficient development over the centerline of the bump was measured directly using the photogrammetric OFI method described in Section 2.4.4, as well as indirectly at discrete boundary layer profile locations using the Clauser method (see Section 3.2.3 for details). The Clauser method was applied to the TBL mean velocity profiles, assuming a ZPG, to obtain the values that are provided in Tables 4.4 and 4.5. The  $C_f$  data are plotted for both bump configurations at freestream speeds of  $M_\infty = 0.2, 0.1$  and  $0.05$  in Figures 4.16, 4.17 and 4.18, respectively. The uncertainty bands for many of the data points are the same size or smaller than the symbols used.

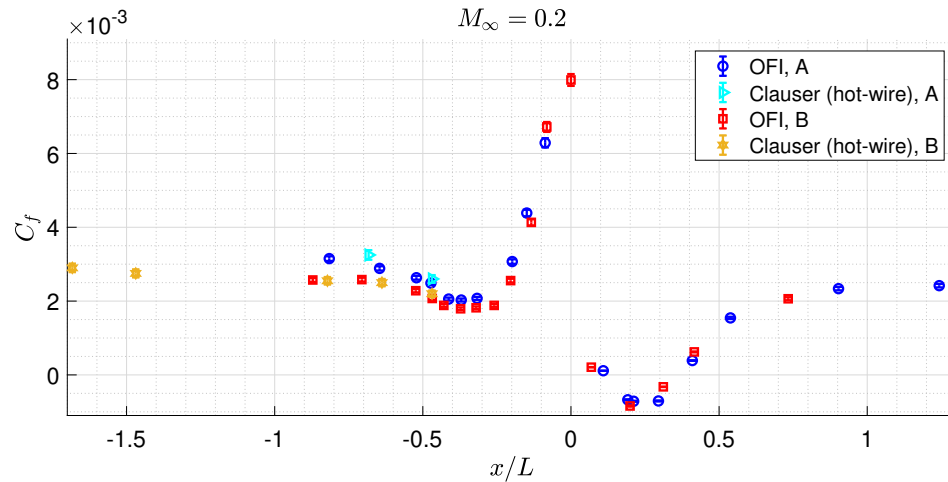


Figure 4.16. Skin friction coefficient distribution for the  $M_\infty = 0.2$  case obtained using OFI for bump configurations A (blue circles) and B (red squares) with 2% uncertainty bands, and using the Clauser method on TBL velocity profiles obtained via hot-wire in configurations A (cyan sideways triangles) and B (yellow hexagons) with 4% uncertainty bands.

The data at  $M_\infty = 0.1$  and  $0.2$  from the OFI and Clauser methods agree well for the corresponding bump configuration and tunnel speed combinations. Moving the bump location farther downstream increases the Reynolds number based on boundary layer thickness (Tables 4.4 and 4.5). Increased thickness yields lower skin friction values upstream of the bump apex. In the region beginning near the leading edge of

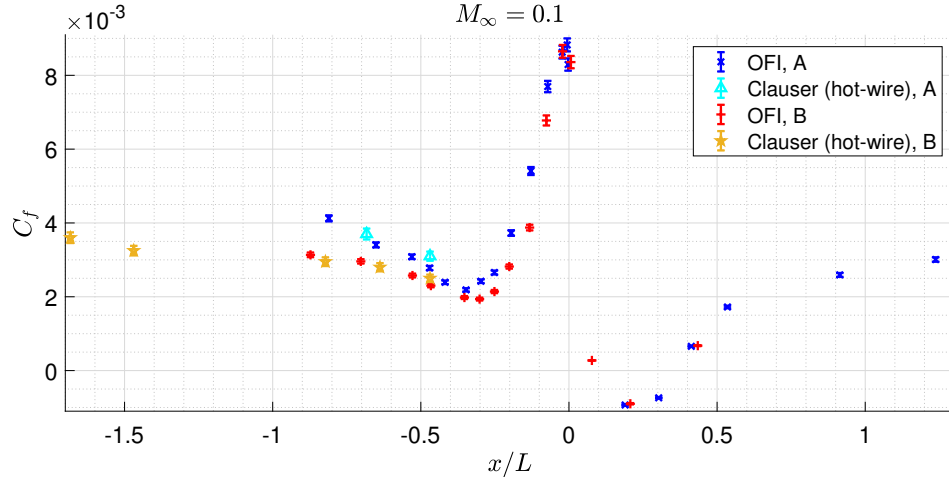


Figure 4.17. Skin friction coefficient distribution for the  $M_\infty = 0.1$  case obtained using OFI for bump configurations A (blue 'x') and B (red '+') with 2% uncertainty bands, and using the Clauser method on TBL velocity profiles obtained via hot-wire in configurations A (cyan upright triangle) and B (yellow pentagram) with 4% uncertainty bands.

the plate, the skin friction values decrease towards the bump. For the other regions (just upstream of the bump, on, and downstream of the bump) the experimental cases yield very similar skin-friction profiles. In these regions, close to the upstream portion of the bump, the FPG accelerates the flow, and an increase in skin friction is evident until about  $x/L = -0.05$ , where a primary  $C_f$  peak is obtained. At this point  $C_f$  begins to drop quickly. Downstream of the bump apex, negative  $C_f$  values were acquired in the separated flow region, where a reverse oil flow pattern was observed. In the case of  $M_\infty = 0.05$ , the profile departs from other skin friction profiles obtained for higher freestream velocities, where a kink is observed at  $x/L = -0.5$  (upstream of the bump). Also for this case, no reversed flow was detected in the OFI measurements.

#### 4.6 PIV in Separation Region

Velocity data was acquired in the downstream region of the bump using the PIV system described in Section 2.4.5. The two-component PIV setup provided time-averaged velocity fields of the streamwise and vertical components of velocity and turbulence. The spanwise locations and tunnel speeds tested using the PIV technique for each of the bump configurations is given in Table 4.9. Each measurement planes extended approximately  $0.3 < x/L < 0.5$  except for the  $z/L = -0.250$  plane in the B configuration, which was limited to  $0.3 < x/L < 0.34$  due to difficulties acquiring the downfield half of the stitched plane..

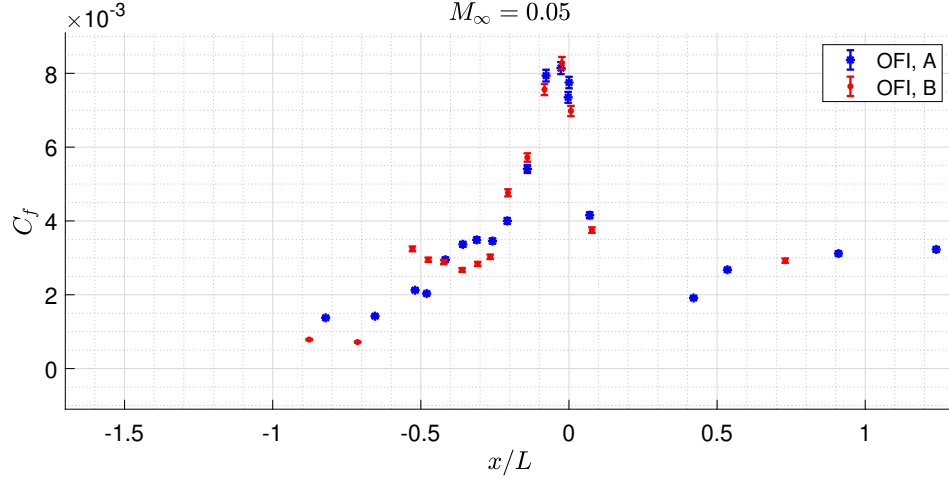


Figure 4.18. Skin friction coefficient distribution for the  $M_\infty = 0.05$  case obtained using OFI for bump configurations A (blue asterisks) and B (red dots) with 2% uncertainty bands.

TABLE 4.9  
LOCATIONS AND TUNNEL SPEEDS RUN FOR BOTH BUMP  
CONFIGURATIONS USING PIV.

$M_\infty$	$z/L = -0.250$	$-0.167$	$-0.083$	$0.000$	$0.083$
0.050	AB	AB	AB	AB	AB
0.100	AB	AB	AB	AB	AB
0.200	AB	AB	AB	AB	AB

Figure 4.19 shows the flow quantities measured for the centerspan ( $z/L = 0$ ) measurement plane at a freestream speed of  $M_\infty = 0.2$  in the A configuration. The measurement begins just downstream of the bump apex, and upstream of the mean flow separation. The streamwise velocity,  $U$ , quickly decelerates after crossing the apex, where the APG dominates the flow. Separation occurs on the surface of the bump near  $x/L = 0.08$ , and a shear layer develops between the reversed flow and the freestream. Figure 4.20 shows the  $U$  component of velocity for the same case ( $z/L = 0$ )

$0, M_\infty = 0.2$ , configuration A) with a few vertical profiles shown along the surface of the bump. Dotted lines indicate where  $U = 0$  in each of the profiles. The background is normalized by the freestream velocity, so that a clear distinction between mean downstream flow and reversed flow is made. The backflow is highlighted in red, while fluid moving downstream is blue. The reversed flow region is clear, and backflow velocity magnitude reaches 25.9% of the freestream velocity. Prior to mean separation, the TBL is highly accelerated from the prior FPG upstream of the bump (see Figures 4.2 and 4.9). As the pressure gradient become more adverse, the fluid near the surface reverses direction and lifts the boundary layer away. Throughout the separated region the velocity profile is highly inflectional. Even in the profile shown downstream of the reattachment, an outer inflection point in the mean velocity is evident. Mean separation occurs at  $x/L = 0.08$ , and the reattachment point occurs at  $x/L = 0.36$ . These measurements are in good agreement with the visual estimate provided by the flow visualization technique that highlighted surface streamlines in Section 4.3. At the centerline, the backflow region covers a streamwise distance of  $0.28L$ . In terms of the model height  $h$ , the backflow region covers  $2.9h$  on the centerline.

Another flow parameter obtained from the measurements and shown in Figure 4.19 was the vertical velocity component,  $V$ . At  $x/L \approx 0.05$ , just upstream of separation, the flow follows the contour of the bump and is shown by a negative  $V$  region. In the separated region, the fluid is moving up the bump surface, creating a positive vertical flow component. The turbulent normal stresses ( $\overline{u'u'}$  and  $\overline{v'v'}$ ) and shear stress ( $\overline{u'v'}$ ) were also averaged and plotted for the centerline case in Figure 4.19. A clear band of high turbulence originating near the point of separation is observed, with the streamwise component dominating the flow. Low freestream turbulence is maintained throughout the streamwise extent of the measurement window.

The same flow components shown in Figure 4.19 were measured at various spanwise planes, for the purpose of capturing the apparent three-dimensionality of the separated region. Figure 4.21 shows the mean velocity streamlines over the streamwise velocity field for each of the measurement planes at  $M_\infty$  with the bump in the A configuration. Furthest offspan at  $z/L = -0.250$ , no mean backflow was measured, and the streamlines follow the contour of the bump, straightening to parallel with increasing distance towards the freestream. Some of the instantaneous vector fields prior to averaging show very minor backflow at this location. Similarly, the  $z/L = -0.167$  location had some reversed fluid at discrete instances, with more regularity and magnitude than the  $z/L = -0.250$  plane. After averaging, however, the mean fields at this plane also did not exhibit mean flow reversal and the streamlines remain straight. Closer to the centerline, at  $z/L = -0.083$ , the prevalence of reversed flow exceeded that of forward flow, producing a time-averaged backflow shown by the rolling up of the streamlines centered near  $x/L = 0.23$ . The same features are also visible on the other side of the centerline at  $z/L = 0.083$ , where the streamlines show the fluid moving up the bump surface and pushed into the freestream flow through the shear layer. The centerline case at  $z/L = 0$  has the greatest magnitude of mean backflow velocity, which was highlighted in Figure 4.20.

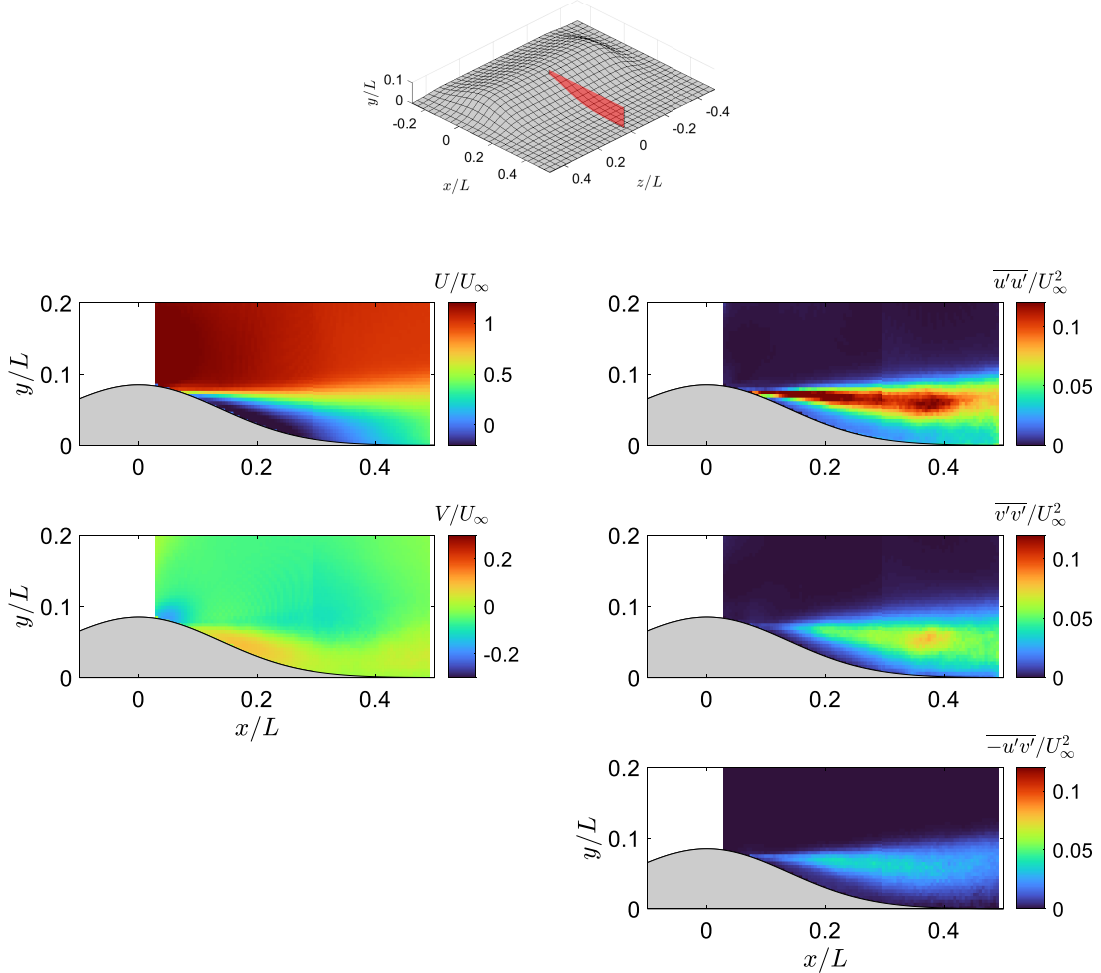


Figure 4.19. Centerline ( $z/L = 0$ ) Mean velocity and Reynolds stress components obtained using PIV downstream of the bump apex in configuration A at  $M_\infty = 0.2$ . The plane cut for which the PIV data is shown is illustrated over the bump surface on the top figure.

The spanwise distribution of the turbulence is shown in Figure 4.22. The two furthest offspan measurement planes have turbulence bands very close to the bump surface, which grow in magnitude and moves away from the surface as the distance to the mean backflow region is decreased. At  $z/L = \pm 0.083$ , where reversed flow is observed, the turbulence peaks increase greatly, and are located farther from the bump. At the centerline, the peak turbulence intensity is largest and located farthest from the bump surface, consistent with the largest extent of mean separated flow at this plane.

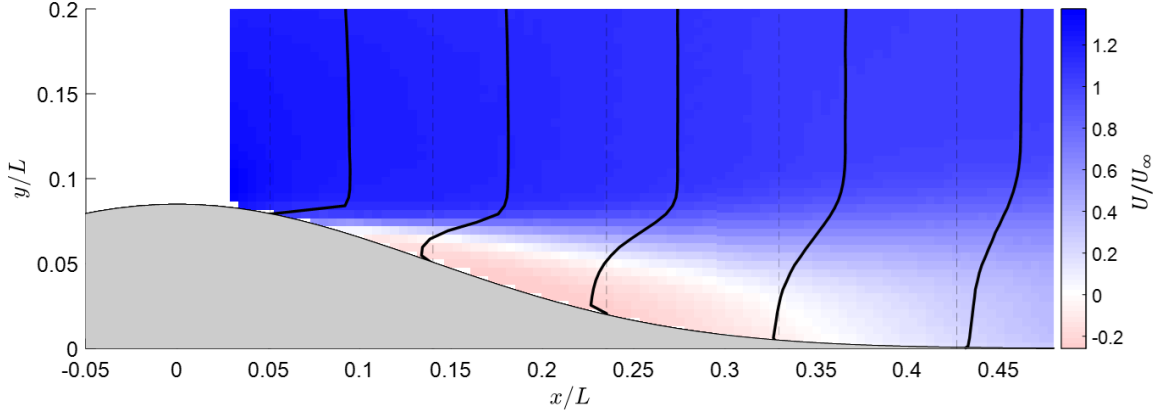


Figure 4.20. Mean streamwise velocity component obtained using PIV for the  $M_\infty = 0.2$  case at the centerline ( $z/L = 0$ ) for bump configuration A. Select vertical profiles are shown. The colormap shows flow moving in the downstream direction as blue, and the backflow region in red, and white indicates  $U = 0$ .

#### 4.7 SPIV Cross-Plane Flow Fields in Separation Region

Velocity data was acquired in the downstream region of the bump in measurement planes perpendicular to the streamwise direction using the SPIV system described in Section 2.4.6.1. The two camera setup provided fields of time-averaged three-component velocity and Reynolds turbulent stresses. Table 4.10 provides the cross-plane streamwise measurement locations at each of the freestream tunnel conditions. Each plane spanned from  $-0.13 < z/L < 0.13$  and from the bump surface to  $y/L \approx 0.1$ . Cross-planes were not investigated in the B configuration.

Figure 4.23 shows the flow quantities measured at the  $x/L = 0.250$  measurement plane at a freestream speed of  $M_\infty = 0.2$  in the A bump configuration. Mean velocity fields are in the left-most column. The SPIV cross-plane intersects with several of the two-component PIV planes taken parallel to the flow direction, and discussed in the previous section. The streamwise velocity follows the same spanwise distribution that was silhouetted in Figure 4.21, which showed fluid moving backward upstream and up the bump with the largest magnitude on the centerline. Farther offspan, the reversed flow becomes weaker and the fluid moves downward following the bump contours. Additionally, the SPIV measurements provide the spanwise velocity component field,  $W$ , which shows fast moving fluid traveling inward towards the centerline at the bump surface, and fluid traveling in the opposite direction farther from the bump surface. The SPIV measurements also captured the Reynolds normal and shear stresses, shown in the middle and right columns of Figure 4.23, respectively. The most significant source of turbulence is the streamwise normal stress,  $\overline{u'u'}$  which follows the same spanwise distribution as the  $\overline{u'v'}$  component (which is also silhouetted in Figure 4.22).

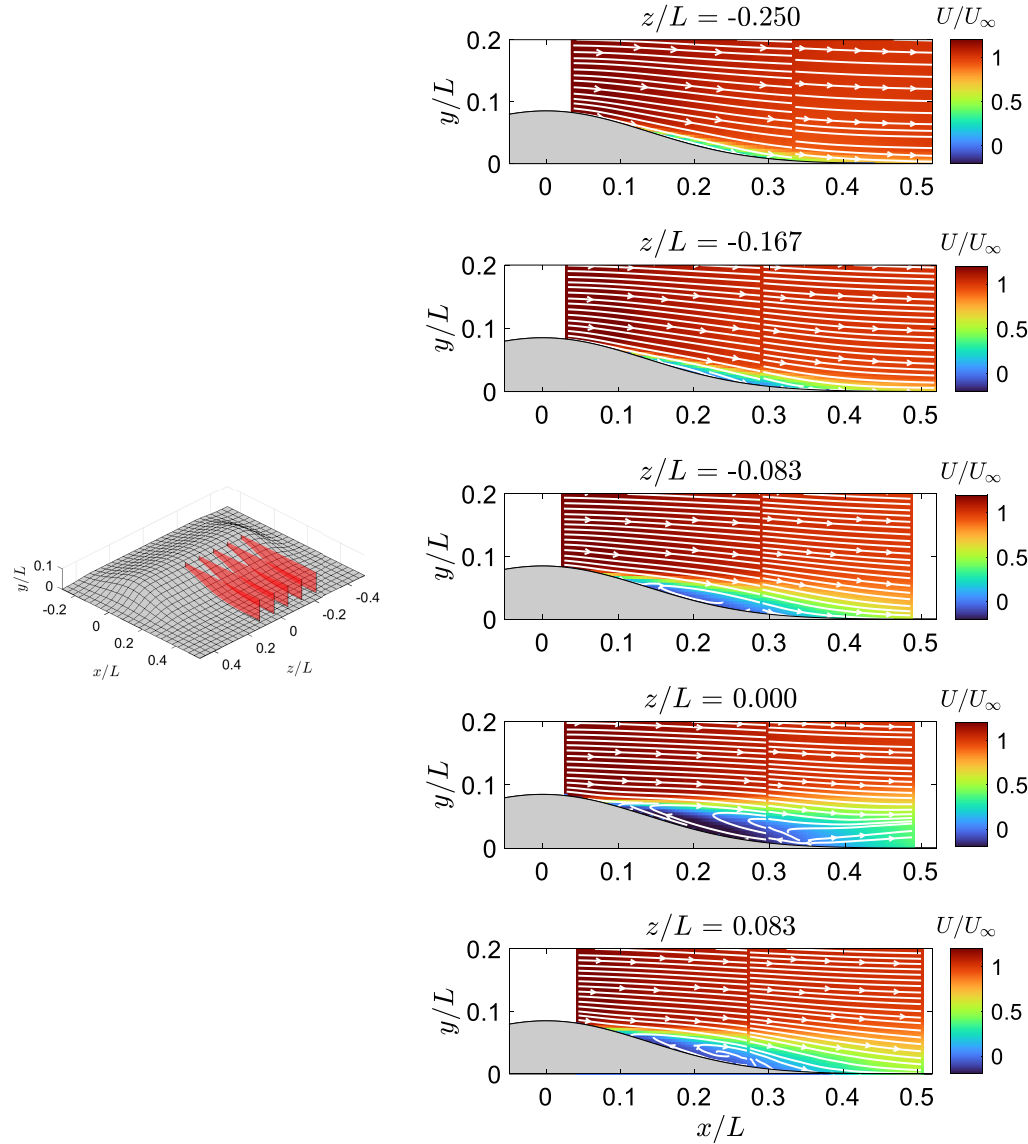


Figure 4.21. Spanwise distribution of mean velocity (colormap) and in-plane streamlines (white arrows) within the separation region measured with PIV at  $M_\infty = 0.2$  in bump configuration A. The plane cuts for which the PIV data are shown are illustrated over the bump surface on the left plot.

Here the turbulence peaks move toward the wall with increasing distance offspan, where the magnitude sharply declines for  $|z/L| > 0.1$ . The time-averaged shear stresses associated with spanwise fluctuations ( $\overline{v'w'}$  and  $\overline{u'w'}$ ) were also measured using the SPIV technique.

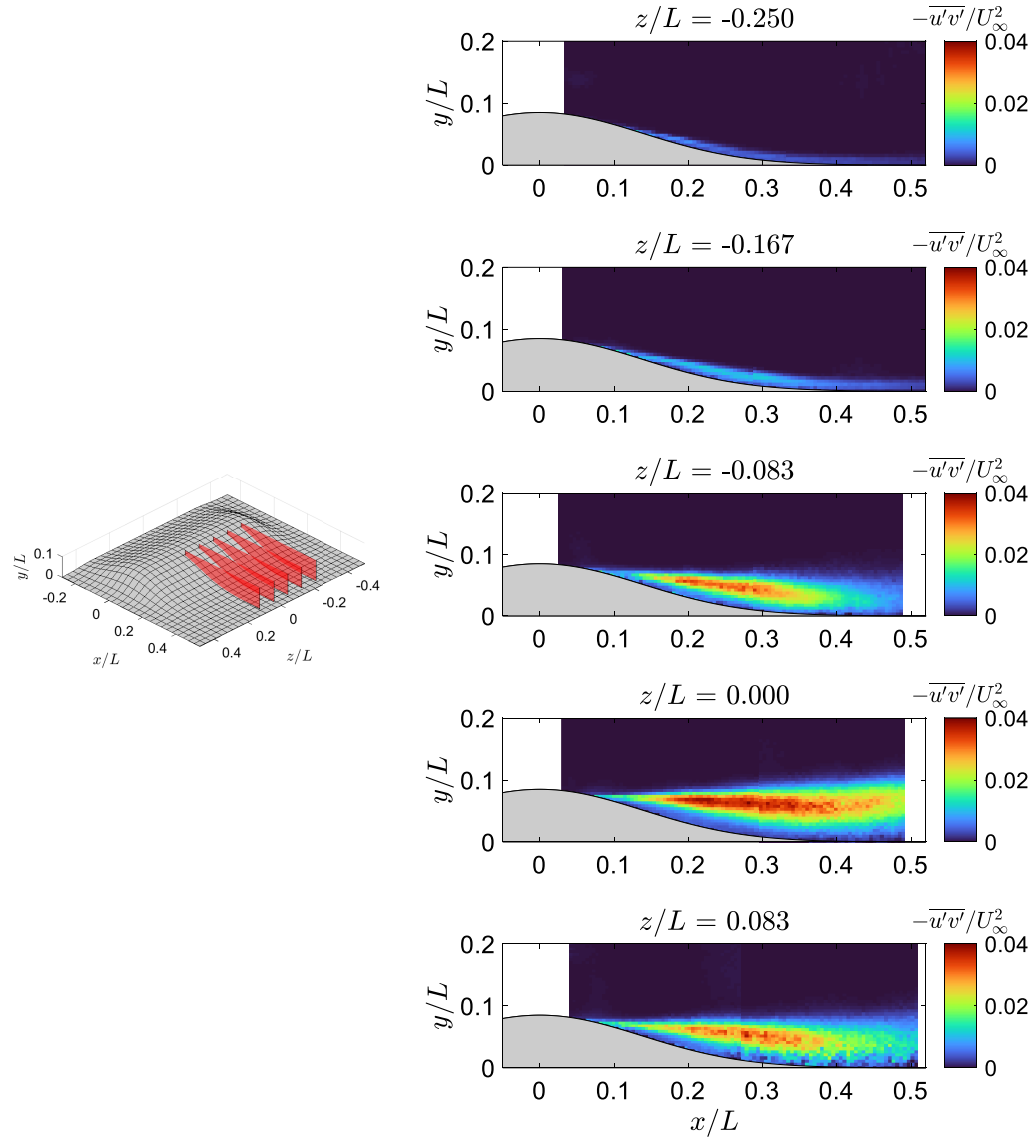


Figure 4.22. Spanwise distribution of turbulent shear stress within the separation region measured with PIV at  $M_\infty = 0.2$  in bump configuration A. The plane cuts for which the PIV data are shown are illustrated over the bump surface on the left plot.

Four cross-planes were investigated in the downstream region of the bump at each of the tunnel speeds. The time-averaged three-component flow fields obtained using SPIV were used to identify the topological evolution of the lifting vortices whose footprint at  $x/L \approx 0.14$  was identified using the oil based surface visualization technique (see Figure 4.8). Figure 4.24 shows how the flow field develops downstream of

TABLE 4.10

TUNNEL SPEEDS AND THE STREAMWISE LOCATIONS OF  
CROSS-PLANES INVESTIGATED USING SPIV.

$M_\infty$	$x/L = 0.208$	$0.250$	$0.306$	$0.361$
0.050	A	A	A	A
0.057	-	A	-	-
0.064	-	A	-	-
0.070	-	A	-	-
0.075	A	A	A	A
0.100	A	A	A	A
0.125	A	A	A	A
0.150	A	A	A	A
0.175	A	A	A	A
0.200	A	A	A	A

the bump at each SPIV cross-plane. The background color represents the streamwise component of the mean velocity field ( $U$ ) while the streamlines follow the direction of  $[W \ V]$ . The dotted black line denotes the  $U = 0$  streamsurface separating the reversed fluid from the downstream moving fluid. Beginning at the upstream most plane at  $x/L = 0.208$ , the counter-rotating vortices denoted as **F1** and **F2** in Figure 4.8 are captured well. Their foci are present in the cross-plane streamlines, confirming the claim that they lift away from the surface. Moving downstream to the  $x/L = 0.250$  plane, the separation bubble has contracted in the spanwise direction while maintaining its height. The foci that originated from the lifting vortices also moved closer together towards the centerline, and retain their vertical distance from the bump surface. The third streamwise plane located at  $x/L = 0.306$  was still located in the backflow region, but the bubble significantly decreased in spanwise length, and slightly in height. The two foci are no longer distinct in this plane, and have joined together into an off-plane node. This node persisted after reattachment in the final cross-plane at  $x/L = 0.361$ , where the mean streamwise velocity was measured to be positive everywhere.

The streamwise development of the turbulent shear stress component  $\overline{u'v'}$  is plotted in color contours for each streamwise cross-plane in Figure 4.25. The peak values begin in a narrow band in the upstream most plane. Moving downstream, the peak values take up more vertical distance and the offspan peaks bend closer to the sur-

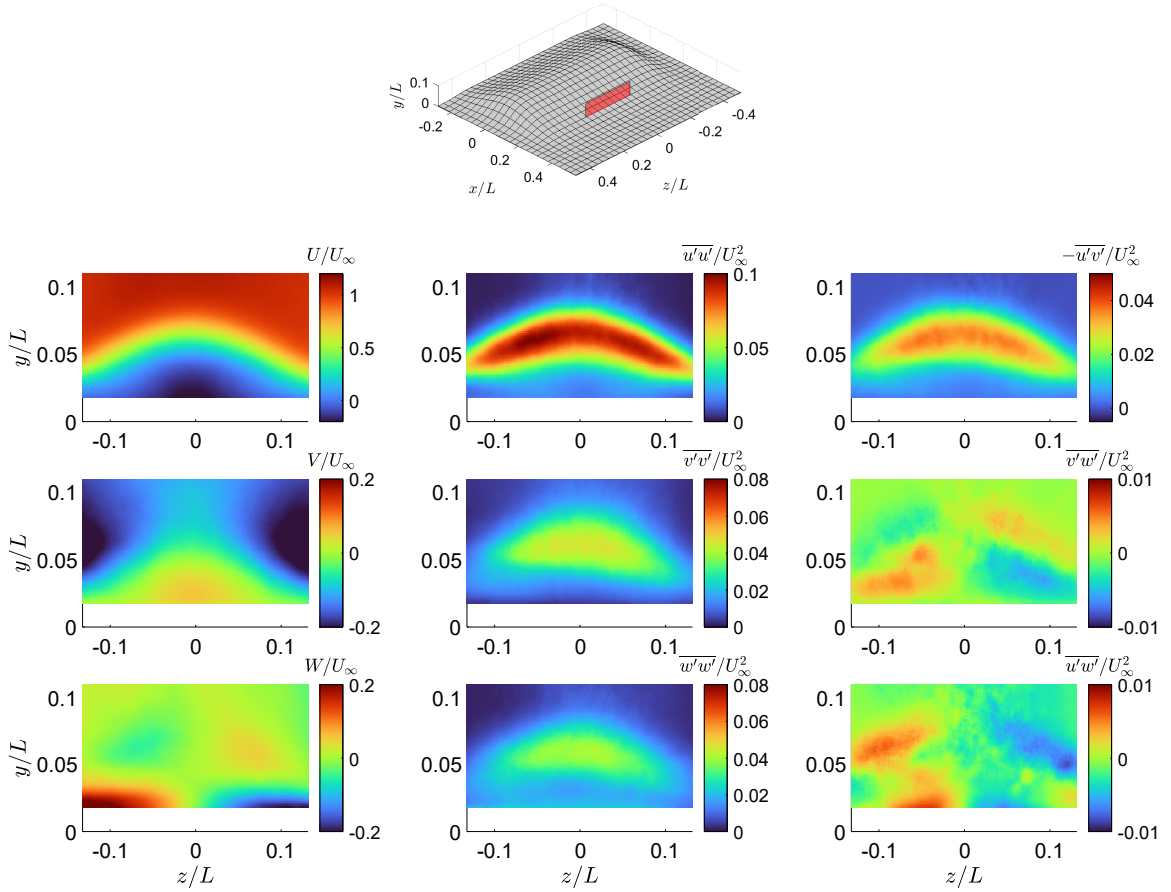


Figure 4.23. Mean velocity and Reynolds stress components obtained using SPIV downstream of the bump apex in a cross-plane located at  $x/L = 0.250$  at  $M_\infty = 0.2$  for bump configuration A. The cross-plane cut for which the SPIV data is shown is illustrated over the bump surface on the top plot.

face. The turbulence near the centerline retains its peak magnitude until it begins to decrease at the  $x/L = 0.361$  plane, where the mean flow is reattached.

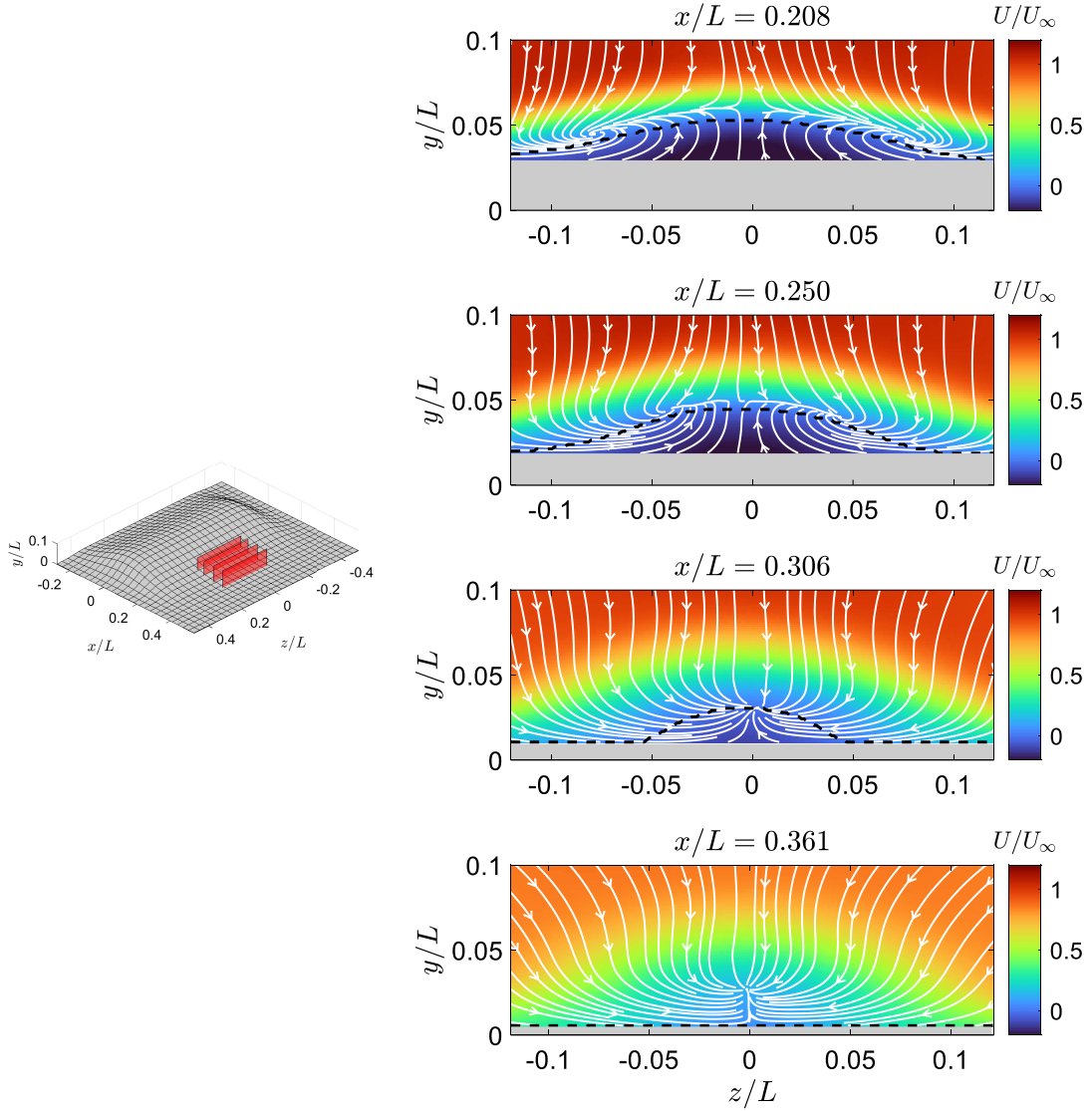


Figure 4.24. Streamwise distribution of the mean velocity (colormap) and the in-plane streamlines (white arrows in direction of [W V]) measured in several SPIV cross-planes at  $M_\infty = 0.2$  for bump configuration A. The dotted black line indicates  $U = 0$ . The cross-plane cuts for which the SPIV data are shown are illustrated over the bump surface on the left plot.

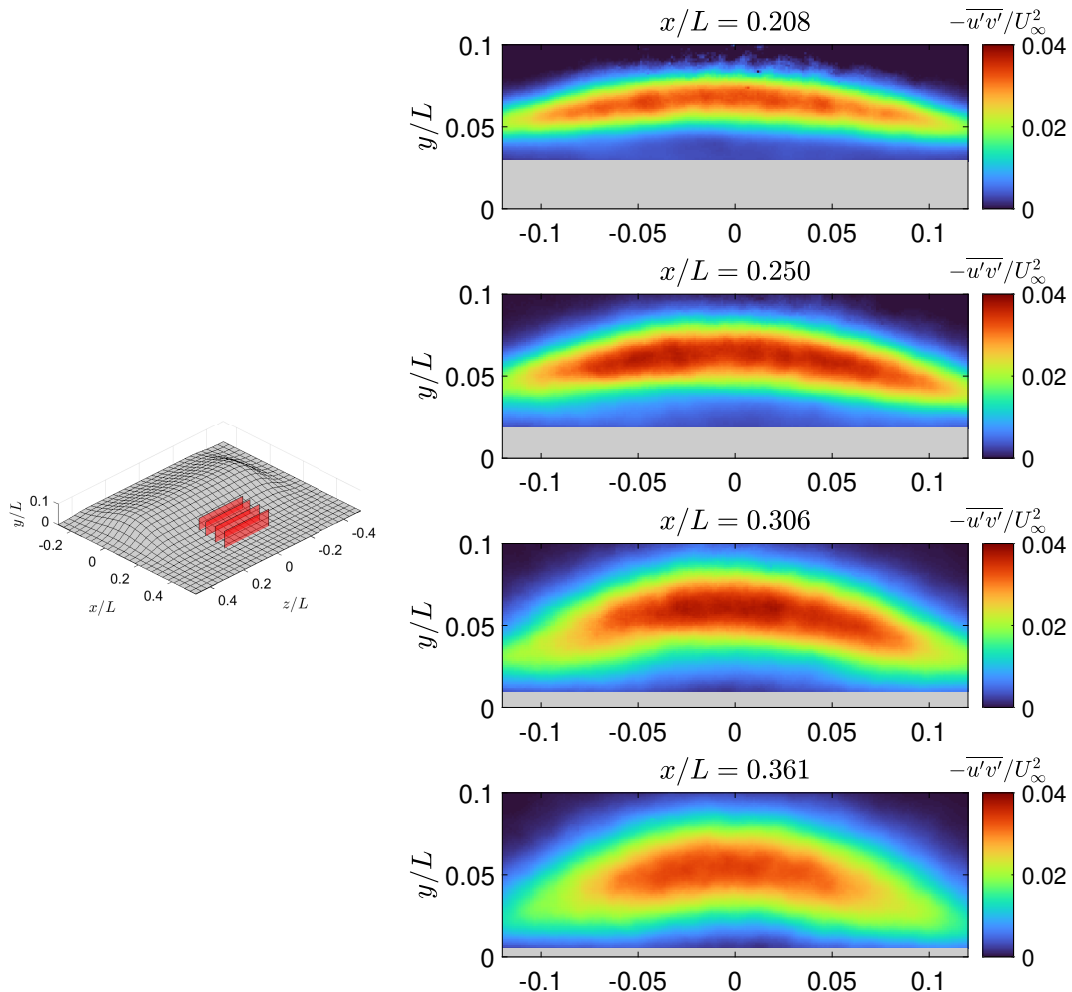


Figure 4.25. Streamwise distribution of the turbulent shear stress,  $-\overline{u'v'}$ , measured in several SPIV cross-planes at  $M_\infty = 0.2$  for bump configuration A. The cross-plane cuts for which the SPIV data are shown are illustrated over the bump surface on the left plot.

## CHAPTER 5

### SUMMARY AND RECOMMENDATIONS

The primary objective of the experimental work described in this report is to produce a series of benchmark data sets on smooth-body flow separation for CFD validation and further turbulence model development. The model geometry utilized in the experiments was designed to provide a well-defined and repeatable smooth-body flow separation case for both experimental work and complementary numerical simulations. Nicknamed the “Boeing Bump”, the geometry is a Gaussian profile in the streamwise,  $x$ , direction and has tapered shoulders using an error function in the spanwise,  $z$ , direction. These bump “shoulders” are designed to make the flow separation largely agnostic to the state of the wind tunnel side-wall boundary layers. The 3D bump geometry was mounted on a splitter plate model suspended in the test section that provides a well-defined origin for the incoming canonical turbulent boundary layer. Furthermore, by varying the streamwise location of the bump geometry on the splitter plate, the character of the incoming boundary layer upstream was systematically varied. The experimental work described in this report was done in partnership with the CFD group at Boeing who performed complementary numerical simulations on the Boeing bump geometry at conditions matching those in the experiments. That numerical work and the physical insights gleaned is described in a separate report.

The experiments were conducted over the freestream Mach number range of  $0.05 \leq M_\infty \leq 0.2$  corresponding to a range of Reynolds numbers (based on the spanwise dimension of the model,  $L = 0.914$  m) of  $1.0 \times 10^6 \leq Re_L \leq 4.0 \times 10^6$ . The majority of the reported measurements were performed at  $M_\infty = 0.2$  so that compressible CFD solvers may be validated without the need for low-speed preconditioning. This flow condition also matches that of the previous NASA Langley smooth body flow separation study on a 2D ramp geometry performed at Notre Dame, the results of which are now posted on the [NASA Turbulence Modeling Resource website](#). Similarly, the experimental results described in this report may be accessed at [https://turbmodels.larc.nasa.gov/Other\\_exp\\_Data/speedbump\\_sep\\_exp.html](https://turbmodels.larc.nasa.gov/Other_exp_Data/speedbump_sep_exp.html). Also available at this site in an extensive uncertainty analysis for all measured quantities.

The benchmark experiments described in this report were performed in the Notre Dame Mach 0.6 closed-circuit wind tunnel. This is a high Reynolds number, temperature controlled, low turbulence wind tunnel specifically designed for fundamental aerodynamic research. The tunnel air is driven by a 2.44 meter diameter, two-stage fan with variable pitch blades. It is powered by a 1750 hp variable r.p.m. AC motor. The wind tunnel utilizes a unique active air temperature control system to maintain a

constant, spatially uniform, free-stream temperature. Turbulence management provides a very low freestream turbulence intensity level throughout the Mach number range of the tunnel,  $\sqrt{\overline{u'^2}}/U_\infty \leq 0.05\%$  which is a unique feature of the Notre Dame facility. One of three removable test sections was dedicated solely for the reported experimental work. The square test section of width  $L = 0.914$  m (3.0 ft) extends 2.743 m (9.0 ft) in the streamwise direction.

Prior to installation of the model geometry, a complete characterization of the empty wind tunnel test section was performed. The results of these measurements are included in the archival data set and serve to document tunnel flow spatial uniformity, flow angularity, freestream turbulence levels and degree of isotropy as well as empty tunnel sidewall turbulent boundary layer mean velocity profiles.

The archival data set also includes a complete set of measurements obtained with the splitter plate and associated fixtures installed in the test section without the bump. These experiments insured proper setting of the trailing flap so that no flow separation was present near the plate leading edge and also provides documentation of canonical zero pressure gradient turbulent boundary layer streamwise development on the plate. The boundary layer development on the splitter plate and tunnel side walls was measured using a traversing hot-wire anemometry system. These data include mean velocity profiles at multiple streamwise and spanwise locations on the plate as well as the tunnel side walls. The Clauser method was utilized to obtain local skin friction coefficients used for inner variable mean velocity profile scaling.

With the Boeing bump geometry installed on the splitter plate, two bump configurations were tested for the majority of the experiments reported in this study. Configuration A denotes the case when the bump apex was installed at a streamwise distance of  $X = X_{apex} = L$  from the inlet. The notation  $X_{apex}$  is used to describe the streamwise location of the bump apex position. Configuration B denotes the case where the apex was located at  $X_{apex} = 2L$  from the leading edge. For both of these configurations, the streamwise evolution of the incoming turbulent boundary layer on the splitter plate and tunnel sidewalls was again documented with hot-wire anemometry and the local skin friction with oil-film interferometry (OFI). These data are included for several freestream Mach numbers. In addition, the data set includes a series of comprehensive stereoscopic particle image velocimetry (SPIV) measurements of the mean velocity and turbulence statistics for the flow both approaching and interacting with the upstream side of the bump. The freestream tunnel speeds for which data is available using each of the diagnostic techniques can be found in tables 4.1 and 4.2.

The data set documenting the flow separation and reattachment on the bump include fluorescent surface oil flow visualization images obtained over a range of approach Mach numbers. These clearly show the surface flow separation and reattachment topography exhibits a generic “owl face pattern of the first kind”. Surface static pressure measurements were obtained at multiple streamwise and spanwise locations on the bump for a range of approach Mach numbers. These mean static surface pressure measurements are complemented by a series of dynamic pressure measurements obtained at selected locations via multiple Kulite dynamic pressure

sensors. The skin friction coefficient development over the centerline of the bump was measured directly using a novel photogrammetric OFI method developed during the course of this study. These OFI data were obtained for approach Mach numbers of 0.05, 0.1 and 0.2.

Planar PIV was utilized in order to document the bump flow and reattachment. These data sets were acquired at five spanwise locations on the downstream side of the bump. These measurement planes were located at  $z/L = -0.250, -0.167, -0.083, 0.000$ , and  $0.083$ . At each spanwise location, the stitched data gave a measurement field extending from  $x/L \approx 0.03$  to  $0.50$  in the streamwise direction, and vertically from the bump surface to  $y/L \approx 0.2$ . The two-component PIV setup provided time-averaged velocity fields of the mean velocity and turbulence statistics.

Stereoscopic PIV (SPIV) data was also acquired in the downstream region of the bump in multiple measurement planes perpendicular to the streamwise direction. Measured from the bump apex, these streamwise locations were  $x/L = 0.208, 0.250, 0.306$ , and  $0.361$ . These measurement planes spanned from  $z/L = \pm 0.131$ , and vertically from the bump surface to  $y/L = 0.11$ . The two camera SPIV setup provided fields of time-averaged three-component velocity and Reynolds turbulent stresses to more fully characterize the nature of the flow separation.

In summary, an extensive validation quality data set has been obtained that characterizes the smooth body flow separation from the Boeing bump geometry and its subsequent reattachment for the incompressible flow regime. The question remains how the character of this smooth body flow separation would change due to compressibility effects. The Notre Dame wind tunnel facility provides the unique capability of extending the acquired Boeing bump data set up to compressible Mach numbers of  $M_\infty = 0.6$ . This would provide for the documentation of the effects of compressibility in the archival data set as well as enable an examination of how scaling of the mean flow and turbulence quantities is influenced. It is highly recommended that the data set be expanded so as to include measurements at subsonic compressible Mach numbers.

It is well known that smooth body flow separation is influenced not only by the imposed adverse pressure gradient but also by surface curvature. Indeed, this is the case for both the NASA Langley smooth body flow experiment performed previously as well as for the Boeing bump geometry experiments documented here. A modification of the current experimental configuration provides an opportunity to separate the effects of wall curvature and imposed pressure gradient. One approach would involve repeating key measurements in the current data set with the splitter plate and Boeing bump model placed at different distances from the wind tunnel ceiling. In this manner, the imposed pressure gradient is systematically modified while the surface curvature is held fixed. Alternately, and perhaps more effectively, a contoured tunnel ceiling matching the Boeing bump contour and placed above the model would reduce the streamwise pressure gradient over the model, so that the streamwise flow evolution would be governed primarily by surface curvature effects. Experiments such as these would provide the unique opportunity to develop a surface curvature parameter for inclusion in smooth body flow separation modeling.

## APPENDIX A

### SPLITTER PLATE AND BUMP INSTALLATION

The bump section consisted of two pieces of 5000 series cast aluminum that were fabricated in a three-axis computer numerically controlled (CNC) machine. The streamwise extent of the bump section was 1016 mm, so that a distance of 508 mm was reached on both sides, amounting to a maximum bump height of  $y_b(\pm 508 \text{ mm}, z) = 0.023 \text{ mm}$  (0.0009 in). This was considered hydrodynamically smooth for boundary layer thicknesses in the current study. The two halves were asymmetric, spanning 483 mm and 432 mm, respectively (the bumps were joined in the  $z/L = -0.028$  plane, or 1.0 in off the centerline. Figure A.1 shows the CAD geometry of the bump halves, and how they were joined together so that the bump surface was flush and the seam was minimized after installation. Stainless steel dowel pins with a 6.35 mm diameter were used to align the sections with  $\pm 0.25 \text{ mm}$  precision. Several hex bolt and nut configuration on the underside of the plates were used to fix the section halves together, and pull the gap tight.



Figure A.1. Top and bottom views of the bump section halves.

The bump section sat flush with the rest of the splitter plate sections, which spanned the full 914 mm of the test section and were made of 12.7 mm (0.5 in) thick aluminum. The streamwise length of each of the plate sections was 508 mm

(20 in), and could be arranged to adjust the streamwise position the bump section. In addition to the plate sections, a 101.6 mm (4 in) spacing plate was fabricated so that the streamwise positions of the bump apex could be precisely  $L$  and  $2L$  from the leading edge, corresponding to configurations A and B, respectively. The leading edge section, which was machined with a 4:1 elliptical leading edge tip, spanned 304.8 mm (12 in) in the streamwise direction. The trailing edge flap assembly, shown in Figure A.2, consisted of a 203.2 mm (8 in) plate and a 101.6 mm (4 in) long flap that symmetrically tapers to a 0.53 mm tip at a  $3.28^\circ$  angle. The two pieces of the trailing edge assembly are connected using a hinge joint that which is tightened with rubber o-rings and bolts.

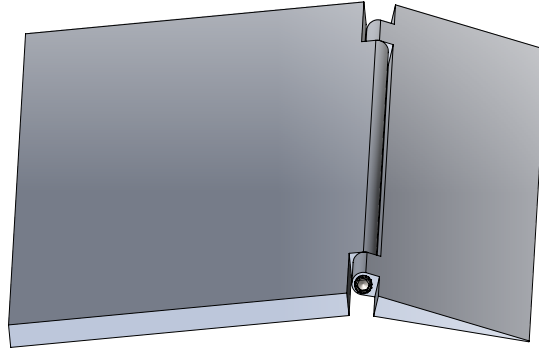


Figure A.2. Trailing edge flap assembly.

The plate sections were aligned vertically and spanwise using stainless steel dowel pins with a 6.35 mm diameter. Plate connectors fixed to the underside of each of the plate sections served to pull each of the plates tightly together, and also to fix the plates onto the suspended L-beams on which they rested. Tie plates were also used to vertically align the plates, and reduce any fatigue sagging caused by the prolonged two point bending. A photograph of the splitter plate from the underside half of the test section looking downstream is provided in Figure A.3, showing the plate connectors and tie plates that are used to fix the plates together and onto the L-beams.

Measurements were made to document the vertical alignment and levelness of the splitter plate. The top of the splitter plate was nominally set half way between the top and bottom walls of the test section ( $L/2$ ). Fine adjustments were made

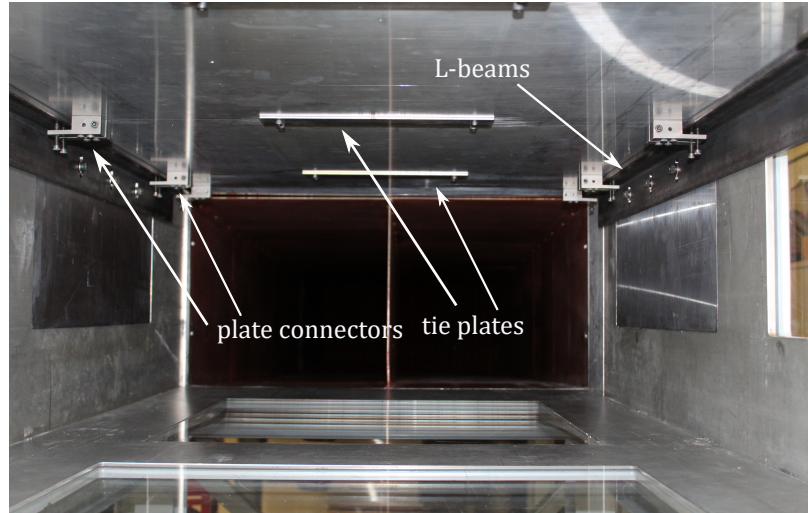


Figure A.3. Photograph underneath the splitter plate, the connecting fixtures are highlighted.

to maximize the levelness of the splitter plate. Twelve measurements were made at various positions streamwise and spanwise positions from the top wall of the test section to the top of the splitter plate. Measurements were made using a Starrett Solid-Rod Long Range Micrometer with a 0.25 mm (0.001 in) accuracy. Table A.1 gives the location of the measurements in the global coordinate system (see Section 2.3), and the difference from the nominal vertical location.

TABLE A.1

VERTICAL PLATE ALIGNMENT IN THE TEST SECTION.

Point #	X [mm]	Z [mm]	$\Delta Y$ [mm]
1	51	-432	0.94
2	51	0	0.28
3	51	432	0.89
4	686	-432	0.36
5	686	431	1.35
6	1372	-432	-0.03
7	1372	432	0.91
8	2057	-432	0.53
9	2057	432	0.94
10	2591	-432	1.17
11	2591	0	0.20
12	2591	432	0.46

## APPENDIX B

### OFI CALIBRATION AND PROCEDURE

The OFI procedure steps, as described by Gluzman et al. [1], are as follows:

- 1. Estimate Camera Parameters (Calibration).**
  - i. Detect a checkerboard pattern in a set of input images.
  - ii. Generate the *world coordinates* of the checkerboard corners.
  - iii. Set local  $x'$ - $z'$  coordinate system with the upper-left corner at (0,0).
  - iv. Estimate intrinsic and extrinsic parameters and the distortion coefficients.
  - v. Evaluate standard estimation errors for the single camera calibration.
- 2. Select single image.**
  - i. Remove lens distortion from the image.
  - ii. Detect the checkerboard in the selected underscored image.
  - iii. Compute rotation and translation of the camera with respect to the checkerboard in that image.
- 3. Select localized area in the fringe pattern in the image.**
  - i. Segment fringes and compute their average spacing  $\Delta x_f$  in that area.
  - ii. Compute the camera refraction angle  $\theta_r$  to the center of the fringe area.

In the first and second steps above, a set of multiple images (at least 3) of a calibration pattern was obtained from different angles. The calibration pattern used was asymmetric, containing an even number of squares along one side, and odd number of squares along the other. The size of a square was measured in world units as precisely as possible. The asymmetric checkerboard provided a local  $x'$ - $z'$  coordinate system with the upper-left corner at (0,0) in the detected checkerboard pattern, where  $x'$  is the direction along the long side, and  $z'$  is direction along the short side, as shown on the checkerboard in Figure 2.13.

Camera calibration estimated the values of the intrinsic parameters, the extrinsic parameters, and the distortion coefficients. The extrinsic parameters represent a rigid transformation from the 3D world coordinate system to the 3D camera's coordinate system. The intrinsic parameters represent a projective transformation from the

3D camera's coordinates into the 2D image coordinates. The calibration algorithm assumes a pinhole camera model, where the following system is solved

$$w \begin{bmatrix} x_i & y_i & 1 \end{bmatrix} = \begin{bmatrix} x' & y' & z' & 1 \end{bmatrix} \begin{bmatrix} \mathbf{R} \\ \mathbf{t} \end{bmatrix} \mathbf{K}. \quad (\text{B.1})$$

Here,  $(x', y', z')$  are the *world coordinates* (metric units, like the one defined in Figure 2.13) of a point;  $(x_i, y_i)$  coordinates (pixel plane of the image) of the corresponding image point;  $w$ : arbitrary scale factor. The world points are transformed to camera coordinates using the extrinsic parameters consisting of  $\mathbf{R}$ , the 3D rotation matrix of the camera and  $\mathbf{t}$ , the translation of the camera relative to the world coordinate system. The camera coordinates are mapped into the image plane using the intrinsic parameters within camera intrinsic matrix  $\mathbf{K}$  that is defined as:

$$\mathbf{K} = \begin{bmatrix} f_x & 0 & 0 \\ s & f_y & 0 \\ c_x & c_y & 1 \end{bmatrix}, \quad (\text{B.2})$$

where  $[c_x \ c_y]$  is the optical center (the principal point), in pixels;  $(f_x \ f_y)$  is the focal length in pixels; and  $s$  is the skew coefficient.

The system in Equation B.1 does not account for lens distortion because an ideal pinhole camera does not have a lens. However, the camera model should also include the radial and tangential lens distortion to represent a real camera accurately. Radial distortion occurs when light rays bend more near the edges of a lens than they do at its optical center. The smaller the lens, the greater the distortion. Whereas tangential distortion occurs when the lens and the image plane are not parallel. A number of radial distortion coefficients and tangential distortion coefficients can be defined and then estimated for calibration. For more details on these distortions, see [70]. Therefore, two steps were involved in camera calibration to account for these types of distortion. First, the system in Equation B.1 was solved for the intrinsics and extrinsics in closed form, assuming that lens distortion is zero [71]. Then, all parameters were estimated simultaneously, including the distortion coefficients using nonlinear least-squares minimization (Levenberg–Marquardt algorithm) [71, 72]. These steps were employed in this study by using built-in MATLAB calibration algorithms, which can also provide the calibration accuracy. In the case of applying the checkerboard on a curved surface, the calibration procedure assumes that the checkerboard is as flat as possible. This is exploited for obtaining the camera angle to the surface accurately for any curvature. The idea is that mounting the flexible checkerboard firmly to the surface would deform the checkerboard. Therefore, the algorithm would associate this deformation to camera intrinsics and lens distortion. The algorithm would yield an undistorted image in an attempt to flatten the checkerboard and thus unfold the curved surface. This unfolded surface would allow obtaining the correct distances between the fringes  $\Delta x_f$  along with the arc distance of the surface and evaluate the angle  $\theta_r$  correctly with respect to the unfolded surface normal. This process is illustrated in Figure B.1a and Figure B.1b for placing the checkerboard over the bump

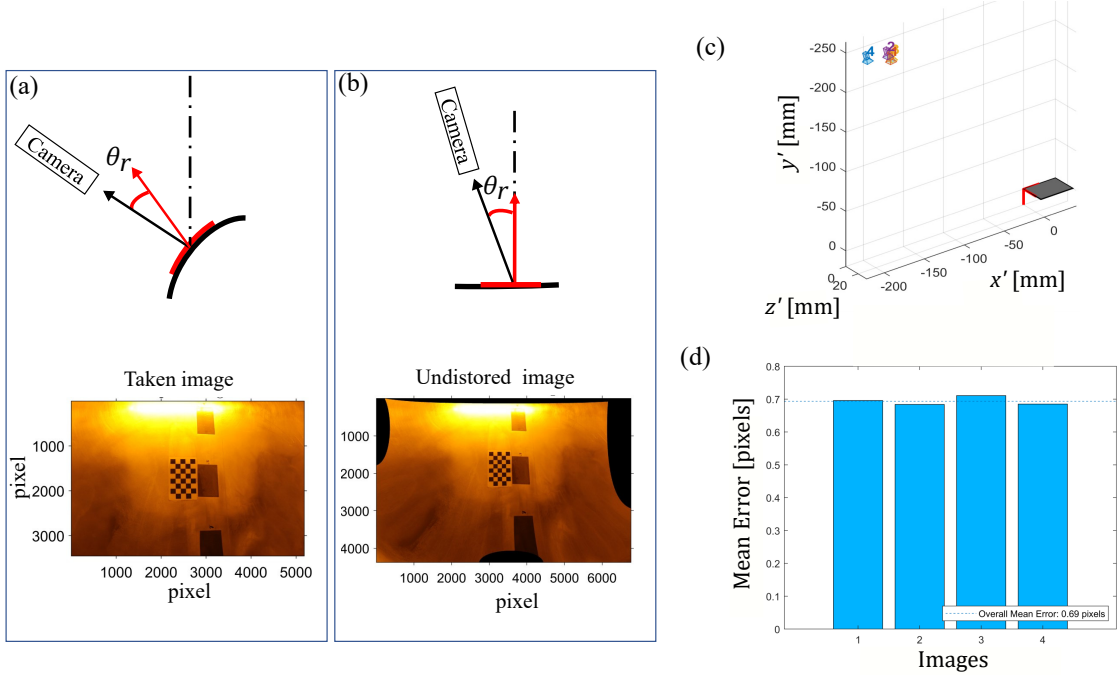


Figure B.1. Undistorting image process for a checkerboard over a curved surface: a) the camera angle with respect to the deformed checkerboard (red curve) mounted on the curved surface (black curve). b) The process of calibration deforms the image to flatten the checkerboard. c) Extrinsic parameters visualization, where the camera for each image is projected in space relative to the local origin of the calibration board. d) Mean projected error per image. Reproduced from Fig. 6 of Gluzman et al. [1].

near Kapton strip number 14, which location is shown in Figure 2.12. In this case, a checkerboard with a square size of 7.75 mm is used, and four images are obtained. The obtained extrinsic parameters are shown in Figure B.1c and their corresponding error in Figure B.1d. The calibration process preference is not deteriorated due to the surface curvature.

After completing the first two steps—image calibration and undistorting the selected image—a third step was performed. In this step, a fringe interrogation region was selected based on quality of fringes. The angle to the center of the fringe region rectangle ( $\theta_r$ ) was computed and the fringe spacing was evaluated via segmentation. The average skin friction would then be obtained over the selected area. Therefore, the smaller the area, the more localized skin friction is measured; however, the area needed to be large enough that at least two fringes were captured. The fringes were segmented in the selected rectangle to evaluate the fringe spacing. This was done by converting the image to HSV (hue, saturation, value) color space and getting

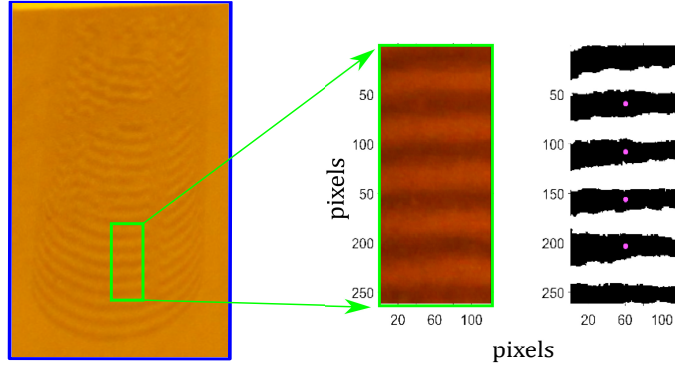


Figure B.2. Undistorted image of OFI application from Kapton strip 6 (see Figure 2.12). The selected rectangle was converted to into HSV space and a threshold function was used to identify the fringe centers for each pixel column (the pink dots represent the fringe centers averaged across the span). Reproduced from Fig. 7a of Gluzman et al. [1].

a saturation channel. Then a threshold, using *graythresh* function in Matlab that employs Otsu's method [73], is set in order to produce a binary fringe pattern. The process is illustrated in Figure B.2 for the fringe pattern highlighted in Figure 2.13. To increase the accuracy of the fringe spacing evaluation, the distance between the fringes for each column of pixels in the rectangle were evaluated and averaged. More fringes along the span would yield more data to be averaged, thus, reducing the error.

## APPENDIX C

### STATIC PRESSURE TAP LOCATIONS

This appendix contains the locations of the static pressure ports, as shown in Figure C.1. The coordinates for each tap are given for the centers of each hole on the bump surface.

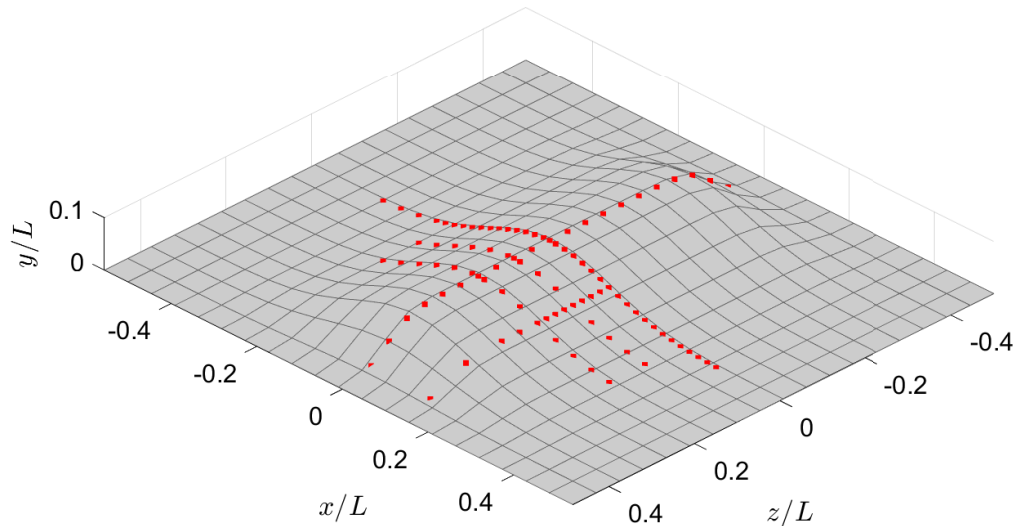


Figure C.1. Static pressure port locations on the instrumented bump.

TABLE C.1

LOCATIONS OF STATIC PRESSURE TAPS ALONG THREE  
DIFFERENT STREAMWISE AXES ( $z/L = 0$ , 0.0833, & 0.1667).

CENTERLINE			OFFSPAN		
$x/L$	$y/L$	$z/L$	$x/L$	$y/L$	$z/L$
-0.3889	0.0016	0.0000	-0.2222	0.0232	0.0833
-0.3472	0.0036	0.0000	-0.1806	0.0361	0.0833
-0.3056	0.0073	0.0000	-0.1378	0.0516	0.0833
-0.2639	0.0136	0.0000	-0.0972	0.0663	0.0833
-0.2431	0.0180	0.0000	-0.0556	0.0784	0.0833
-0.2222	0.0232	0.0000	-0.0139	0.0846	0.0833
-0.2014	0.0293	0.0000	0.0000	0.0850	0.0833
-0.1806	0.0361	0.0000	0.0139	0.0846	0.0833
-0.1597	0.0435	0.0000	0.0556	0.0784	0.0833
-0.1378	0.0516	0.0000	0.0972	0.0663	0.0833
-0.1181	0.0589	0.0000	0.1378	0.0516	0.0833
-0.0972	0.0663	0.0000	0.1806	0.0361	0.0833
-0.0764	0.0729	0.0000	0.2222	0.0232	0.0833
-0.0556	0.0784	0.0000	0.2639	0.0136	0.0833
-0.0347	0.0823	0.0000	0.3056	0.0073	0.0833
-0.0139	0.0846	0.0000	-0.2222	0.0232	0.1667
0.0000	0.0850	0.0000	-0.1806	0.0361	0.1667
0.0139	0.0846	0.0000	-0.1378	0.0516	0.1667
0.0347	0.0823	0.0000	-0.0972	0.0663	0.1667
0.0556	0.0784	0.0000	-0.0556	0.0784	0.1667
0.0764	0.0729	0.0000	-0.0139	0.0846	0.1667
0.0972	0.0663	0.0000	0.0000	0.0850	0.1667
0.1181	0.0589	0.0000	0.0139	0.0846	0.1667
0.1378	0.0516	0.0000	0.0556	0.0784	0.1667
0.1597	0.0435	0.0000	0.0972	0.0663	0.1667
0.1806	0.0361	0.0000	0.1378	0.0516	0.1667
0.2014	0.0293	0.0000	0.1806	0.0361	0.1667
0.2222	0.0232	0.0000	0.2222	0.0232	0.1667
0.2431	0.0180	0.0000	0.2639	0.0136	0.1667
0.2639	0.0136	0.0000	0.3056	0.0073	0.1667
0.2847	0.0101	0.0000			
0.3056	0.0073	0.0000			
0.3264	0.0052	0.0000			
0.3472	0.0036	0.0000			
0.3681	0.0024	0.0000			
0.3889	0.0016	0.0000			

TABLE C.2

LOCATIONS OF STATIC PRESSURE TAPS ALONG TWO  
DIFFERENT SPANWISE AXES ( $x/L = 0$  &  $0.1379$ ).

BUMP APEX			INFLECTION PT.		
$x/L$	$y/L$	$z/L$	$x/L$	$y/L$	$z/L$
0.0000	0.0165	-0.4167	0.1379	0.0516	0.0000
0.0000	0.0465	-0.3750	0.1379	0.0516	0.0208
0.0000	0.0735	-0.3333	0.1379	0.0516	0.0417
0.0000	0.0834	-0.2917	0.1379	0.0516	0.0625
0.0000	0.0849	-0.2500	0.1379	0.0516	0.0833
0.0000	0.0850	-0.2083	0.1379	0.0516	0.1042
0.0000	0.0850	-0.1667	0.1379	0.0516	0.1250
0.0000	0.0850	-0.1250	0.1379	0.0516	0.1458
0.0000	0.0850	-0.0833	0.1379	0.0516	0.1667
0.0000	0.0850	-0.0417	0.1379	0.0516	0.2083
0.0000	0.0850	0.0000	0.1379	0.0515	0.2500
0.0000	0.0850	0.0417	0.1379	0.0446	0.3333
0.0000	0.0850	0.0833	0.1379	0.0100	0.4167
0.0000	0.0850	0.1250			
0.0000	0.0850	0.1667			
0.0000	0.0850	0.2083			
0.0000	0.0849	0.2500			
0.0000	0.0834	0.2917			
0.0000	0.0735	0.3333			
0.0000	0.0465	0.3750			
0.0000	0.0165	0.4167			

## APPENDIX D

### UNCERTAINTY ANALYSIS

#### D.1 Freestream Conditions

The total standard uncertainty  $\varepsilon_U$  in the measurement of the streamwise velocity  $U$  is a combination of random standard uncertainty  $s_U$  and systematic standard uncertainty  $b_U$ :

$$\varepsilon_U = \sqrt{s_U^2 + b_U^2} \quad (\text{D.1})$$

Similarly, the total standard uncertainty  $\varepsilon_M$  in the measurement of the Mach number  $M$  is a combination of random uncertainty  $s_M$  and systematic uncertainty  $b_M$ :

$$\varepsilon_M = \sqrt{s_M^2 + b_M^2} \quad (\text{D.2})$$

Equation 2.2 expresses the velocity as a function of density and differential pressure. Combining Equations 2.5 gives an expression for  $M$  as a function of differential pressure, density, and temperature:

$$M = f(\Delta P, \rho, T) = \sqrt{\frac{2\Delta P}{\rho\gamma RT}}. \quad (\text{D.3})$$

The sensitivities of  $M$  with respect to each of these quantities can then be obtained by partial differentiation as:

$$\frac{\partial M}{\partial \Delta P} = \sqrt{\frac{1}{2\Delta P \rho \gamma RT}}, \quad (\text{D.4})$$

$$\frac{\partial M}{\partial \rho} = -\sqrt{\frac{\Delta P}{2\rho^3 \gamma RT}}, \text{ and} \quad (\text{D.5})$$

$$\frac{\partial M}{\partial T} = -\sqrt{\frac{\Delta P}{2\rho\gamma RT^3}}. \quad (\text{D.6})$$

Likewise, the sensitivities of  $U$  with respect to each of its functional quantities can be expressed via partial differentiation as:

$$\frac{\partial U}{\partial \Delta P} = \sqrt{\frac{1}{2\Delta P \rho}}, \text{ and} \quad (\text{D.7})$$

$$\frac{\partial U}{\partial \rho} = -\sqrt{\frac{\Delta P}{2\rho^3}}. \quad (\text{D.8})$$

The random uncertainty for  $U$  and  $M$ , respectively, can then be expressed as:

$$s_U = \sqrt{\left(\frac{\partial U}{\partial \Delta P} s_P\right)^2 + \left(\frac{\partial U}{\partial \rho} s_\rho\right)^2}, \quad (\text{D.9})$$

$$s_M = \sqrt{\left(\frac{\partial M}{\partial \Delta P} s_P\right)^2 + \left(\frac{\partial M}{\partial \rho} s_\rho\right)^2 + \left(\frac{\partial M}{\partial T} s_T\right)^2}, \text{ and} \quad (\text{D.10})$$

where  $s_P$ ,  $s_\rho$ , and  $s_T$  are the random standard uncertainty values for pressure, density, and temperature, respectively. These values are estimator variances normalized by the number of samples  $N$ , and are defined as:

$$s_P = \sqrt{\frac{\frac{1}{N-1} \sum_{i=1}^N (P_i - \bar{P})^2}{N}}, \quad (\text{D.11})$$

$$s_\rho = \sqrt{\frac{\frac{1}{N-1} \sum_{i=1}^N (\rho_i - \bar{\rho})^2}{N}}, \quad (\text{D.12})$$

$$s_T = \sqrt{\frac{\frac{1}{N-1} \sum_{i=1}^N (T_i - \bar{T})^2}{N}}, \text{ and} \quad (\text{D.13})$$

where  $P_i$ ,  $\rho_i$ , and  $T_i$  are the instantaneous pressure, density, and temperature values, respectively.

Similarly, the systematic uncertainty values are given by:

$$b_U = \sqrt{\left(\frac{1}{k_P} \frac{\partial U}{\partial \Delta P} b_P\right)^2 + \left(\frac{1}{k_\rho} \frac{\partial U}{\partial \rho} b_\rho\right)^2}, \text{ and} \quad (\text{D.14})$$

$$b_M = \sqrt{\left(\frac{1}{k_P} \frac{\partial M}{\partial \Delta P} b_P\right)^2 + \left(\frac{1}{k_\rho} \frac{\partial M}{\partial \rho} b_\rho\right)^2 + \left(\frac{1}{k_T} \frac{\partial M}{\partial T} b_T\right)^2}, \quad (\text{D.15})$$

where  $k_P$ ,  $k_\rho$ , and  $k_T$  are the coverage factors for differential pressure, density, and temperature, respectively, each taken to be  $\sqrt{3}$ . These values are related to the measurement confidence intervals via the relationship presented in Table D.1. The systematic uncertainty  $b_\rho$  of the density was estimated as

$$b_\rho = \frac{|\rho_{start} - \rho_{end}|}{2}. \quad (\text{D.16})$$

Here,  $\rho_{start}$  and  $\rho_{end}$  are the density values calculated at the beginning and end of the run. The systematic uncertainty  $b_T$  of the temperature was estimated as a combination of measured temperature difference across the run and instrument

TABLE D.1  
CONFIDENCE INTERVALS FOR VARIOUS COVERAGE FACTOR  
VALUES.

k	Confidence [%]
1	68
1.96	95
2.58	99
3	> 99

uncertainty in the thermocouple:

$$b_T = \sqrt{\left(\frac{T_{start} - T_{end}}{2}\right)^2 + b_{TC}^2}. \quad (\text{D.17})$$

Here, the thermocouple uncertainty  $b_{TC}$  is given as  $2.2^\circ\text{C}$ , while  $T_{start}$  and  $T_{end}$  are the recorded free-stream temperatures at the beginning and end of the run.

The pressure systematic uncertainty term  $b_P$  was similarly calculated as a combination of uncertainty values, given by

$$b_P = \sqrt{b_{cal}^2 + b_{inst}^2 + b_0^2}, \quad (\text{D.18})$$

where  $b_{cal}$  is the calibration uncertainty associated with the Scanivalve calibration,  $b_{inst}$  is the Scanivalve instrument uncertainty, given as 0.3% of full scale, and  $b_0$  is the "zero-out" uncertainty associated with manual zeroing of the transducer output. Based on the Scanivalve full scale range of 10 inches of water, the instrument uncertainty was calculated as  $b_{inst} = 7.5 \text{ Pa}$ . Moreover, the zero-out uncertainty was estimated based on a zero-out transducer error range of  $\pm 0.0005\text{V}$ . This uncertainty was calculated as  $b_0 = 2.3 \text{ Pa}$  using the sample Scanivalve calibration equation, shown in Figure 2.7 given as:

$$\Delta P = 1264.8 \cdot V + 2.9 \quad (\text{D.19})$$

Further, the calibration uncertainty  $b_{cal}$  was determined by combining the random standard uncertainty  $s_{P_{cal}}$  and the systematic standard uncertainty  $b_{P_{cal}}$  associated with the calibration's linear regression:

$$b_{cal} = \sqrt{s_{P_{cal}}^2 + b_{P_{cal}}^2} \quad (\text{D.20})$$

Here, the calibration uncertainty was calculated in the manner outlined in section 8-6 of the ASME PTC 19.1-2013 Test Uncertainty manual. The procedure will follow the example case of the pressure calibration, as shown in Figure 2.7. This procedure first requires the calculation of the linear fit's standard error of estimate  $SEE$ :

$$SEE = \sqrt{\frac{\sum_{j=1}^N (\Delta P_j - mV_j - c)^2}{N - 2}}. \quad (\text{D.21})$$

Here  $N$  is the number of calibration data pairs, which in this case is equal to 12.  $\Delta P_j$  and  $V_j$  are the differential pressure and voltage recorded at each of the 12 data points, respectively. The value  $m = 1264.8$  is taken from the first linear calibration coefficient, and  $c = 2.9$  is the second coefficient. The standard error of estimate was calculated as  $SEE = 2.1$  Pa for the sample case. The average calibration voltage  $V_{avg}$  can then be calculated as:

$$V_{avg} = \frac{1}{N} \sum_{j=1}^N V_j \quad (\text{D.22})$$

The average voltage was calculated as 0.98 V for this calibration. The random standard uncertainty associated with a non-calibration voltage measurement can be calculated as:

$$s_{P_{cal}} = SEE \sqrt{\frac{1}{N} + \frac{(V - \bar{V})^2}{\sum_{j=1}^N (V_j - \bar{V})^2}}, \quad (\text{D.23})$$

where  $V_j$  values are calibration voltages and  $V$  values are experimental (non-calibration) measurements. This uncertainty value, as indicated, varies with each voltage measurement, and thus with each streamwise velocity measurement. The calibration systematic standard uncertainty  $b_{P_{cal}}$  is taken as 0, as both the calibration voltages and the experimental voltages were recorded using the Scanivalve pressure transducer. Thus, the systematic uncertainty values associated with the calibration are already accounted for via the Scanivalve instrument uncertainty term.

Inserting all of the individual uncertainty values into their associated equations, the values of uncertainty for the freestream velocity and Mach number measurements with a 95% confidence interval are approximately  $\varepsilon_U/U = 0.4\%$  and  $\varepsilon_M/M = 0.5\%$ .

## D.2 Hot-wire Anemometry

The total standard uncertainty  $\varepsilon_U$  in the measurement of the streamwise velocity  $U$  is a combination of random uncertainty  $s_U$  and systematic uncertainty  $b_U$ :

$$\varepsilon_U = \sqrt{s_U^2 + b_U^2} \quad (\text{D.24})$$

The random uncertainty can then be written as:

$$s_U = \sqrt{\frac{\frac{1}{N-1} \sum_{i=1}^N (U_i - \bar{U})^2}{N}} \quad (\text{D.25})$$

where  $N$  is the number of samples and  $\bar{U}$  is the average flow velocity recorded over the run. The systematic uncertainty can then be expressed as:

$$b_U = \sqrt{(\frac{1}{k_\theta} b_\theta)^2 + (\frac{1}{k_{fit}} b_{fit})^2 + (\frac{1}{k_{cal}} b_{cal})^2 + (\frac{1}{k_P} b_P)^2 + (\frac{1}{k_T} b_T)^2 + (\frac{1}{k_{A/D}} b_{A/D})^2} \quad (\text{D.26})$$

where each  $k_i$  value is a coverage factor for an associated systematic uncertainty value, related to the measurement confidence intervals via the relationship presented in Table D.1.

The systematic uncertainty  $b_\theta$  of the probe's angular alignment was estimated as the difference between the magnitude of the angled flow and the streamwise component of the flow, given by:

$$b_\theta = U(1 - \cos(\theta)) \quad (\text{D.27})$$

where  $\theta$  is the probe's angle with respect to the freestream flow. The probe angle  $\theta$  was then estimated to be aligned within  $\pm 3^\circ$ . From there, the systematic uncertainty  $b_{fit}$  in the hot-wire calibration curve fit against the reference Pitot tube velocity measurements can be obtained as the product of the voltage error generated by the calibration and the derivative of the calibration curve. This can be expressed as:

$$b_{fit} = \frac{\partial U}{\partial V} b_V \quad (\text{D.28})$$

where  $b_V$  is the estimated standard error in the voltage measurement stemming from the use of the curve fit for velocity  $U$  and was calculated to be 0.0614 V. Additionally,  $\frac{\partial U}{\partial V}$  was calculated by differentiating Equation 2.7:

$$\frac{\partial U}{\partial V} = 5aV^4 + 4bV^3 + 3cV^2 + 2dV + e \quad (\text{D.29})$$

The systematic uncertainty in the hot-wire calibration  $b_{cal}$  can then be estimated as a combination of the uncertainty in the calibration flow speed values  $U_i$  or  $M_i$  and the deviation in flow direction and magnitude from the Pitot probe location to the hot-wire probe location during the calibration process. This second term can be understood as a measure of the freestream flow uniformity. The calibration flow speeds were measured by a Scanivalve transducer which was calibrated against the differential pressure measured by two Setra transducers. The Mach number uncertainty terms were then calculated from the definition of the Mach number as:

$$M = \sqrt{\frac{2(P_T - P_s)}{\gamma P_s}} \quad (\text{D.30})$$

where  $P_s$  is the local static pressure and  $P_T$  is the local stagnation pressure measured by the Setra transducer. The sensitivities of  $M$  with respect to each of these variables can then be obtained by partial differentiation of Equation (14) as:

$$\frac{\partial M}{\partial P_s} = \frac{-P_T}{M\gamma P_s^2} \quad (\text{D.31})$$

$$\frac{\partial M}{\partial P_T} = \frac{1}{M\gamma P_s} \quad (\text{D.32})$$

The calibration Mach number systematic uncertainty  $b_{M_{cal}}$  can then be written as:

$$b_{M_{cal}} = \sqrt{\left(\frac{\partial M}{\partial P_s} b_{P_s}\right)^2 + \left(\frac{\partial M}{\partial P_T} b_{P_T}\right)^2} \quad (\text{D.33})$$

where  $b_{P_T}$  and  $b_{P_s}$  are both Setra instrument uncertainty values, each given as 0.05% of full scale, or 25 Pa. The calibration flow velocity can be calculated from the Mach number as:

$$U = M\sqrt{\gamma RT} \quad (\text{D.34})$$

This allows for the uncertainty in the calibration velocity values to be expressed from Equations D.33 and D.34 as:

$$b_{U_{cal}} = \sqrt{\left(\frac{U}{M} b_{M_{cal}}\right)^2 + \left(\frac{U}{2T} \Delta T\right)^2} \quad (\text{D.35})$$

where  $\Delta T$  is the variation in temperature measurement across the calibration, taken as 3°C. The calibration uncertainty can then be written as:

$$b_{cal} = \sqrt{b_{U_{cal}}^2 + b_{U_{uniformity}}^2} \quad (\text{D.36})$$

Here,  $b_{U_{uniformity}}$  is the uncertainty associated with variations in freestream flow uniformity, and can be obtained by examining differences in the fluctuating components of velocity between the hot-wire probe location and the Pitot probe location during calibration. This was achieved by processing streamwise velocity data from benchmark empty tunnel, freestream Pitot-static test entries, and calculating the flow velocity's typical standard deviation across planar regions. In this way, the value of  $b_{U_{uniformity}}$  was computed as 0.6108 m/s.

The systematic uncertainty due to changes in ambient pressure  $b_P$  affects the total uncertainty through its impact on calibration flow density. In other words, the change in flow density is influenced by changes in ambient pressure, and thus affects the uncertainty calculation through its effect on mass flux through the calibration measurement plane. Through dimensional analysis and the calibration equation derivative given by Equation D.29, this uncertainty term can be written as:

$$b_P = \frac{\partial U}{\partial V} \frac{\partial V}{\partial \rho} \frac{\partial \rho}{\partial P} \Delta P = \frac{U}{P} \Delta P \quad (\text{D.37})$$

where  $\Delta P$  is the change in ambient pressure across the calibration run, estimated as 3 hPa.

The uncertainty term  $b_T$  arises due to uncertainty in the measured temperature, as the hot-wire voltage is directly related to heat transfer, and any changes in temperature additionally impact calibration flow density. In this way, the hot-wire voltage becomes dependent on both density and temperature, and can be cast as a function given by:

$$V(\rho, U, T) = (T_w - T)\rho V(U) \quad (\text{D.38})$$

where  $V(U)$  is the hot-wire voltage which generates a mean velocity  $U$  when inserted into the hot-wire calibration given by Equation 2.7. Additionally,  $T$  is the profile temperature,  $\rho$  is the profile density, and  $T_w$  is the wire temperature, calculated as a corrected temperature and given by:

$$T_w = T + \frac{OHR - 1}{\alpha} \quad (\text{D.39})$$

The systematic uncertainty due to changes in temperature can then be understood as a combination of uncertainty due to convective heat transfer and uncertainty due to changes in calibration flow density:

$$b_T = \frac{\partial U}{\partial V} \frac{\partial V}{\partial T} \Delta T + \frac{\partial U}{\partial V} \frac{\partial V}{\partial \rho} \frac{\partial \rho}{\partial T} \Delta T = \frac{\partial U}{\partial V} V \Delta T \left( \frac{\alpha}{OHR - 1} \right) + \frac{U}{T} \Delta T \quad (\text{D.40})$$

where the first term is convective and the second term relates to the calibration flow density, and  $\Delta T$  remains that temperature variation across the calibration, 3°C.

A further uncertainty term arises from the conversion from analog to digital data output. This systematic A/D uncertainty  $b_{A/D}$  can be expressed as:

$$b_{A/D} = \frac{E_{AD}}{2^n} \frac{\partial U}{\partial V} \quad (\text{D.41})$$

where  $E_{AD}$  is the A/D board input range of 20 V and  $n$  is the resolution in bits, taken as 16.

The total standard uncertainty  $\varepsilon_U/U$  of velocity with a 95% confidence interval ranges between 3.5-8.1%, increasing with proximity to the wall. This is owed largely to the increasing turbulence (larger random uncertainty  $s_U$ ) and smaller velocities. Consideration of the wall heating was not addressed here. For the temperature corrections made (Equation 2.8), it was assumed that the wall temperature was the same as the freestream temperature. However, over the experimental run, the surface shear stress heated the surface. This temperature difference was not measured, but would affect the accuracy of the near wall measurements [74]. Another consideration not mentioned is the spatial averaging over the length of the hot-wire. This influences the magnitude and shape of the turbulence profiles, particularly for higher wave number energies with viscous length scales smaller than the length of the wire,  $l^+ < 150$  [75].

The uncertainty with respect to the turbulent shear stress is solely a function of

the variance and kurtosis of the velocity, and the number of samples taken:

$$\varepsilon_{\overline{u'^2}} = \sqrt{\frac{\overline{u'^4} - \overline{u'^2}^2}{N}}. \quad (\text{D.42})$$

### D.3 Photogrammetric Oil-Film Interferometry

There is a vast literature dealing with uncertainty analysis in OFI [76, 77, 78, 41, 79]. In particular, a summary of error sources and their estimated value on OFI can be found in table 2 of Zilliac [77], whereas a detailed uncertainty quantification via mathematical and statistical approaches to identify the parameters of the highest impact on the overall uncertainty to OFI was done by [41]. In addition, a propagation of the uncertainties of each of the parameters in Equation (2.10) for the setup is detailed in Section D.4 in Simmons [80]. Herein, we only discuss the dominant uncertainties.

We consider two categories of uncertainties: probabilistic and systematic. The probabilistic errors are uncertainties that are considered to be independent of each other and can occur due to noise, fringe visibility, surface imperfections, variations in the illumination on the surface, and also uncertainty as a result of a departure from the assumptions that are used to obtain Equation (2.10), such as two-dimensionality of the thin layer. One way to reduce these error impacts is to evaluate hundreds of individual  $C_f$  values at the same location, which would lead to an average  $C_f$  with a small precision error. For example, see Figure 10 of Naughton et al. [44], and Figure 10 of Naughton et al. [34], where the total uncertainty was determined by summation in the RMS sense, showing its decrease with an increasing number of samples. In this study, to increase the accuracy of the fringe spacing evaluation, the distance between the fringes for each column of pixels in the rectangle was evaluated (at least 100 columns were used) and averaged. More  $M$  independent measurements of fringes along the span would yield more data to be averaged, thus, reducing the random error  $e_r$  by a factor of  $\sqrt{M}$ , i.e.,  $e_r/\sqrt{M}$ . However, this procedure cannot help with systematic errors.

In this study, two factors contribute the most to the overall systematic error in wall-shear stress measurements: the estimated incident camera angle and the variation in the oil viscosity as a function of temperature measurement. The results indicate that when model curvature is high, or the camera-to-model distance is short, significant uncertainties of the order of 10% in skin friction can be introduced due to angle bias if photogrammetry is not applied [46, 34]. In this study, 1 degree in angle error would lead to 0.88% error in skin friction. With the photogrammetry technique employed, the angle to every pixel in the image is estimated to be below 0.2 degrees in the selected rectangle of interest, thus reducing the error to be negligible. In that regard, the uncertainty caused by the photogrammetry was found to be, in most cases, significantly less than the other uncertainties [46, 34]. An additional uncertainty is that the curvature of the checkerboard is not the same as the curvature where the fringe pattern was measured. The checkerboard was made sufficiently small and

placed along the span where the fringes were taken with uniform curvature captured by the checkerboard. Difficulties may arise in measuring the skin friction values on 3D bump regions with high curvatures (e.g., the apex region), where greater care on checkerboard size selection and mounting location should be taken.

The remaining source of error is the viscosity variation with temperature, where propagation analysis yields that for every degree Celsius, the calculated shear stress results in a 1.8% error. In the present study, a K-type calibrated thermocouple was used, where calibration assured that its accuracy was within 0.5 °C.

Lastly, non-constant run conditions can be an additional leading source of error, with tunnel startup and shutdown transients producing different flow conditions from the test condition. A conservative estimate of skin friction uncertainty is to assume that the uncertainty is proportional to the ratio of time spent in startup and shutdown relative to the total run time [37]. Thus, to make it negligible for the analysis, experimental runs lasted at least 20 min, whereas the startup time with added shutdown time took less than 40 s (3.33% of total run time) for the fasted tunnel speed, which lead to uncertainty of 0.7% (over-prediction) to the overall error in  $C_f$  in the experiments.

To conclude, the overall bias error in mean skin friction values is taken to be within 2%, assuming that the oil was calibrated with the uncertainty of 0.2% of  $\nu_0$ , and an oil temperature uncertainty of 0.5 °C. The uncertainties due to initial oil conditions, light source wavelength variations, oil index of refraction variations, pressure gradients, and tunnel startup and shutdown effects have been neglected because they were considered too small to impact the total uncertainty of the  $C_f$  measurements.

#### D.4 Particle Image Velocimetry

The random uncertainty quantification of the individual PIV components is critical for the creation of a benchmark data set for future CFD validation. The instantaneous velocity fields are used in some cases to compute the uncertainty in the derived quantities, such as the turbulence fields. The uncertainties of the mean velocity, as well as the mean turbulence quantities, are presented here. The foundation of the PIV measurement is particle displacement, which is then related to velocity by the time between frame pairs,  $\delta t$ . Time-averaged statistical quantities over a time interval  $T$  also need to be considered, often described as a "random" error. In this case presented, the number of effective samples will be implemented, and is related to the temporal correlation of data from one frame set to another. The effective sample number is a function of the autocorrelation between subsequent samples at a select point in space:

$$N_{\text{eff}} = \frac{N}{\sum_{n=-\infty}^{n=\infty} \rho(n\Delta t)} \quad (\text{D.43})$$

where  $\rho$  is the autocorrelation function,  $\Delta t$  is the time between samples, and  $n$  are integers. An integral time scale is often used so that

$$T_{\text{int}} = \int_0^\infty \rho(\tau) d\tau \quad \text{and} \quad N_{\text{eff}} = \frac{T}{2T_{\text{int}}}. \quad (\text{D.44})$$

The time mean of a certain discrete signal  $x$  is

$$X = \frac{1}{N} \sum_{i=1}^N x_i, \quad (\text{D.45})$$

while its standard deviation is

$$\sigma_x = \sqrt{\frac{1}{N-1} \sum_{i=1}^N (x_i - X)^2} \quad (\text{D.46})$$

and the variance of the measurement is simply  $\sigma_x^2$ . Using these definitions, and implementing the effective number of samples for the flow, the uncertainty of the velocity is as follows:

$$\varepsilon_U = \frac{\sigma_u}{\sqrt{N_{\text{eff}}}}, \quad (\text{D.47})$$

and a similar equation can yield the uncertainty for the mean of  $v$ , as is the case for all following analysis. It should be noted that the standard deviation measurement includes both the physical velocity fluctuations as well as erroneous measurement errors caused by noise, which can be represented by

$$\varepsilon_{\sigma_u} = \frac{\sigma_u}{\sqrt{2(N_{\text{eff}} - 1)}}. \quad (\text{D.48})$$

The root-mean-squared value of the turbulence and its uncertainty is computed using these definitions of the standard deviation since

$$u_{\text{RMS}} = \sqrt{\overline{u'^2}} = \sqrt{\frac{1}{N-1} \sum_{i=1}^N (u_i - U)^2} = \sigma_u, \quad (\text{D.49})$$

where  $u'$  is the fluctuating part of  $u = U + u'$ . The uncertainty of the normal Reynolds stresses, which is simply the variance of the velocity ( $R_{uu} = \overline{u'u'} = \sigma_u^2$ ) can be expressed using the uncertainty of the variance:

$$\varepsilon_{R_{uu}} = \sigma_u^2 \sqrt{\frac{2}{N_{\text{eff}} - 1}} \cong R_{uu} \sqrt{\frac{2}{N_{\text{eff}}}}. \quad (\text{D.50})$$

The final quantity to focus attention to is the Reynolds shear stress and its uncertainty. This becomes a bit more complex than the normal stresses, as it involves an additional cross correlation coefficient ( $\rho_{uv}$ ) between velocity components  $u$  and  $v$  that arises from the mean evaluation, shown by the expression:

$$R_{uv} = \overline{u'v'} = \frac{1}{N-1} \sum_{i=1}^N (u_i - U)(v_i - V) = \rho_{uv}\sigma_u\sigma_v. \quad (\text{D.51})$$

The uncertainty of the measurement is then obtained by

$$\varepsilon_{R_{uv}} = \sigma_u\sigma_v \sqrt{\frac{1 + \rho_{uv}}{N_{\text{eff}} - 1}}. \quad (\text{D.52})$$

## D.5 Static Pressure Coefficient

The uncertainty analysis conducted for the static pressure coefficient followed the procedure outlined by the ASME PTC 19.1-2013 Test Uncertainty manual and that provided in Appendix D.1 of Simmons [8]. The standard uncertainty of  $C_p$  is the sum of squares of the random and systematic standard uncertainties, denoted by  $s_{C_p}$  and  $b_{C_p}$ , respectively:

$$\varepsilon_{C_p} = \sqrt{s_{C_p}^2 + b_{C_p}^2}. \quad (\text{D.53})$$

The static pressure coefficient given by Equation 2.13 is functionally dependant on the difference between the local static pressure and the reference static pressure  $\Delta P_i$ , and the dynamic pressure  $q$ . The sensitivities of  $C_p$  to each of these parameters were obtained via partial differentiation and are given by

$$\frac{\partial C_p}{\partial \Delta P_i} = \frac{1}{q}, \text{ and} \quad (\text{D.54})$$

$$\frac{\partial C_p}{\partial q} = -\frac{\Delta P_i}{q^2}. \quad (\text{D.55})$$

The random uncertainty of the static pressure coefficient is a function of the random uncertainties of its functionally dependent values:

$$s_{C_p} = \sqrt{\left(\frac{\partial C_p}{\partial \Delta P_i} s_{\Delta P_i}\right)^2 + \left(\frac{\partial C_p}{\partial q} s_q\right)^2}, \quad (\text{D.56})$$

and after introducing the sensitivities of  $C_p$  provided by Equations D.54 and D.55 the random uncertainty is represented by

$$s_{C_p} = \frac{1}{|q|} \sqrt{s_{\Delta P_i}^2 + C_p^2 s_q^2}. \quad (\text{D.57})$$

The random standard uncertainties of the pressure difference and dynamic pressure are related to the estimator variances and are provided by the following equations:

$$s_{\Delta P_i} = \sqrt{\frac{\sigma_{\Delta P_i}^2}{N}} \quad (\text{D.58})$$

$$s_q = \sqrt{\frac{\sigma_q^2}{N}} \quad (\text{D.59})$$

where  $N$  is the number of samples taken during the measurement.

The propagation of the systematic uncertainties was computed using an analogous procedure so that

$$b_{C_p} = \sqrt{\left(\frac{\partial C_p}{\partial \Delta P_i} b_{\Delta P_i}\right)^2 + \left(\frac{\partial C_p}{\partial q} b_q\right)^2} = \frac{1}{|q|} \sqrt{b_{\Delta P_i}^2 + C_p^2 b_q^2}. \quad (\text{D.60})$$

Due to the fact that the  $\Delta P_i$  and  $q_\infty$  measurements were obtained using the same pressure transducer system, a systematic uncertainty for the pressure,  $b_p$ , was introduced to simplify Equation D.60 to

$$b_{C_p} = \frac{b_p}{|q|} \sqrt{1 + C_p^2}. \quad (\text{D.61})$$

The systematic uncertainty of the pressure measurement was divided into the calibration uncertainty component,  $b_{cal}$  and the instrument uncertainty,  $b_{inst}$  given by

$$b_p = \sqrt{b_{cal}^2 + b_{inst}^2}. \quad (\text{D.62})$$

Based on the Scanivalve full scale range of 10 inches of water and its specification of 0.3% uncertainty, the instrument uncertainty was calculated as  $b_{inst} = 7.5$  Pa. The linear calibration fit was shown in Figure 2.23 and the equation for the fit was

$$\Delta P = 590.7V + 0.3 \quad (\text{D.63})$$

where  $V$  is the transducer output [V] and  $\Delta P$  is the pressure differential measured between the specified local pressure channel ( $P_i$ , or  $P_0$  for  $q_\infty$ ) and the reference static velocity,  $P_\infty$  [Pa]. The calibration uncertainty was calculated in the manner outlined in section 8-6 of the ASME PTC 19.1-2013 Test Uncertainty manual. The procedure followed the example case of the pressure calibration, as shown in Figure 2.23. This procedure first requires the calculation of the linear fit's standard error of estimate  $SEE$ :

$$SEE = \sqrt{\frac{\sum_{j=1}^N (\Delta P_j - mV_j - c)^2}{N - 2}}. \quad (\text{D.64})$$

Here  $N$  is the number of calibration data pairs, which in this case is equal to 30.  $\Delta P_j$  and  $V_j$  are the differential pressure and voltage recorded at each of the 30 data points, respectively. The value  $m = 590.7$  is taken from the first linear calibration coefficient, and  $c = 0.3$  is the second coefficient. The standard error of estimate was calculated as  $SEE = 0.54$  Pa for the sample case. The average calibration voltage

$V_{avg}$  can then be calculated as:

$$V_{avg} = \frac{1}{N} \sum_{j=1}^N V_j \quad (\text{D.65})$$

The average voltage was calculated as 0.11 V for this calibration. The standard uncertainty associated with a non-calibration voltage measurement can be calculated as:

$$b_{cal} = SEE \sqrt{\frac{1}{N} + \frac{(V - V_{avg})^2}{\sum_{j=1}^N (V_j - V_{avg})^2}}, \quad (\text{D.66})$$

where  $V_j$  values are calibration voltages and  $V$  values are experimental (non-calibration) measurements. This uncertainty value, as indicated, varies with each voltage measurement, and thus with each tap location. The combined total uncertainty of  $C_p$  (Equation D.53) can be rewritten after utilizing Equations D.57 and D.61 and all of the subsequent analysis as

$$\varepsilon_{C_p} = \frac{1}{|q|} \sqrt{b_p^2(1 + C_p^2) + (s_{\Delta P_i}^2 + C_p^2 s_q^2)} \quad (\text{D.67})$$

The expanded uncertainty can be computed by multiplying the combined uncertainty by the Student's t-table value,  $t_{\nu,p} = 1.96$ , where  $\nu = N - 1$  is greater than 1000 and  $p$  is for a 95% confidence interval.

## D.6 Freestream Uniformity

The total standard uncertainty  $\varepsilon_U$  in the measurement of the streamwise velocity  $U$  can be determined by breaking down its uncertainty into individually measured quantities. The functional dependence of the freestream velocity depends on the differential pressure,  $\Delta P$ , and the fluid density,  $\rho$  as shown by Equation 2.2. Hence the velocity can be shown to be  $U = f(\Delta P, \rho)$ . The total standard uncertainty of  $U$  can then be represented by the total uncertainties of the measured quantities and their sensitivities to the desired quantity:

$$\varepsilon_U = \sqrt{\left(\frac{\partial U}{\partial \Delta P} \varepsilon_{\Delta P}\right)^2 + \left(\frac{\partial U}{\partial \rho} \varepsilon_{\rho}\right)^2}. \quad (\text{D.68})$$

The sensitivities of  $U$  with respect to each of its functional quantities can be expressed via partial differentiation as:

$$\frac{\partial U}{\partial \Delta P} = \sqrt{\frac{1}{2\Delta P \rho}} \quad (\text{D.69})$$

$$\frac{\partial U}{\partial \rho} = -\sqrt{\frac{\Delta P}{2\rho^3}} \quad (\text{D.70})$$

Because the density was not directly measured, there are uncertainties associated

with the functional quantities, as  $\rho = f(T, P_{\text{atm}}, RH)$ . Thus, the total uncertainty of density can be shown to be

$$\varepsilon_\rho = \sqrt{\left(\frac{\partial\rho}{\partial T}\varepsilon_T\right)^2 + \left(\frac{\partial\rho}{\partial P_{\text{atm}}}\varepsilon_{P_{\text{atm}}}\right)^2 + \left(\frac{\partial\rho}{\partial RH}\varepsilon_{RH}\right)^2} \quad (\text{D.71})$$

Now, the measured quantities that make up the calculated quantities must contain a reading uncertainty from the measurement display of the instrument ( $\varepsilon_R$ ) and the systematic uncertainty related to instrument ( $\varepsilon_k$ , where  $k$  can represent individual sources such as total accuracy, hysteresis, offset, etc.). The temperature measurements were made using a k-type thermocouple, which has an accuracy of  $\pm 2.2^\circ\text{C}$  and a resolution in this case of  $0.1^\circ\text{C}$ , so the reading accuracy can be estimated by  $0.005^\circ\text{C}$ . Hence the uncertainty in the temperature measurement can be shown in the following equation:

$$\varepsilon_T = \sqrt{\varepsilon_{T,R}^2 + \varepsilon_{T,k}^2} = \sqrt{0.005^2 + 2.2^2} = 2.20 \text{ K} \quad (\text{D.72})$$

Similarly, the uncertainty in the atmospheric pressure and relative humidity measurements by the Fisher barometer can be determined.

$$\varepsilon_{P_{\text{atm}}} = \sqrt{\varepsilon_{P_{\text{atm}},R}^2 + \varepsilon_{P_{\text{atm}},k}^2} = \sqrt{100^2 + 400^2} = 412.3 \text{ Pa} \quad (\text{D.73})$$

$$\varepsilon_{RH} = \sqrt{\varepsilon_{RH,R}^2 + \varepsilon_{RH,k}^2} = \sqrt{1^2 + 3^2} = 3.2\% \quad (\text{D.74})$$

From Equations 2.3 and 2.4, the sensitivities of  $\rho$  to its functional dependent quantities can be estimated using a standard finite difference approximation for each variable so that  $\partial\rho/\partial() \approx \Delta\rho/\Delta()$ . Placing the unchanging variables at values typically seen for testing conditions, the sensitivities were determined to be the following:  $\partial\rho/\partial T = 4 \times 10^{-3} \text{ kg/m}^3\text{K}$ ,  $\partial\rho/\partial P_{\text{atm}} = 1.2 \times 10^{-5} \text{ kg/m}^3\text{Pa}$ , and  $\partial\rho/\partial RH = 1.2 \times 10^{-4} \text{ kg/m}^3$ . Combining Equations D.84-D.87, the uncertainty in the density is found to be  $\varepsilon_\rho = 0.010 [\text{kg/m}^3]$ . The dominant source of uncertainty in the density arises from the accuracy of the k-type thermocouple.

Next the focus on differential pressure, measured using the calibrated Scanivalve pressure transducer, will be discussed. A few different sources of uncertainty must be considered. These include the random uncertainty ( $\varepsilon_{\Delta P,N}$ ) that is caused by unknown changes from one measurement to another, the calibration uncertainty from the wind tunnel's Setra pressure transducers to the data acquiring Scanivalve transducer ( $\varepsilon_{\Delta P,C}$ ), as well as the uncertainties that come from the instrumentation, the analog to digital (A/D) conversion, the "zero-out" uncertainty caused by the voltage drift of the transducer, and the probe alignment in the test section. The combination of these sources is given by Equation D.88.

$$\varepsilon_{\Delta P} = \sqrt{\varepsilon_{\Delta P,N}^2 + \varepsilon_{\Delta P,\text{cal}}^2 + \varepsilon_{\Delta P,k}^2 + \varepsilon_{\Delta P,A/D}^2 + \varepsilon_{\Delta P,0}^2 + \varepsilon_{\Delta P,\theta}^2} \quad (\text{D.75})$$

Because the velocity is time-averaged over many samples, the random uncertainty of the mean can be determined by the following expression:

$$\varepsilon_{\Delta P,N} = t_{v,P} \frac{\sigma_{\Delta P}}{\sqrt{N}}, \quad (\text{D.76})$$

where  $\sigma_{\Delta P}$  is the standard deviation of the pressure difference, and  $N = 60000$  is the number of samples, for each point. The value  $t_{v,P} = 1.96$  is taken from the student t-table for a large sample size ( $>1000$ ) and a selected confidence interval of 95%. The random uncertainties are on the order of  $\varepsilon_{\Delta P,N} \approx 0.05$  Pa.

The calibration uncertainty must include both the systematic uncertainty of the wind-tunnel's built-in Setra transducer as well as the error of the linear curve fit to the measuring Scanivalve transducer. Hence the uncertainty becomes  $\varepsilon_{\Delta P,\text{cal}} = \sqrt{\varepsilon_{\text{cal},k}^2 + \varepsilon_{\text{cal,fit}}^2}$ . The value  $\varepsilon_{\text{cal},k} = 25$  Pa, is simply the accuracy of the transducer. The linear fit error can be determined by the standard deviation of the error between the linear progression line and the individual calibration points:

$$\varepsilon_{\text{cal,fit}} = t_{v,P} \sqrt{\frac{\sum_{i=1}^N (y_i - (aV_i + b))^2}{N - 2}}, \quad (\text{D.77})$$

where  $N = 12$  is the number of calibration points, and the constants  $a = 1176.5$  and  $b = 1.69$  were taken from the best linear fit of the calibration points,  $y_i$  (see Fig. 2.7). In this case, the student t-table's value reflects a 95% confidence interval for  $v = N - 1 = 11$ . In the case shown above the fit error is  $\varepsilon_{\text{cal,fit}} = 0.031$  Pa. The calibration uncertainty is clearly dominated by the systematic uncertainty of the build-in pressure transducers so that  $\varepsilon_{\Delta P,\text{cal}} = \varepsilon_{\text{cal},k} = 25$  Pa.

The systematic uncertainty of  $\Delta P$  is given by the accuracy of the Scanivalve system, so that  $\varepsilon_{\Delta P,k} = 7.47$  Pa.

The error associate with the A/D conversion can be determined by the resolution of the device, with a 5% allowance. In this case the NI USB 6343 DAQ was set to an input range from -5 to 5V. The 16-bit converter would then have an expected resolution of

$$\frac{5V - (-5V)}{2^{16}} * 1.05 = 160\mu V. \quad (\text{D.78})$$

After applying the linear fit to convert the voltage to  $\Delta P$ , the uncertainty from the A/D conversion is found to be  $\varepsilon_{\Delta P,A/D} = 0.19$  Pa. Similarly, the "zero-out" uncertainty can be estimated by applying the linear fit to the error in setting the manual "zero" for the transducer. The analog transducer showed minor drifting of the no-flow voltage between experimental runs. Before each test while the  $\Delta P = 0$  (no flow  $U_\infty = 0$ ), the Scanivalve system voltage was manually set to within  $\pm 1$  mV of zero. The uncertainty associated with this is  $\varepsilon_{\Delta P,0} = 1.18$  Pa.

Finally, the uncertainty in the probe alignment should be considered in the analysis. Because the Pitot-static probe only measured velocity that is parallel to the measurement head, the misalignment uncertainty is given by the following equation:

$$\varepsilon_{\Delta P, \theta} = \Delta P (1 - \cos(\theta)) (1 - \sin(90 - \phi)), \quad (\text{D.79})$$

where  $\theta$  is the yaw angle and  $\phi$  is the angle of attack of the measurement head of the Pitot-static probe. Both angles can be estimated to be within  $\pm 3^\circ$ . The resulting uncertainty caused by probe misalignment is  $\varepsilon_{\Delta P, \theta} / \Delta P = 1.9 \times 10^{-6}$ .

The above elements can be inserted into Equation D.88. For a sample case for  $U_\infty \approx 70$  m/s at standard atmosphere and temperature, the uncertainty for the dynamic pressure is calculated to be  $\varepsilon_{\Delta P} = 26.1$  Pa, which is dominated by the calibration uncertainty.

Combining the uncertainties and mean values for  $\rho$  and  $\Delta P$  with Equations D.81-D.83, the total standard uncertainty in velocity can be computed for each data point using the final form:

$$\varepsilon_U = \sqrt{\left(\sqrt{\frac{1}{2\Delta P \rho}} \varepsilon_{\Delta P}\right)^2 + \left(\sqrt{\frac{\Delta P}{2\rho^3}} \varepsilon_\rho\right)^2} \quad (\text{D.80})$$

The uncertainty in the freestream velocity measurements for a 95% confidence interval is  $\varepsilon_U/U < 0.7\%$  across the 5 measurement planes.

## D.7 Empty Tunnel Side Wall Boundary Layers

The total standard uncertainty  $\varepsilon_U$  in the measurement of the streamwise velocity  $U$  can be determined by breaking down its uncertainty into individually measured quantities. The functional dependence of the freestream velocity depends on the differential pressure,  $\Delta P$ , and the fluid density,  $\rho$  as shown by Equation 2.2. Hence the velocity can be shown to be  $U = f(\Delta P, \rho)$ . The total standard uncertainty of  $U$  can then be represented by the total uncertainties of the measured quantities and their sensitivities to the desired quantity:

$$\varepsilon_U = \sqrt{\left(\frac{\partial U}{\partial \Delta P} \varepsilon_{\Delta P}\right)^2 + \left(\frac{\partial U}{\partial \rho} \varepsilon_\rho\right)^2}. \quad (\text{D.81})$$

The sensitivities of  $U$  with respect to each of its functional quantities can be expressed via partial differentiation as:

$$\frac{\partial U}{\partial \Delta P} = \sqrt{\frac{1}{2\Delta P \rho}} \quad (\text{D.82})$$

$$\frac{\partial U}{\partial \rho} = -\sqrt{\frac{\Delta P}{2\rho^3}} \quad (\text{D.83})$$

Because the density was not directly measured, there are uncertainties associated with the functional quantities, as  $\rho = f(T, P_{\text{atm}}, RH)$ . Thus, the total uncertainty of

density can be shown to be

$$\varepsilon_{\rho} = \sqrt{\left(\frac{\partial\rho}{\partial T}\varepsilon_T\right)^2 + \left(\frac{\partial\rho}{\partial P_{\text{atm}}}\varepsilon_{P_{\text{atm}}}\right)^2 + \left(\frac{\partial\rho}{\partial RH}\varepsilon_{RH}\right)^2} \quad (\text{D.84})$$

The measured quantities that make up the calculated quantities must contain a reading uncertainty from the measurement display of the instrument ( $\varepsilon_R$ ) and the systematic uncertainty related to instrument ( $\varepsilon_k$ , where  $k$  can represent individual sources such as total accuracy, hysteresis, offset, etc.). The temperature measurements were made using a k-type thermocouple, which has an accuracy of  $\pm 2.2^\circ\text{C}$  and a resolution in this case of  $0.1^\circ\text{C}$ , so the reading accuracy can be estimated by  $0.005^\circ\text{C}$ . Hence the uncertainty in the temperature measurement can be shown in the following equation:

$$\varepsilon_T = \sqrt{\varepsilon_{T,R}^2 + \varepsilon_{T,k}^2} = \sqrt{0.005^2 + 2.2^2} = 2.20 \text{ K} \quad (\text{D.85})$$

Similarly, the uncertainty in the atmospheric pressure and relative humidity measurements by the Fisher barometer can be determined.

$$\varepsilon_{P_{\text{atm}}} = \sqrt{\varepsilon_{P_{\text{atm}},R}^2 + \varepsilon_{P_{\text{atm}},k}^2} = \sqrt{100^2 + 400^2} = 412.3 \text{ Pa} \quad (\text{D.86})$$

$$\varepsilon_{RH} = \sqrt{\varepsilon_{RH,R}^2 + \varepsilon_{RH,k}^2} = \sqrt{1^2 + 3^2} = 3.2\% \quad (\text{D.87})$$

From Equations 2.3 and 2.4, the sensitivities of  $\rho$  to its functional dependent quantities can be estimated using a standard finite difference approximation for each variable so that  $\partial\rho/\partial() \approx \Delta\rho/\Delta()$ . Placing the unchanging variables at values typically seen for testing conditions, the sensitivities were determined to be the following:  $\partial\rho/\partial T = 4 \times 10^{-3} \text{ kg/m}^3\text{K}$ ,  $\partial\rho/\partial P_{\text{atm}} = 1.2 \times 10^{-5} \text{ kg/m}^3\text{Pa}$ , and  $\partial\rho/\partial RH = 1.2 \times 10^{-4} \text{ kg/m}^3$ . Combining Equations D.84-D.87, the uncertainty in the density is found to be  $\varepsilon_{\rho} = 0.010 \text{ [kg/m}^3]$ . The dominant source of uncertainty in the density arises from the accuracy of the k-type thermocouple.

Next the focus on differential pressure, measured using the calibrated Scanivalve pressure transducer, will be discussed. A few different sources of uncertainty must be considered. These include the random uncertainty ( $\varepsilon_{\Delta P,N}$ ) that is caused by unknown changes from one measurement to another, the calibration uncertainty from the wind tunnel's Setra pressure transducers to the data acquiring Scanivalve transducer ( $\varepsilon_{\Delta P,C}$ ), as well as the uncertainties that come from the instrumentation, the analog to digital (A/D) conversion, the "zero-out" uncertainty caused by the voltage drift of the transducer, and the probe alignment in the test section. The combination of these sources is given by Equation D.88.

$$\varepsilon_{\Delta P} = \sqrt{\varepsilon_{\Delta P,N}^2 + \varepsilon_{\Delta P,\text{cal}}^2 + \varepsilon_{\Delta P,k}^2 + \varepsilon_{\Delta P,A/D}^2 + \varepsilon_{\Delta P,0}^2 + \varepsilon_{\Delta P,\theta}^2} \quad (\text{D.88})$$

Because the velocity is time-averaged over many samples, the random uncertainty

of the mean can be determined by the following expression:

$$\varepsilon_{\Delta P,N} = t_{v,P} \frac{\sigma_{\Delta P}}{\sqrt{N}}, \quad (\text{D.89})$$

where  $\sigma_{\Delta P}$  is the standard deviation of the pressure difference, and  $N = 20000$  is the number of samples, for each point. The value  $t_{v,P} = 1.96$  is taken from the student t-table for a large sample size ( $>1000$ ) and a selected confidence interval of 95%. The random uncertainties are on the order of  $\varepsilon_{\Delta P,N} \approx 0.20$  Pa.

The calibration uncertainty must include both the systematic uncertainty of the wind-tunnel's built-in Setra transducer as well as the error of the linear curve fit to the measuring Scanivalve transducer. Hence the uncertainty becomes  $\varepsilon_{\Delta P,\text{cal}} = \sqrt{\varepsilon_{\text{cal},k}^2 + \varepsilon_{\text{cal,fit}}^2}$ . The value  $\varepsilon_{\text{cal},k} = 25$  Pa, is simply the accuracy of the transducer. The linear fit error can be determined by the standard deviation of the error between the linear progression line and the individual calibration points:

$$\varepsilon_{\text{cal,fit}} = t_{v,P} \sqrt{\frac{\sum_{i=1}^N (y_i - (aV_i + b))^2}{N - 2}}, \quad (\text{D.90})$$

where  $N = 12$  is the number of calibration points, and the constants  $a = 1176.5$  and  $b = 1.69$  were taken from the best linear fit of the calibration points,  $y_i$  (see Figure 2.7). In this case, the student t-table's value reflects a 95% confidence interval for  $v = N - 1 = 11$ . In the case shown above the fit error is  $\varepsilon_{\text{cal,fit}} = 0.031$  Pa. The calibration uncertainty is clearly dominated by the systematic uncertainty of the build-in pressure transducers so that  $\varepsilon_{\Delta P,\text{cal}} = \varepsilon_{\text{cal},k} = 25$  Pa.

The systematic uncertainty of  $\Delta P$  is given by the accuracy of the Scanivalve system, so that  $\varepsilon_{\Delta P,k} = 7.47$  Pa.

The error associate with the A/D conversion can be determined by the resolution of the device, with a 5% allowance. In this case the NI USB 6343 DAQ was set to an input range from -5 to 5 V. The 16-bit converter would then have an expected resolution of

$$\frac{5V - (-5V)}{2^{16}} * 1.05 = 160\mu V. \quad (\text{D.91})$$

After applying the linear fit to convert the voltage to  $\Delta P$ , the uncertainty from the A/D conversion is found to be  $\varepsilon_{\Delta P,A/D} = 0.19$  Pa. Similarly, the "zero-out" uncertainty can be estimated by applying the linear fit to the error in setting the manual "zero" for the transducer. The analog transducer showed minor drifting of the no-flow voltage between experimental runs. Before each test while the  $\Delta P = 0$  (no flow  $U_\infty = 0$ ), the Scanivalve system voltage was manually set to within  $\pm 1$  mV of zero. The uncertainty associated with this is  $\varepsilon_{\Delta P,0} = 1.18$  Pa.

Finally, the uncertainty in the probe alignment should be considered in the analysis. Because the Pitot-static probe only measured velocity that is parallel to the measurement head, the misalignment uncertainty is given by the following equation:

$$\varepsilon_{\Delta P,\theta} = \Delta P(1 - \cos(\theta))(1 - \sin(90 - \phi)), \quad (\text{D.92})$$

where  $\theta$  is the yaw angle and  $\phi$  is the angle of attack of the measurement head of the Pitot-static probe. Both angles can be estimated to be within  $\pm 3^\circ$ . The resulting uncertainty caused by probe misalignment is  $\varepsilon_{\Delta P, \theta} / \Delta P = 1.9 \times 10^{-6}$ .

The above elements can be inserted into Equation D.88. For a sample case for  $U_\infty \approx 70$  m/s at standard atmosphere and temperature, the uncertainty for the dynamic pressure is calculated to be  $\varepsilon_{\Delta P} = 26.1$  Pa, which is dominated by the calibration uncertainty.

Combining the uncertainties and mean values for  $\rho$  and  $\Delta P$  with Equations D.81-D.83, the total standard uncertainty in velocity can be computed for each data point using the final form:

$$\varepsilon_U = \sqrt{\left(\sqrt{\frac{1}{2\Delta P \rho}} \varepsilon_{\Delta P}\right)^2 + \left(\sqrt{\frac{\Delta P}{2\rho^3}} \varepsilon_\rho\right)^2} \quad (\text{D.93})$$

## PUBLICATIONS AND PRESENTATIONS

- Gray, P. D., Lakebrink, M., Straccia, J., Thomas, F., Corke, T., Gluzman, I., “Experimental and Computational Evaluation of Smooth-Body Separated Flow over Boeing Bump”, *AIAA Aviation Forum*, Jun. 2023.
- Gray, P., Gluzman, I., Corke, T., Thomas, F., “Experimental Investigation of Embedded Shear Layer in Smooth-body Separated Flow over Boeing Bump”, *IACAS*, 2023.
- Gluzman, I., Gray, P., Corke, T., Thomas, F., “Accurate skin friction measurement over 3D surfaces via a simplified photogrammetry procedure in oil-film interferometry”, *IACAS*, 2023.
- Gray, P. D., Gluzman, I., Thomas, F. O., Corke, T. C., Mejia, K., “Coherent Vortical Structures in the Separated Flow over a 3D Hump”, *American Physical Society’s Division of Fluid Dynamics (APS DFD)*, Nov. 2022.
- Gray, P. D., Gluzman, I., Thomas, F., Corke, T., Lakebrink, M., and Mejia, K., “Benchmark Characterization of Separated Flow Over Smooth Gaussian Bump,” *AIAA Aviation Forum*, AIAA-2022-3342, Jun. 2022.
- Gluzman, I., Gray, P., Mejia, K., Corke, T. C., and Thomas, F. O., “A simplified photogrammetry procedure in oil-film interferometry for accurate skin-friction measurement over arbitrary geometries,” *Experiments in fluids*, Vol. 63, No. 7, 2022.
- Gray, P. D., Gluzman, I., Thomas, F. O., and Corke, T. C., “Experimental Characterization of Smooth Body Flow Separation Over Wall-Mounted Gaussian Bump,” *AIAA SciTech Forum*, 2022.
- Gray, P. D., Gluzman, I., Thomas, F., Corke, T., Lakebrink, M., and Mejia, K., “A New Validation Experiment for Smooth-Body Separation,” *AIAA Aviation Forum*, AIAA-2021-2810, Aug. 2021.

## ACKNOWLEDGEMENTS

The design of the bump model was developed by Philippe Spalart (Senior Technical Fellow, the Boeing Company, Retired) in close collaboration with J. Slotnick of Boeing and the New Technologies and Services (NTS) group under Professor Strelets in St. Petersburg. Bump fabrication was done in the University of Notre Dame Hessert Fabrication Shop by Terry Jacobson.

This work is funded through a cooperative effort between the Office of Naval Research, the National Aeronautics and Space Administration, the Army Research Office, the Air Force Research Lab, and The Boeing Company. Any opinions, findings, and conclusions or recommendations expressed in this material are those of the authors and do not necessarily reflect the views of the Office of Naval Research. The government funding for the work is provided thru the ONR Cooperative Agreement No. N00014-20-2-1002.

## BIBLIOGRAPHY

1. I. Gluzman, P. Gray, K. Mejia, T. C. Corke, and F. O. Thomas. A simplified photogrammetry procedure in oil-film interferometry for accurate skin friction measurement over a gaussian bump. *Experiments in Fluids*, 2022.
2. Hermann Schlichting. *Boundary-layer theory*. Springer, Berlin, ninth edition.. edition, 2016.
3. Ghanem F. Oweis, Eric S. Winkel, James M. Cutbrith, Steven L. Ceccio, Marc Perlin, and David R. Dowling. The mean velocity profile of a smooth-flat-plate turbulent boundary layer at high reynolds number. *Journal of fluid mechanics*, 665:357–381, 2010.
4. Kapil A Chauhan, Peter A Monkewitz, and Hassan M Nagib. Criteria for assessing experiments in zero pressure gradient boundary layers. *Fluid dynamics research*, 41(2):021404, 2009.
5. I. Marusic, K. A. Chauhan, V. Kulandaivelu, and N. Hutchins. Evolution of zero-pressure-gradient boundary layers from different tripping conditions. *Journal of fluid mechanics*, 783:379–411, 2015.
6. J Delery. *Three-dimensional separated flow topology : critical points, separation lines and vortical structures*. Focus series in fluid mechanics. ISTE ; Wiley, London : Hoboken, N.J., 2013.
7. J Slotnick, A Khodadoust, J Alonso, D Darmofal, W Gropp, E Lurie, and D Marvriplis. Vision 2030 cfd study:a path to revolutionary computational aerosciences. *Technical Report, NASA/CR-2014-218178*, 2014.
8. Daniel J Simmons. An experimental investigation of smooth-body flow separation. Ph.D dissertation, University of Notre Dame, 2020.
9. D.J. Simmons, F.O. Thomas, T.C. Corke, and F. Hussain. Experimental characterization of smooth body flow separation topography and topology on a two-dimensional geometry of finite span. *Journal of fluid mechanics*, 944, 2022.
10. Owen Williams, Madeline Samuell, Sage Sarwas, Matthew Robbins, and Antonino Ferrante. Experimental study of a cfd validation test case for turbulent separated flows. 2019.

11. W.L. Oberkampf and B.L. Smith. Assessment criteria for computational fluid dynamics validation benchmark experiments. AIAA paper 2014-0205, 2014.
12. A Cary, A Dorgan, and M Mani. Towards accurate flow predictions using unstructured meshes. In *AIAA Proceedings*, 2009.
13. Patrick D. Gray, Igal Gluzman, Flint Thomas, Thomas Corke, Matthew Lakebrink, and Kevin Mejia. A new validation experiment for smooth-body separation. *AIAA Aviation Forum*, 08 AIAA-2021-2810, Aug. 2021.
14. Patrick D. Gray, Igal Gluzman, Flint O. Thomas, Thomas C. Corke, Matthew T. Lakebrink, and Kevin Mejia. Benchmark characterization of separated flow over smooth gaussian bump. *AIAA Aviation Forum*, 08 AIAA-2022-3342, Jun. 2022.
15. Patrick D. Gray, Matthew T. Lakebrink, Flint O. Thomas, Thomas C. Corke, Igal Gluzman, and Joseph Straccia. Experimental and computational evaluation of smooth-body separated flow over boeing bump. In *AIAA AVIATION 2023 Forum*.
16. Albert E. Von Doenhoff. The effect of distributed surface roughness on laminar flow. In G.V. LACHMANN, editor, *Boundary Layer and Flow Control*, pages 657–681. Pergamon, 1961.
17. Jewel B Barlow. *Low-speed wind tunnel testing*. Wiley, New York, 3rd ed.. edition, 1999.
18. *Flow visualization II : proceedings of the Second International Symposium on Flow Visualization, September 9-12, 1980, Bochum, West Germany*. Hemisphere Pub. Corp., Washington, 1982.
19. *A Collection of flow visualization techniques used in the aerodynamic research branch*. NASA technical memorandum ; 85998. National Aeronautics and Space Administration, Ames Research Center, Moffett Field, Calif., 1984.
20. *Flow-visualization techniques used at high speed by configuration aerodynamics wind-tunnel-test team*. NASA technical memorandum ; 210848. National Aeronautics and Space Administration, Langley Research Center ; Available from NASA Center for AeroSpace Information (CAS), Hampton, Va. : Hanover, MD, 2001.
21. W Gracey. *Measurement of aircraft speed and altitude*. 1981.
22. F.E. Jones. The air density equation and the transfer of the mass unit. *Journal of Research of the National Bureau of Standards*, 83(5):419, 1978.
23. John L Monteith. *Principles of environmental physics*. Academic, Oxford, 4th ed.. edition, 2012.

24. William Sutherland. Lii. the viscosity of gases and molecular force. *The London, Edinburgh, and Dublin Philosophical Magazine and Journal of Science*, 36(223):507–531, 1893.
25. Charles G Lomas. *Fundamentals of hot wire anemometry*. Cambridge University Press, Cambridge [Cambridgeshire] ; New York, 1986.
26. H H Bruun. Hot-wire anemometry: Principles and signal analysis. *Measurement Science and Technology*, 7(10):024, oct 1996.
27. Marcus Hultmark and Alexander J Smits. Temperature corrections for constant temperature and constant current hot-wire anemometers. *Measurement science technology*, 21(10):105404–105404, 2010.
28. George G Mateer, Daryl J Monson, and Florian R Menter. Skin-friction measurements and calculations on a lifting airfoil. *AIAA journal*, 34(2):231–236, 1996.
29. Alan J Wadcock, Gloria K Yamauchi, and David M Driver. Skin friction measurements on a hovering full-scale tilt rotor. *Journal of the American Helicopter Society*, 44(4):312–319, 1999.
30. Tianshu Liu. Global skin friction measurements and interpretation. *Progress in Aerospace Sciences*, 111:100584, 2019.
31. Th Von Karman. Turbulence and skin friction. *Journal of the Aeronautical Sciences*, 1(1):1–20, 1934.
32. H Dong, SC Liu, X Geng, YD Cui, and BC Khoo. A note on flow characterization of the fx63-137 airfoil at low reynolds number using oil-film interferometry technique. *Physics of Fluids*, 30(10):101701, 2018.
33. Kristofer M Womack, Charles Meneveau, and Michael P Schultz. Comprehensive shear stress analysis of turbulent boundary layer profiles. *Journal of Fluid Mechanics*, 879:360–389, 2019.
34. Jonathan W Naughton, S Viken, and David Greenblatt. Skin friction measurements on the nasa hump model. *AIAA journal*, 44(6):1255–1265, 2006.
35. LH Tanner and LG Blows. A study of the motion of oil films on surfaces in air flow, with application to the measurement of skin friction. *Journal of Physics E: Scientific Instruments*, 9(3):194, 1976.
36. Jonathan W Naughton and Mark Sheplak. Modern developments in shear-stress measurement. *Progress in Aerospace Sciences*, 38(6-7):515–570, 2002.
37. David M Driver. Application of oil-film interferometry skin-friction measurement to large wind tunnels. *Experiments in Fluids*, 34(6):717–725, 2003.

38. Hassan M Nagib, Chris Christophorou, and Peter A Monkewitz. High reynolds number turbulent boundary layers subjected to various pressure-gradient conditions. In *IUTAM symposium on one hundred Years of boundary layer research*, pages 383–394. Springer, 2006.
39. Leonard Charles Squire. The motion of a thin oil sheet under the steady boundary layer on a body. *Journal of Fluid Mechanics*, 11(2):161–179, 1961.
40. Daryl J Monson, George G Mateer, and Florian R Menter. Boundary-layer transition and global skin friction measurement with an oil-fringe imaging technique. *SAE Transactions*, 102:1829–1843, 1993.
41. Saleh Rezaeiravesh, Ricardo Vinuesa, Matthias Liefvendahl, and Philipp Schlatter. Assessment of uncertainties in hot-wire anemometry and oil-film interferometry measurements for wall-bounded turbulent flows. *European Journal of Mechanics-B/Fluids*, 72:57–73, 2018.
42. Tianshu Liu, LN Cattafesta III, RH Radeztsky, and AW Burner. Photogrammetry applied to wind-tunnel testing. *AIAA Journal*, 38(6):964–971, 2000.
43. Tianshu Liu, Alpheus W Burner, Thomas W Jones, and Danny A Barrows. Photogrammetric techniques for aerospace applications. *Progress in Aerospace Sciences*, 54:1–58, 2012.
44. JW Naughton, J Robinson, and V Durgesh. Oil-film interferometry measurement of skin friction-analysis summary and description of matlab program. In *20th International Congress on Instrumentation in Aerospace Simulation Facilities, 2003. ICIASF'03.*, pages 169–178. IEEE, 2003.
45. JW Naughton and MD Hind. Multi-image oil-film interferometry skin friction measurements. *Measurement Science and Technology*, 24(12):124003, 2013.
46. Jonathan W Naughton and Tianshu Liu. Photogrammetry in oil-film interferometry. *AIAA journal*, 45(7):1620–1629, 2007.
47. Markus Raffel, Christian E Willert, Fulvio Scarano, Christian J Kähler, Steve T Wereley, and Jürgen Kompenhans. *Particle Image Velocimetry: A Practical Guide*. Springer International Publishing AG, Cham, 2018.
48. R. J Adrian. *Particle image velocimetry*. Cambridge aerospace series ; 30. Cambridge University Press, Cambridge, UK ; New York, 2011.
49. M Stanislas, K Okamoto, and C Kähler. Main results of the first international piv challenge. *Measurement science technology*, 14(10):R63–R89, 2003.
50. Michel Stanislas, K. Okamoto, C.J. Kaehler, and J. Westerweel. Main results of the second international piv challenge. *Experiments in fluids*, 39 (2):170–191, 2005.

51. M Stanislas, K Okamoto, C.J Kähler, J Westerweel, and F Scarano. Main results of the third international piv challenge. *Experiments in fluids*, 45(1):27–71, 2008.
52. Christian J. Kähler, Tommaso Astarita, Pavlos P. Vlachos, Jun Sakakibara, Rainer Hain, Stefano Discetti, Roderick La Foy, and Christian Cierpka. Main results of the 4th international piv challenge. *Experiments in fluids*, 57(6):1, 2016.
53. Andrea Sciacchitano and Bernhard Wieneke. Piv uncertainty propagation. *Measurement science technology*, 27(8):84006, 2016.
54. J Westerweel. Fundamentals of digital particle image velocimetry. *Measurement science technology*, 8(12):1379–1392, 1997.
55. Dirk Michaelis, Douglas R Neal, and Bernhard Wieneke. Peak-locking reduction for particle image velocimetry. *Measurement science technology*, 27(10):104005, 2016.
56. J WESTERWEEL. Efficient detection of spurious vectors in particle image velocimetry data. *Experiments in fluids*, 16(3-4):236–247, 1994.
57. B. Wieneke. Piv anisotropic denoising using uncertainty quantification. *Experiments in fluids*, 58(8):1–10, 2017.
58. Christian Kähler, Sven Scharnowski, and Christian Cierpka. On the uncertainty of digital piv and ptv near walls. *Experiments in Fluids*, 52(6):1641–1656, 2012.
59. Bernhard Wieneke. Piv uncertainty quantification from correlation statistics. *Measurement science technology*, 26(7):74002–10, 2015.
60. Barton L Smith, Douglas R Neal, Mark A Feero, and Geordie Richards. Assessing the limitations of effective number of samples for finding the uncertainty of the mean of correlated data. *Measurement science technology*, 29(12):125304, 2018.
61. Christian Willert. Stereoscopic digital particle image velocimetry for application in wind tunnel flows. *Measurement science technology*, 8(12):1465–1479, 1997.
62. Ajay K. Prasad and Kirk Jensen. Scheimpflug stereocamera for particle image velocimetry in liquid flows. *Appl. Opt.*, 34(30):7092–7099, Oct 1995.
63. T Scheimpflug. Improved method and apparatus for the systematic alteration or distortion of plane pictures and images by means of lenses and mirrors for photography and for other purposes. *British Patent No. 1196*, 1904.
64. F Scarano and A Sciacchitano. Robust elimination of light reflections in piv. In K Okamoto, editor, *9th International Symposium on Particle Image Velocimetry*, pages 1–7. s.n., 2011. 9th International Symposium on Particle Image Velocimetry ; Conference date: 21-07-2011 Through 23-07-2011.
65. Jerry Westerweel and Fulvio SCARANO. Universal outlier detection for piv data. *Experiments in fluids*, 39(6):1096–1100, 2005.

66. Francis H. Clauser. The turbulent boundary layer. In *Advances in Applied Mechanics*, 4:1–51, 1956.
67. Hassan M. Nagib and Kapil A. Chauhan. Variations of von kármán coefficient in canonical flows. *Physics of fluids (1994)*, 20(10):101518–101518–10, 2008.
68. A. E. Perry and H. Hornung. Some aspects of three-dimensional separation. II - Vortex skeletons. *Zeitschrift fur Flugwissenschaften und Weltraumforschung*, 8:155–160, June 1984.
69. M Tobak and D J Peake. Topology of three-dimensional separated flows. *Annual Review of Fluid Mechanics*, 14(1):61–85, 1982.
70. Visesh Chari and Ashok Veeraraghavan. *Lens Distortion, Radial Distortion*, pages 443–445. Springer US, Boston, MA, 2014.
71. Zhengyou Zhang. A flexible new technique for camera calibration. *IEEE Transactions on pattern analysis and machine intelligence*, 22(11):1330–1334, 2000.
72. Janne Heikkila and Olli Silvén. A four-step camera calibration procedure with implicit image correction. In *Proceedings of IEEE computer society conference on computer vision and pattern recognition*, pages 1106–1112. IEEE, 1997.
73. Nobuyuki Otsu. A threshold selection method from gray-level histograms. *IEEE Transactions on Systems, Man, and Cybernetics*, 9(1):62–66, 1979.
74. F DURST and E. S ZANOUN. Experimental investigation of near-wall effects on hot-wire measurements. *Experiments in fluids*, 33(1):210–218, 2002.
75. N. HUTCHINS, T. B. NICKELS, I. MARUSIC, and M. S. CHONG. Hot-wire spatial resolution issues in wall-bounded turbulence. *Journal of fluid mechanics*, 635:103–136, 2009.
76. James P Hubner and Bruce F Carroll. Uncertainty analysis on thin-oil-film skin friction measurements in compressible flow. In *ICIASF'91 Record., International Congress on Instrumentation in Aerospace Simulation Facilities*, pages 231–239. IEEE, 1991.
77. Gregory C Zilliac. Further developments of the fringe-imaging skin friction technique. Technical report, NASA Technical Memorandum 110425, 1996.
78. Antonio Segalini, Jean-Daniel Rüedi, and Peter A Monkewitz. Systematic errors of skin-friction measurements by oil-film interferometry. *Journal of Fluid Mechanics*, 773:298–326, 2015.
79. Taekjin Lee, Taku Nonomura, Keisuke Asai, and Jonathan W Naughton. Validation and uncertainty analysis of global luminescent oil-film skin-friction field measurement. *Measurement Science and Technology*, 31(3):035204, 2019.

80. Daniel J Simmons. *An Experimental Investigation of Smooth-Body Flow Separation*. PhD thesis, University Of Notre Dame, 2020.

This document was prepared & typeset with pdfL<sup>A</sup>T<sub>E</sub>X, and formatted with  
NDdiss2<sub>ε</sub> classfile (v3.2017.2[2017/05/09])